Experimental Studies of the Hydrodynamics of Liquid Droplet Generation and Transport in Microchannels

by

Zeyad Almutairi

A thesis
presented to the University of Waterloo
in fulfillment of the
thesis requirement for the degree of
Doctor of Philosophy
in
Mechanical Engineering

Waterloo, Ontario, Canada, 2014

Author's Declaration

I hereby declare that I am the sole author of this thesis. This is a true copy of the thesis, including any required final revisions, as accepted by my examiners.

I understand that my thesis may be made electronically available to the public.

Abstract

Droplet microfluidics is a promising field since it overcomes many of the limitations of single phase microfluidic systems. The improved mixing time scale, the increase of number of samples and the isolation of droplets are some of its virtues. The core of droplet microfluidics is a two-phase flow condition that is subjected to scaling of the confining geometry. With the scaling the complexities of the flow phenomena arise. For that reason both the processes of droplet generation and transport are not fully understood for various flow and fluid conditions.

The work in this thesis aims to experimentally examine droplet generation and transport in microchannels for flow and fluid conditions that are experimentally challenging to perform. Examination of droplet generation in a T-junction microchannel design was performed with a quantitative velocity field approach known as micro particle image velocimetry (μPIV). The studies on droplet generation focused on very fast generation regimes, namely transition and dripping that have not been studied for a T-junction design. This achievement was accomplished because of the development of a fast optical detection and triggering system that allowed for acquiring images of different identical droplets at the same position.

μPIV results indicate that the quantitative velocity field patterns of different regimes share some similarities. The filling stage in the transition and dripping regimes had some resemblance in their velocity patterns. The velocity patterns for the start of droplet pinch-off were alike for the squeezing and transition regimes. Furthermore, the presence of a surfactant in the droplet phase above the critical micelle concentration (CMC) did not have an effect on the general velocity patterns as long as the capillary number Ca was matched with the no-surfactant condition.

The studies of hydrodynamic properties of droplet transport were performed in hard materials to avoid cumulative error sources, such as material pressure compliance and swelling effects. The project had several parts: designing a microchannel network that allowed studying the hydrodynamic properties of small droplets, surface treatments of the channel material for stable droplet generation and examining the hydrodynamics of small liquid droplets with sizes that have not been reported

in the literature. The studies examined effects of changing the interfacial tension, viscosity, and flow conditions on the transport of droplets.

The experimental results from the hydrodynamic transport studies indicated that for the droplet sizes that were examined the pressure drop of droplets was affected by the capillary number Ca and length of the droplet L_d. Also, the presence of surfactants altered the hydrodynamic properties of droplets. At a high concentration of surfactants the droplets pressure drop was reduced significantly. Moreover, the type of surfactant affected the magnitude of the pressure drop. Experimental results indicate that if the concentration of surfactants was very low (below CMC) it did not have an effect on the droplet excess pressure. These findings are important to consider in designing droplet microfluidic systems with complex channel networks that involve droplet sorting, splitting, and merging for droplets that contain surfactants.

Acknowledgements

In the name of Allah that most Gracious the most Merciful

It is hard to state in a few words my sincere gratitude to all who helped me to finish my academic journey towards earning the PhD degree. First I would like to thank both of my supervisors Carolyn Ren and David Johnson for giving me the opportunity to work with them. The past three years and after being frustrated with all the things going wrong with my experiments professor Johnson helped me overcome the challenges. Our endless discussions about the flow phenomena I wanted to study and the experimental issues that I usually encounter encouraged me to stay on the path and never give up.

I would like to thank David Sinton, João Saores, Roydon Fraser, and Sean Peterson for participating in my PhD defense exam. Their comments and views about the experimental approaches and the results were very insightful.

Special thanks to professor Zhao Lu at CMC Microsystems and for his support and help with the fabrication of the polycarbonate microchannels.

The Waterloo Microfluidics Laboratory was the place where I learned the most. Thanks to all past and current members of the lab. My lab colleague who deserves special appreciation is Tom Glawdel.

King Saud University earns special recognition for sponsoring me.

I would like to thank my father and mother for their encouragement and support of my decision to pursue an academic career. I would like to give special gratitude to the person who was by my side during hard times. That person is my wife Shuruq. Thanks for all what you did. Both Shuruq and I were blessed with a loveable daughter. Jumana you always put joy to our life and we are grateful for that.

To all my friends at Waterloo thanks for the great times we shared together.

Dedication

To my parents and family.

Table of Contents

List of Tables

List of Figures

Acronyms

AOI	Area of interest.
APD	Avalanche photodiode.
BOD	Back of droplet.
CCD	Charged couple device.
CMC	Critical micelle concentration.
CMOS	Complementary metaloxidesemiconductor.
CW	Continuous wave laser.
DDA	Dodcylamine.
HeNe	Helium Neon laser.
IR	Infrared.
LED	Light emitting diode.
LSM	Laser scanning microscopy.
Nd:YAG	Neodymium-doped Yttrium Aluminum Garnet laser.
P	Applied pressure (Pa).
PC	Polycarbonate
PDMS	Polydimethylsiloxane.
PIV	Particle image velocimetry.
PMMA	Poly(methyl methacrylate).
PMT	Photomultiplier tube.
Q	Measured flow rate ($\frac{m^3}{s}$).
SDS	Sodium Dodecyl Sulfate.
ROI	Region of interest.
VOF	Volume of fluid.
2D	Two dimensional flow.
3D	Three dimensional flow.

Greek Symbols

α	Geometrical factor of the T-junction.
α_L	The void fraction of liquid to gas in a two phase gas liquid flow.
β	Droplet slip factor compared to the average velocity of continuous stream.
ΔP^+	Excess pressure of a droplet (Pa).
ΔP_{drop}	Pressure drop across a droplet (Pa).
$\Delta P_{drop,total}$	Pressure drop across a droplet (Pa).
ΔP_{plugs}	Pressure drop across the continuous phase (Pa).
ρ_i	Density of fluid i ($\frac{kg}{m^3}$).
μ_i	Viscosity of fluid i ($\frac{N.s}{m^2}$).
μPIV	Micro-particle image velocimetry.
γ	Interfacial tension between fluids ($\frac{N}{m}$).
λ	Spacing between droplets (m).
ϕ	The flow rate ratio between the continuous phase and the dispersed phase.
ρ_c	Density of the continuous phase ($\frac{kg}{m^3}$).
ρ_d	Density of the dispersed phase ($\frac{kg}{m^3}$).
θ_a	The contact angle formed between a liquid and a horizontal solid surface.
ω_z	Vorticity in the z-direction ($\frac{1}{s}$).

Alphabetical Symbols

$A_{droplet}$	Total area of a droplet (m^2).
Ca	Capillary number.
D_h	hydraulic diameter of a rectangular channel = $\frac{4 \times Crosssectionalarea}{Perimeter}$ (m).
f_{drop}	Frequency of droplets (Hz).
F_γ	The force from the curved interface during droplet generation (N).
F_p	The force from pressure acting on the droplet (N).

F_τ	The shear force that acts on droplet during the generation process (N).
h	Height of channel (m).
$h_{g,square}$	Thickness of the gutter region surrounding a bubble or a droplet in a rectangular microchannel capillary (m).
h_∞	Thickness of the lubrication region surrounding a bubble or a droplet in a capillary (m).
$h_{\infty,square}$	Thickness of the lubrication region surrounding a bubble or a droplet in a rectangular microchannel (m).
$L_{channel}$	Total length of the test channel (m).
L_d	Length of droplet (m).
L^*_{lag}	Droplet interface retraction length after pinch-off (m).
L_{plugs}	The length that separates two droplet from front of droplet to rear of droplet (m).
$L_{plugs,total}$	The total length of all plugs that separate all droplets in a microchannel (m).
n_d	The number of droplets in the test area.
n_g	The refractive index of the glass slide.
n_i	The refractive index of the fluid.
n_o	The refractive index medium between the lens and glass slide.
P_d	Pressure at dilution stream ($mbar$ or Pa).
P_{drop}	Calculated pressure drop of each droplet ($mbar$ or Pa).
$P_{drop,total}$	Calculated total pressure drop for a train of droplets ($mbar$ or Pa).
P_i	Applied pressure at channel inlet ($mbar$ or Pa) i=1,2,3 & 4.
Q_d	Flow rate of the dispersed stream ($\frac{m^3}{s}$).
Q_c	Flow rate of the continuous stream ($\frac{m^3}{s}$).
Q_{Ref}	Measured flow rate at reference condition without droplets ($\frac{m^3}{s}$).
Q_{with_drops}	Measured flow rate in the presence of droplets ($\frac{m^3}{s}$).
Re	Reynolds number.
R_{hyd}	Hydrodynamic resistance channel ($\frac{mbar.min}{\mu l}$ or $\frac{Pa.s}{m^3}$).
$R_{hyd,drop}$	Hydrodynamic resistance of a droplet ($\frac{Pa.s}{m^3}$).
$R_{hyd,drops}$	Total hydrodynamic resistance of a train of droplets ($\frac{Pa.s}{m^3}$).
$R_{hyd,plugs}$	Total hydrodynamic resistance of plugs between droplets ($\frac{Pa.s}{m^3}$).
$R_{hyd,Ref}$	Reference hydrodynamic resistance without droplets ($\frac{Pa.s}{m^3}$).

T_m	Melting temperature of a thermoplastic.
$\vec{u}$	x-component of velocity ($\frac{m}{s}$).
u_d	Velocity of droplet ($\frac{m}{s}$).
u_m	Average velocity of the main fluid ($\frac{m}{s}$).
u_t	Average total flow rate inside the channel ($\frac{m}{s}$).
$\vec{v}$	y-component of velocity ($\frac{m}{s}$).
V_d	Volume of droplet (m^3).
v_m	Average velocity of the main fluid ($\frac{m}{s}$).
w_c	Width of the continuous phase channel (m).
W_d	Width of the dispersed phase channel (m).
w_d	Width of droplet (m).
z	The location of the plane of focus from the bottom channel wall (m).
z_i	The plane of focus of the lens (m).
z_o	The plane of focus in the absence of the glass slide (m).

Chapter 1

Microfluidics and Droplet Microfluidics

1.1 Preface

Microfluidics is a term that is given to the area that focuses on the control of fluids in micro-scale geometries [2, 8, 9, 10]. The geometries of microfluidic devices have a characteristic length less than 1 mm [2, 10]. With the decrease of the confinement geometry for a fluid changes will occur to some physical forces or processes [10]. An effective approach to sense the degree of change for a physical property or a process is to examine the length dimension of the property. For example an area has l^2 and volume has l^3, and the scaling of the geometry will affect the volume more than the area. Changes in secondary properties that are composed of two or more properties can be estimated by examining the relationship between the primary length units, for example surface to volume ratio $= \frac{Area}{Volume} = \frac{l^2}{l^3} = l^{-1}$.

The biggest advantage for microfluidics is the handling of small volumes of fluid. This allows for increasing the number of tests that could be done with minute volumes compared to volumes used in conventional assays [8, 10, 11]. Manifestation of the geometrical scaling appears in the increase of different forces that are negligible in macro-scale conditions. For example electrostatic forces are important in the micro-

scale and can be used to induce flow between junctions of a microchannel [2, 10, 12]. Viscous and interfacial forces are more pronounced compared to the momentum force. One result for the increase of viscous forces is that most microchannel flow has a very low Reynolds number $Re \leq 1$. This flow condition is known as Stokes flow. Fortunately the continuum hypothesis for the fluid properties is still valid for all liquid flows in micro-scale geometries [2, 10, 12].

The start of the attention to microfluidics research can be traced back to the development of fabrication techniques that allowed for the creation of enclosed micro-scaled structures that support fluid flow [2, 10]. This development of fabrication techniques allowed for integration of multiple physical phenomena for controlling and sensing flow processes in microchannels. Phenomena such as electrokinetics, electromagnetics, acoustic wave, and photonics are some examples of processes that have been used and integrated in microfluidic applications [2, 10, 13, 14, 15].

1.2 Microchannel Material

Generally any material that can be formed in an enclosed micro structure is a candidate to be a channel material for microfluidic applications [2, 16, 17]. The choice of a certain material for channel fabrication depends on the intended application that the microfluidic device [2, 17]. Early microfluidic chips were fabricated from silicon and glass since their fabrication procedures were adopted from the photo-lithography approaches that are used in integrated circuits etching [2, 10]. The time of fabrication and cost are two factors that limited the spread of microfluidics research. Since most of the potential microfluidic applications do not require materials with high rigidity there was an interest in working with less expensive materials. Later on attention was directed towards polymeric materials since many of them offer low cost, ease of fabrication and optical transparency [2, 17, 18].

The material of choice for most microfluidic research has been Polydimethylsiloxane (PDMS) because of less time needed for chip fabrication and low cost [17, 18]. The attention that was given to PDMS started from the development of the soft-lithography technique that is used to fabricate the microchannels in normal lab envi-

ronments [17]. A common method used to bond a PDMS microchannel to a substrate is to perform plasma treatment that alters the hydrophobic nature of PDMS to a temporary hydrophilic condition [19, 20, 21]. PDMS has good optical properties that allow for real time monitoring of processes that can be optically detected [17]. Also, the surface of PDMS can be functionalized with chemical monomers or adsorbed molecules for different applications [21, 22].

PDMS has many shortcomings that may affect its use for certain applications [7, 23]. First, PDMS is hydrophobic by nature and it absorbs proteins and some dyes [24]. Secondly, PDMS swells when exposed to different solvents [23]. Thirdly, PDMS is soft and deforms under pressure [25]. Thus, the choice of PDMS as a microchannel substrate for some applications must be taken with care. Hence, the search for other types of materials for microfluidic applications is an ongoing process.

Thermoplastics are polymeric materials that have been used for microchannel fabrication. These materials are hard at room temperature and start to deform and liquidate at a certain temperature, T_m the melting temperature. In recent years thermoplastics attracted an interest since they can be fabricated with various methods with high precision to form microchannel networks. Fabrication approaches including laser ablation, direct machining, and hot embossing are commonly used to form microfluidic systems [16, 26, 27]. Furthermore, automated production methods can be applied to thermoplastics materials which offer an advantage from a fabrication point of view [16]. Typical thermoplastics that were used in microfluidics applications include: Polycarbonate (PC), polystyrene (PS), and Poly(methyl methacrylate) (PMMA). Some of the properties of thermoplastics that are beneficial for microfluidics applications include rigidity, swell resistance and optical transparency.

PDMS and thermoplastics have been used for single and two phase microfluidics applications [27, 28, 29, 30, 31]. For microfluidic two phase liquid/liquid flow applications, usually; the surface of the channel must be conditioned to have a preferable wetting liquid to assure the isolation of fluid segments [27, 30, 31, 32]. Surface conditioning is achieved with different approaches that include: monomer grafting, direct coating, and surfactant adsorption [27, 28, 30, 31].

1.3 Research Motivation

One subarea area of microfluidics is *droplet microfluidics* [33]. This area focuses on the generation and control of droplets inside another liquid confined by a microchannel. These droplets are considered as small reactors that facilitate processes [34]. There are many advantages for using droplet systems that include a larger reduction in the volume of samples, increased number of samples, reduction of cross contamination and higher control on the transport properties [33].

A potential application for droplet microfluidics is in drug screening research [35, 36, 37]. The very small volume of droplets is one advantage that cannot be matched by conventional drug screening methods. Furthermore, droplet microfluidics chips can be designed to incorporate different processes, such as mixing, merging of droplets with different reagents, heating, and detection. This leads to less interaction with the sample. Brouzes *et al.* [3] reported on the use of droplet microfluidics for cytotoxicity screening tests on mammalian cells. In their work they generated a library of reagents with microchannel droplet generators and then merged them with droplets that contained cells. Incubation was done to the droplets for different times. Afterwards, the droplets containing cells were tested with an assay incorporated in a microfluidic network. Figure 1.1 illustrates the flow processes that were done in the cell screening approach reported by Brouzes *et al.* [3]. This work presents the huge potential that droplet microfluidics offer as a screening tool for biological and biomedical applications.

1.4 Objectives

Droplet generation and transport in microchannels are two basic processes in any droplet microfluidic system. These processes are not fully understood for various operational conditions such as the effect of surfactant on the hydrodynamics of droplet transport [34, 38, 39]. This PhD work aimed to study these two processes for conditions that were not examined in the literature. The main objective of this work is to examine the hydrodynamics of liquid droplet generation and transport in rect-

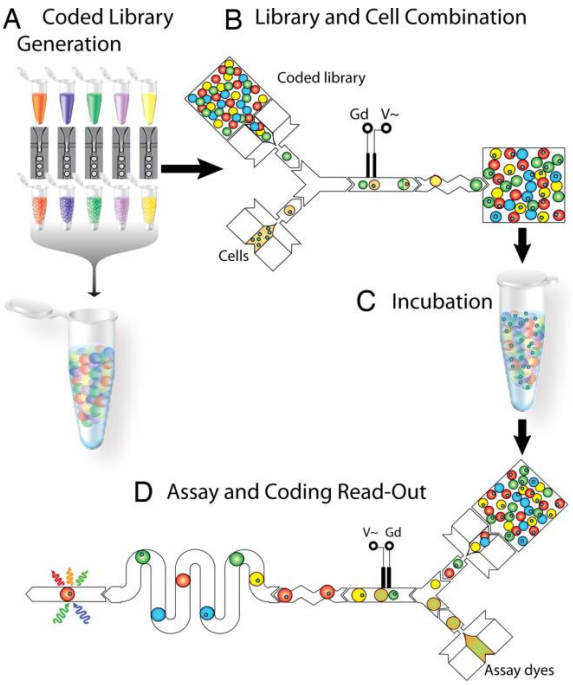

Figure 1.1: The operational principle of the droplet microfluidic system that was used by Brouzes *et al.* [3] for cell cytotoxicity tests. The operation principle (a) Generation of the reagents library with microfluidic droplet generator, (b) Merging of the reagent droplets with the cells droplets, (c) Incubation, and (d) Detection assay. Included with permission.

angular microchannels. The work focuses on studying the hydrodynamics aspects of the two processes with experimental approaches that were adopted from existing experimental techniques and modified for an accurate examination of flow properties. The two themes of the projects studied in this work are: μPIV study of droplet generation in a T-junction design, and the transport of liquid droplets in rectangular microchannels. The specific objectives of the main projects are presented next.

1.4.1 μPIV Study Objectives

TThe process of droplet generation in microchannels has been studied with various approaches to find the proper operational condition for the generation and the final volume of droplets. Most of the studies rely on qualitative experimental techniques that provide the average properties of droplet flow. For quantitative studies of flow patterns inside droplets during the generation process the reported studies in the literature were limited to flow conditions that are considered slow (squeezing regime). This limitation arises from the experimental challenges associated with applying quantitative velocity field studies to fast droplet generation regimes (transition and dripping). The goal of this project is to have a better understanding of the droplet generation process from a velocity field view. Hence, this project can be divided into several objectives:

* Develop a fast droplet detection and μPIV triggering system.
* Study droplet generation in a T-junction microchannel design for fast flow situations (transition and dripping regimes) with a quantitative velocity field approach. The purpose of this part is to compare the velocity patterns that are formed in the droplet phase for each regime and examine the similarities in flow patterns, if it existed.
* Examine the effect of the presence of a high concentration surfactant on the velocity patterns inside the droplet phase during the generation process.
* Study the stages of droplet filling and start of pinch-off in a T-junction microchannel.

1.4.2 Droplet Transport Studies Objectives

The second theme of this thesis focuses on studying the hydrodynamics of liquid droplet transport in microchannels. This work aims to perform the examination of droplets hydrodynamics with a non-intrusive approach and avoid other experimental error sources that might affect the measurements. Practical operational issues including channel swelling and deformation with pressure were avoided in the current studies. The objectives of this project can be listed as follows:

* Design a microchannel network that allows for the examination of the hydrodynamic properties of small droplets with a non-intrusive approach.
* Examine the applicability of using thermoplastics as a channel substrate material for droplet generation and transport studies.
* Optimize a surface treatment approach that conditions the channel surface for the chosen thermoplastic channel material to support stable droplet generation.
* Develop an accurate measurement approach of liquid droplet hydrodynamic properties.
* Study the effect of changing the droplet phase viscosity on the transport of droplets.
* Study the effects of the presence of surfactants on the hydrodynamic properties of droplets. The surfactant studies aimed to understand the effect of the type of surfactant and the surfactant concentration on droplet transport properties.

1.5 Thesis Outline

The thesis will be outlined as follows:

Chapter 2: In this chapter the background of droplet generation and transport in microchannels will be briefly presented. The chapter will focus on the physics

and experimental work for droplet generation studies and the hydrodynamics of droplet transport in microchannels.

Chapter 3: The experimental systems, fluids used and their properties, microchannel designs, and fabrications of the channels will be presented in this chapter.

Chapter 4: In this chapter the experimental work to examine the droplet generation in a T-junction in the squeezing, transition, and dripping regimes with a μPIV system will be discussed.

Chapter 5: This chapter will present the approach used to treat the surface of Polycarbonate (PC) microchannels to alter the surface condition to a hydrophobic state that assures aqueous droplet generation in hexadecane. The aspects for generating droplets in T-junction made from PC will be discussed and compared to droplet generation in Polydimethylsiloxane (PDMS) microchannels.

Chapter 6: In this chapter the approach used to measure the hydrodynamic properties of liquid droplets transported in rectangular PC microchannels will be presented. The results of measuring the hydrodynamic resistance and excess pressure of liquid droplets for various fluids and flow conditions will also be discussed.

Chapter 7: A summary of the work that had been done throughout this thesis with emphasis on the major findings will be revisited. An outlook of future projects will also be discussed.

Chapter 2

Droplet Microfluidics from Generation to Transport

In this chapter a review of droplet generation and transport in microchannels will be presented. For droplet generation review, the focus will be directed towards droplet generation with a T-junction microchannel design and the parameters affecting it, such as wetting of fluid with the microchannel walls and the presence of surfactants. The literature of droplet generation with quantitative μPIV will be presented as well. The second part of the chapter will focus on the transport of droplets in microchannels. The literature for the general transport of segmented flow in capillaries and rectangular channels will be presented to understand the nature of the transport of droplets. Then, attention will be aimed at the literature of the measurement of the hydrodynamic properties of single liquid droplets in microchannels.

2.1 Droplet Microfluidics

When two immiscible fluids come into contact in a confining channel interfacial and body forces between the fluids and the container will influence the fluids shape. If the fluids are dynamically flowing within the confining channel the flow condition

will also affect the flow patterns. The condition of having micro (μm) scaled confinement geometry adds complexity to the flow patterns because of the scaling effect on fluids, and flow forces. This flow condition is known as two phase flow in microchannels [40, 41, 42]. The flow patterns that could be formed in two phase flow in microchannels are complex and depend on the flow condition, as well as the fluids interfacial properties. Some flow patterns that could appear in gas/liquid systems are presented in Figure 2.1. The differences between the flows shown in Figure 2.1 is the dominant force that influences the segmentation pattern (i.e. momentum, viscous, and interfacial).

The forces that act on flows are commonly compared with non-dimensional numbers to scale their importance. Examples of non-dimensional numbers that are used to categorize two phase Newtonian flows are listed in Table 2.1. From the numbers presented in Table 2.1 the most important number in microchannel flows is the capillary number (Ca) since it relates the viscous and interfacial forces.

Droplet microfluidics is a sub-area of two phase flow that focuses on the generation, transport, and control of liquid droplets in microchannels [34, 38, 40, 44]. The formed droplets fully block the microchannel that it is generated and transported in. The carrier phase is referred to as the continuous phase while the droplet phase is known as dispersed or segmented phase. In the condition of having the continuous phase wetting the channel walls more than the dispersed phase the droplets are fully separated from the walls of the confining channel by regions of the carrier continuous phase [38, 45, 46].

The generation of monodisperse droplets in another carrier liquid flow can be achieved with simple microchannel designs. These designs allow the continuous phase to induce a disturbance in the forces that maintain the dispersed phase thread causing the interface to rupture and generate droplets. Fortunately, under certain flow conditions this process repeats in a quasi-steady manner in the microscale leading to the creation on monodisperse droplets [38, 45]. Typical microchannel designs that are commonly used to generate droplets include: flow focuser, parallel flow, and T-junction. Figure 2.2 presents schematics of the main geometries used for droplet generation in microchannels [47].

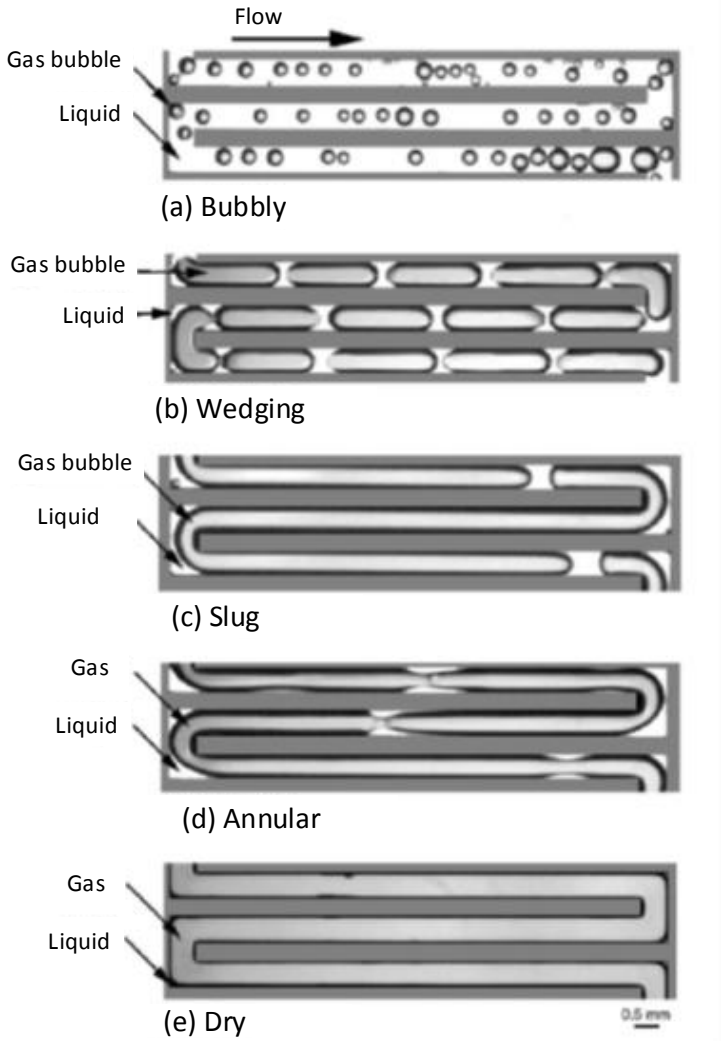

Figure 2.1: The different two phase flow patterns that could be generated in microscale channel geometries for gas/liquid systems. Figure adopted from Cubad and Ho [43] permission.

Table 2.1: The non-dimensional numbers that are commonly used to categorize two phase Newtonian flow.

Non dimensional number	Forces	Formula
Reynolds (Re)	Momentum and viscous	$\frac{\rho u L}{\mu}$
Capillary (Ca)	Viscous and interfacial	$\frac{u\mu}{\gamma}$
Peclet (Pe)	Advection transport and diffusive transport	$\frac{Lu}{D}$
Bond (Bo)	Buoyancy and interfacial	$\frac{\rho g L^2}{\gamma}$
Weber (We)	Inertia and interfacial	$\frac{\rho u^2 L}{\gamma}$

Note: the variables listed in the above table are as follows: ρ is the density of the fluid, u is the average velocity, μ fluid viscosity, γ is the interfacial tension, L is a characteristic length, and D is the diffusion coefficient of molecule or particle.

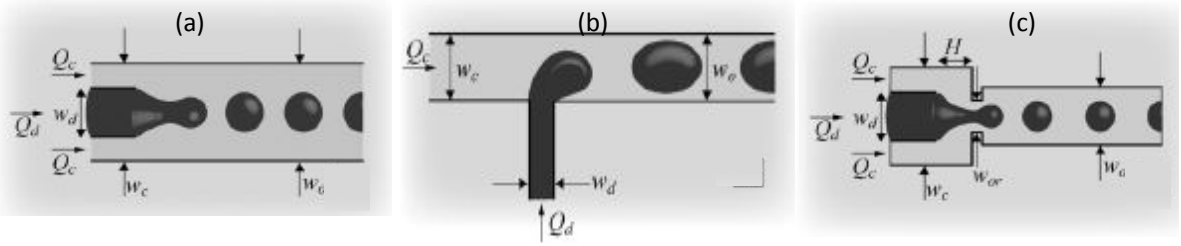

Figure 2.2: A schematic illustration of the main microchannel designs for droplet generators. [47]. The droplet generators are: (a) Co-flow, (b) T-junction, and (c) Flow focusing. The main parameters labelled in the figures are: Q_c the continuous phase flow rate, Q_d is the dispersed phase flow rate, w_o is the width of the main channel, and w_d is the width of the channel supplying the dispersed phase. The figure was taken from Christopher and Anna [47] (Included with permission).

Interest in fluid segmentation in microchannels has risen due to the advantages that it offered over single phase microfluidics. The extremely low volumes of generated fluids (*nano* to *pico* litre), high throughput (in the kHz), and isolation of the droplets from the confining walls are some of the reasons droplets attracted the attention of researchers [33, 34, 38]. Another advantage is that fluid segmentation improved mixing of miscible reagents at low Re flows, also known as Stokes flow [48, 49]. The enhancement in mixing occurs in both the carrier phase and segment phase, as seen in Figure 2.3. The main cause of improvement in mixing is the flow circulation patterns that occur due to the relative motion between the two fluid phases.

T-junction microchannel designs are widely used to generate droplets in microfluidic systems [34, 38, 39]. In most T-junction droplet generators the continuous phase flows in the main channel and the dispersed phase flows from the branch of the T-junction, as shown in Figure 2.4. The fluid segment is generated since the dispersed phase fully, or partially, blocks the main channel that disrupts the physical forces between the liquid thread and the continuous phase. The pressure, interfacial, and shear forces from the continuous phase rupture the dispersed phase interface that leads to the generation of the droplet. Figure 2.4 presents an illustration of the forces that interact during the droplet generation process in a T-junction design.

Droplet generation in a T-junction is affected by the geometrical aspects of the T-junction, the fluid properties, and the flow condition. The geometrical parameters for T-junction designs, similar to one shown in Figure 2.4 -(a), are: w_c main channel width, w_d dispersed phase channel width, and height h. The fluid properties are: μ_c viscosity of the continuous phase, μ_d viscosity of the dispersed phase, and γ the interfacial tension between the two fluids. The flow conditions are: Q_c the flow rate of the continuous phase, Q_d the flow rate of the dispersed phase, P_c the applied pressure at the continuous phase, and P_d the applied pressure at the dispersed phase.

The different forces that interact during droplet generation are: pressure force F_p, shear force F_τ, and interfacial force F_γ. The magnitudes of these forces dynamically change according to the evolution of droplet shape and the flow condition [28, 39]. The interfacial force F_γ originates from the shape that the interface attains during the confinement and the interfacial tension between the fluids. The shape of the

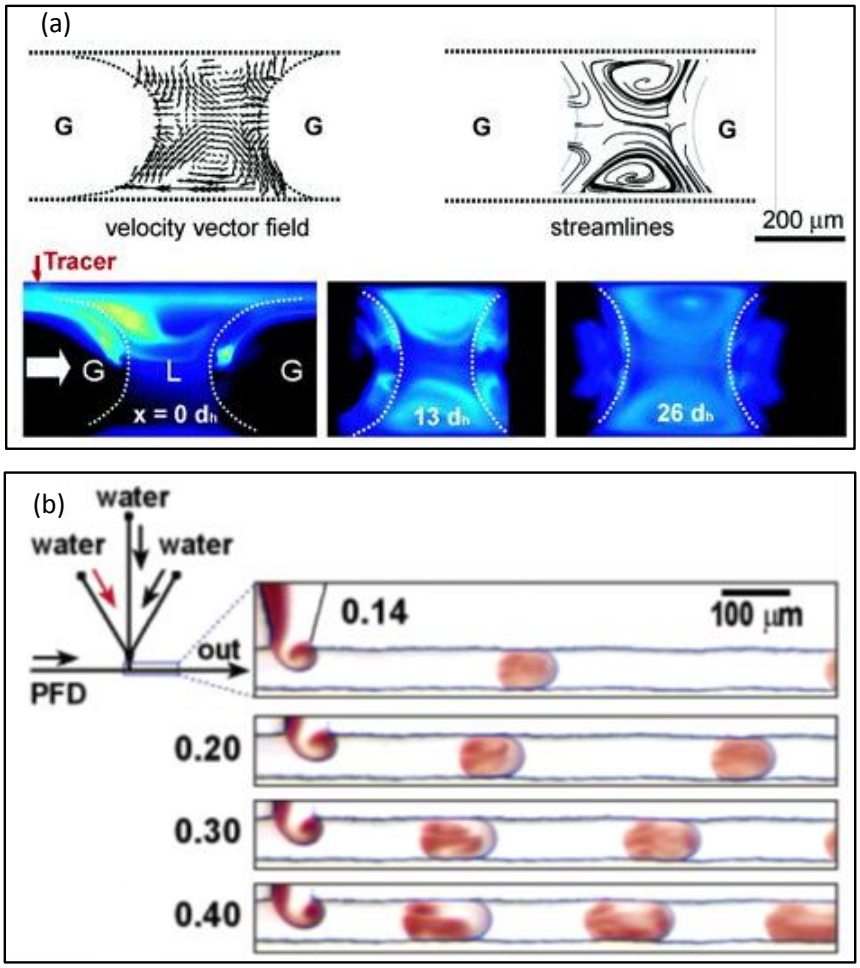

Figure 2.3: Flow mixing patterns in segmented fluid flow in microchannels. Figure (a) Flow mixing patterns that occur in the continuous phase in segmented gas/liquid flow in microchannels reported by Gunther *et al.* [50] (Copyright 2005 American Chemical Society, Langmuir), (b) Flow mixing in liquid/liquid flow in the droplet phase droplet microfluidic systems presented by Tice *et al.* [48] (Copyright 2003 American Chemical Society, Langmuir).

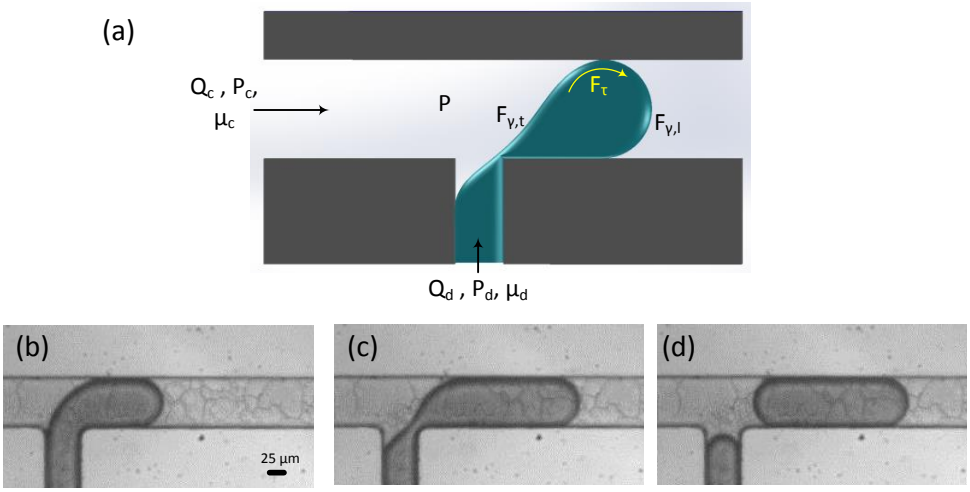

Figure 2.4: A schematic illustration of the forces present during the droplet generation process in a T-junction design along with typical images from the stages of droplet generation. Figure (a) Schematic illustration of the forces that act on the dispersed phase during droplet generation (courtesy of Michael Winer), (b) Image of the filling stage, (c) Droplet squeezing process, and (d) pinched off droplet.

interface is dictated by the surface tension between the two liquids and the confinement condition. These conditions force the liquid interface to attain a curved profile [51, 52, 53]. The pressure drop across the curved interface can be calculated from the Laplace pressure equation. For the leading edge of the droplet presented in Figure 2.4 the pressure drop across the interface can be estimated from [54]:

$$\triangle P_{\gamma,l} = \gamma \left(\frac{2}{h} + \frac{2}{w_c} \right) \tag{2.1}$$

where $\triangle P_{\gamma,l}$ is the Laplace pressure from the leading edge curved interface. The two geometrical parameters $\left(\frac{2}{h}, \frac{2}{w_c}\right)$ arise from the fact that the nature of confinement for a stationary droplet leads to having each radius with half of the dimension of the confinement.

Droplet generation in a T-junction has different stages: filling, squeezing and pinch-off. The filling stage is the stage where the dispersed phase enters the main channel and starts to block the channel. The squeezing stage occurs when the interface of the dispersed phase is being squeezed by the continuous phase and its thread is decreasing. Finally the pinch-off is the stage where the liquid thread of the dispersed phase detaches and forms a droplet.

After droplets are generated they are transported in the confining channel. This is achieved by applying body forces that exceed the added resistance of the droplets. Usually pressure is applied to the channel transporting the droplets. The amount of pressure applied, or the pressure gradient in the channel needed to transport a single or a train of droplets is influenced by various factors associated with encapsulation conditions of the droplets and the fluid properties. The extent of the force needed to transport a droplet can be estimated by knowing the shape of the droplet in a microchannel where a simple look at the nature of confinement of the droplet can give an indication about its resistance. Figure 2.5 presents a schematic illustration of a droplet in a rectangular microchannel for the condition of having a fully wetting continuous phase that encapsulates the droplet.

From the schematics presented in Figure 2.5 it is shown that the expected shape of a droplet is influenced by the confining geometry. Regardless of the dimensions of

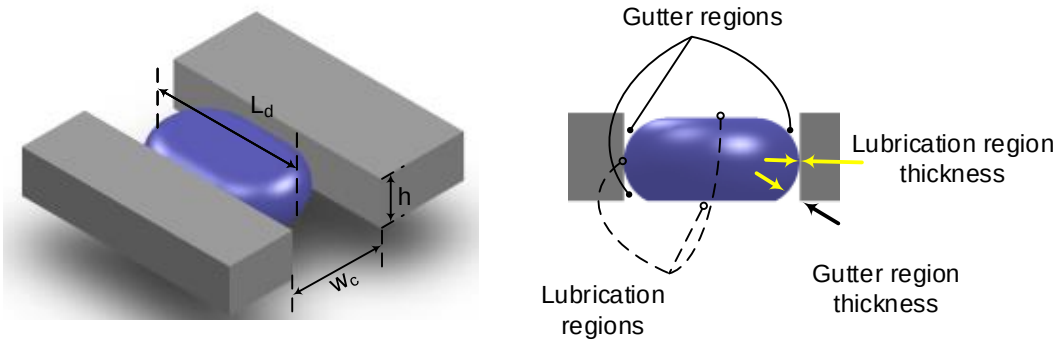

Figure 2.5: A three dimensional schematic illustration of a droplet inside rectangular microchannel with a front section of the droplet showing the lubrication regions (Courtesy of Michael Winer).

the channel there will be regions of the continuous phase that separate the droplet from the channel walls. These regions are gutter regions, and lubrication regions. The gutter regions are located at the corners of the channel and are present since the continuous phase wets the channel and occupies the corners [55, 56, 57]. The lubrication regions are located between the walls of the channel and the droplet. The thickness of the gutter regions is larger than the lubrication regions in rectangular microchannels. These thicknesses are affected by the flow conditions, fluid properties, and wetting condition.

The pressure drop across a droplet in a rectangular microchannel is composed of the pressure drop from the encapsulating regions and the pressure drop across the droplet phase. The pressure drop of the droplet phase has two parts: the pressure drop from the curved leading and trailing interfaces, and the viscous component of a droplet body [38].

The above brief discussions were presented to illustrate the effect of the nature of confinement on the shape of droplet and the expected sources of pressure drop that must be overcome for droplet transport. It should be emphasized that the flow conditions will affect the transport of droplets since it will have an influence on the shape of droplets and confinement conditions. Details of the flow segmentation

patterns and flow properties will be presented in later sections.

2.2 Droplet Generation in Real Microfluidic Systems

In the previous section the process of droplet generation in a T-junction microchannel was presented in a general and ideal condition. However, in actual microfluidic systems the process is complex and is affected by many practical issues and dynamic system factors associated with droplet generation and transport. Properties of the channel network design, fluid pumping mechanism, fluids wetting condition with the channel, and the presence of surfactants all have crucial implications on the droplet generation process. Brief clarifications about the effects of these factors are presented next.

2.2.1 Channel Network Design

Microfluidic droplet generation systems are simply microchannel networks with source and outlet ports. The flow in a microchannel network with multiple ports is affected by the changes of pressure, or hydrodynamic resistance at any junction. In droplet generation systems change in the hydrodynamic resistance of the channel network occur because of the droplet generation and transport in the network [58]. This change is dynamic where the addition of a droplet changes the resistance of the network and will eventually change the droplet generation process. The manifestation of the changes in the dynamic resistance appear in the form of droplet velocity fluctuations as they are transported or the change in the droplet generation size or spacing with time [59, 60, 61]. This process is referred to as the feedback effect [58]. Hence, reaching a stable monodisperse droplets size maybe difficult since the overall channel resistance system is dynamically unstable.

Researchers who encountered these problems in microfluidic droplet systems were able to define design criteria that allowed systems to reach steady generation con-

ditions [59, 60, 61]. Designs with high hydrodynamic resistance downstream of the droplet generator showed better droplet volume stability compared to networks that have low hydrodynamic resistance with respect to the generator section. The reason is that with a large resistance the downstream channel is slightly affected by addition of droplets [62]. Thus, droplet generation will reach steady conditions after a critical number of droplets, or bubbles, had been generated in the network [61]. The other rule that was found to improve the stability of a T-junction droplet generator is increasing the resistance of the channel that supplies the dispersed phase to the T-junction. This resistance should be in the same order as resistance of the downstream channel [59]. These two criteria are sufficient in order to have stable droplet generation systems with minimal feedback in long runs of droplet generation.

2.2.2 Fluid Pumping System

There are two types of fluids supply systems for droplet generation in microchannels: passive, and active [39, 63]. In passive generation fluids are supplied to the T-junction with a continuous source. The two main types of sources are continuous flow sources (i.e. syringe pump), and constant pressure system. The size and frequency of generated droplets in passive systems are affected by the fluids, geometry (w_c, w_d, and h), and flow (Q_d and Q_c) variables [28, 39, 54, 64]. Constant pressure systems were reported to have better stability in generating stable droplet sizes and spacing compared to continuous flow systems [65]. This is due to the fact that by applying constant pressure the flow in the channels adapt to the applied pressure and reach a steady condition. Furthermore, there are no moving parts in the pressure systems.

By contrast syringe pumps have moving parts that propel syringes to pump the fluid. This mechanism is achieved by having an electric motor that rotates a lead screw with a certain pitch. Thus, the speed of the motor, the diameter of the lead screw, the pitch, and the diameter of the syringes may have an effect on the stability of droplet generation. These issues were studied by Korczyk *et al.* [65] where they compared the variation in droplet size between a syringe pump and a pressure system flow system. Their results indicate that the pressure system gave stable

droplet generation patterns compared to the settings that they used with syringe pumps [65]. It should be pointed out that proper choice of the syringe pump, the diameter of the syringe, and flow rate will lead to stable outcomes from the syringes.

Active control approaches, also known as the droplet on demand systems, utilize valves or controllable pressure regulators to control the flow of the continuous or dispersed phase at the T-junction [66, 67]. The size of the droplet is a function of the opening time of the valves. One example for a droplet on demand system was presented by Galas *et al.* [67] where they took advantage of the flexibility of PDMS to create a multilayer flow control assembly. Their assembly had two parts: the channel section, and the control section. These two sections were separated by a thin PDMS membrane. The deflection of the membrane controlled the flow in the channel and was actuated by a pneumatic system. Figure 2.6 presents a schematic of the design and typical outcomes for droplet generation that were presented by Galas *et al.* [67].

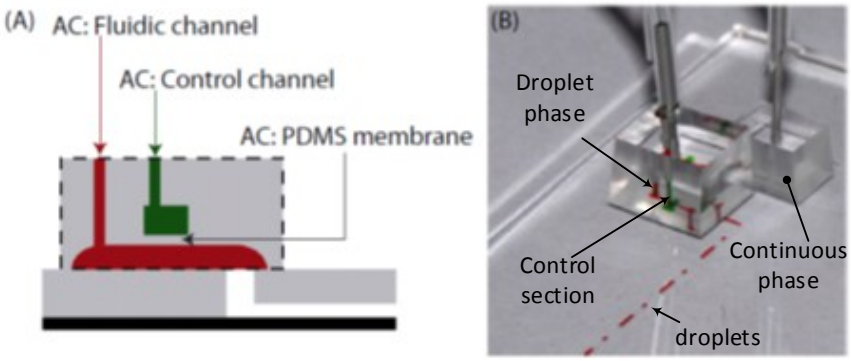

Figure 2.6: A schematic illustration of the pressure control approach used to generate droplets on demand and a typical outcome for droplet generation. Figure (a) Side section of the multilayer active flow control design made from PDMS, and (b) Droplet generation patterns generated in an actual PDMS microchannel. Figures were adapted from Galas *et al.* [67].

2.2.3 Wetting of Surfaces

A crucial property that affects droplet generation is the degree of wetting that the fluids have with the channel material [68]. This property affects the stable formation of droplets and their transport. Simply, if a small volume of a liquid is gently placed onto a horizontal flat surface it can act in two ways: spread on the surface or it could stay stationary and the liquid interface forms an angle with the solid [68, 69, 70]. The first condition is referred to as total wetting where from a macroscopic point of view the angle between the liquid and solid is 0^o. The second condition where an angle is formed is referred to as partial wetting [68, 69]. Partial wetting has two conditions: hydrophilic or hydrophobic. The difference between those two conditions is the angle formed between the solid/liquid interfaces. If the angle is below 90^o then the surface is considered hydrophilic surface and the solid favors the fluid [68, 70]. By contrast, the surface is considered hydrophobic if the angle is above 90^o. Figure 2.7 illustrates the different conditions of fluid drops with partial wetting on a horizontal surface.

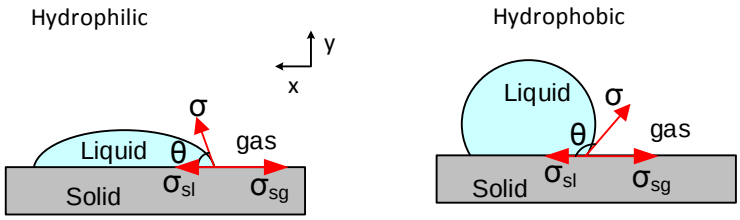

Figure 2.7: A schematic illustration of the contact angle formed for the two different wetting conditions.

In the presence of two immiscible liquids in contact with a horizontal surface the wetting condition becomes complicated where the angle formed between the two liquids and the solid wall is crucial for droplet generation and transport in microchannels. To generate monodisperse droplets that are isolated from the channel walls by the continuous phase the contact angle between the dispersed phase on the surface immersed with continuous phase should be at least 135^o [39, 34, 45]. For that reason to assure proper wetting conditions microchannels are usually treated

with procedures that are suited for certain types of fluids. Examples of some of the surface treatment protocols used to alter the wetting conditions of microchannels will be presented later for the different projects that were done in this work.

Sometimes it is hard to measure the contact angle between the two fluids in a microchannel, especially after surface treatments. This is due to the fact that the outcome of a surface treatment performed on a microchannel format may slightly differ from the outcome of treating larger slabs of the materials. However, the wetting condition could be inferred from the flow segmentation process and the transport of liquid segments in microchannels. Proper wetting conditions lead to having a droplet with curved leading and trailing edges, as was presented earlier. If partial wetting exists it will cause the interface of droplets to pin on the channel walls. Inferring the wetting condition of liquid segments by observing the process of fluid segmentation and transport is a practice that was used by researchers [43, 62].

Wetting Properties of PDMS

When using PDMS microchannels for droplet microfluidic systems the oil of choice, mostly, is silicone oil since it naturally wets hydrophobic PDMS. [47, 64, 71]. However, in the soft-lithography fabrication technique plasma treatment is used to aid bonding the fabricated microchannel to a substrate [17, 21]. One result of plasma treatment is that it alters the surface of PDMS from hydrophobic to a hydrophilic condition that does not support proper droplet generation for silicone oils. But with a prolonged heat treatment the surface of PDMS recovers back to a hydrophobic state [19].

Other oils that are commonly used for droplet generation in PDMS microchannels include fluorinated oil [30], mineral oil [6], and hexadecane [72]. Each oil type needs a specific surface treatment approach that guarantee proper wetting for the oil. For example a water repellent (Aquapel) is grafted on the surfaces of PDMS microchannels to aid with droplet generation in fluorinated oils the continuous phase [30]. Hexadecane requires a Silane called OTS (Octadecyltrichlorosilane) to condition the surface of PDMS.

Wetting Properties of Thermoplastics

Thermoplastics come in a wide range and have been used for fabricating microchannel structures [16, 26]. If the intended use of the microfluidics network is single phase or gas/liquid flow applications the microchannels can be used without any alterations to the surface condition [26, 29, 73]. For liquid/liquid droplet systems the choice of material, fluids and surface treatment are important factors that must be considered for a successful droplet system. Two approaches that were used to alter surface properties of thermoplastics include the use of surfactants [31] and monomer grafting [27].

The thermoplastic that was chosen for one project presented in this thesis was polycarbonate (PC) because it can be used to fabricate microchannels and could be treated for liquid droplet generation. PC is a naturally hydrophilic with a contact angle of 82^o. The surface of natural PC will not support generation of liquid droplets with uniform size when using silicone oil and water or hexadecane and water. Hence, surface treatment must be performed to alter the PC surface to a state that supports proper generation of liquid segments. One research group has made several contributions on performing surface treatments to PC microchannels for droplet generation is the group led by Garstecki [27, 32, 74]. Their group worked on altering the surfaces of PC by active monomer grafting and were able to alter the PC surface to a hydrophilic [74], hydrophobic [27], and to a solvent inert condition [32].

Usually, aqueous based solutions are generated as droplets in carrier oils since the applications targeted with droplet microfluidics use water based solutions as a medium for processes. For that reason interest was directed towards the approach of treating PC to a hydrophobic state [27]. Jankowski *et al.* [27] reported an approach to treat the surface of PC to a hydrophobic state that support the generation of water based droplets in different oils. In their work they grafted Dodecylamine (DDA, $C_{12}H_{27}N$) on the surface of PC with the aid of heat and a continuous flow of DDA solution. In their work they examined the effect of changing treatment temperature, concentration of DDA in the solvent, and the type of solvent used. Their work was done on simple T-junctions with a width of 800 μm. Jankowski *et al.* [27] also optimized DDA surface treatment of PC for the duration of the treatment. Their

final recommendations for grafting DDA to PC surfaces in microchannel format were:

* **Type of solvent:** The recommended solvent to dissolve DDA was Ethanol.
* **DDA concentration:** The concentration that gave the best wetting properties was 5%.
* **Temperature of treatment:** The recommended temperature of treatment was 60^o.
* **Duration of treatment:** 1 - 2 hrs.
* **Flow rate of DDA solution:** 2 ml/hr.

The approach reported by Jankowski *et al.* [27] was used, with modifications, to treat microchannels made from PC for the droplet hydrodynamics studies project. Details about modified approach for DDA treatment will be presented later in Chapter 5.

2.2.4 Surfactants

Surface active agents (surfactants) are molecules that have two chemical termination parts that prefer a certain type of fluid. These two parts are a hydrophilic and a hydrophobic part [10, 70, 75]. Between immiscible fluids surfactant molecules orient themselves at the fluid/fluid interface according to the chemical group and fluid phase where the hydrophilic group prefers water and the hydrophobic group prefers oil [10, 70, 75]. This orientation on the interface distorts the surface leading to a decrease in the surface tension between the fluids [10, 70, 75]. The surfactant coverage on the interface creates an immobile surface that helps stabilize emulsions [68, 70, 76]. Moreover, it may cause rheological effects and increase flow resistance at the surface of the liquid/liquid interface [62, 76, 77].

There are two important parameters of surfactants at a liquid/liquid interface in microfluidic applications. These are: the surface coverage of the surfactant on

the interface and critical micelle concentration (CMC). The surface coverage of the surfactant on an interface affects the reduction of the interfacial tension. This coverage is a function of the diffusion time scale of the surfactant molecule and the bulk and surface concentrations of the surfactant. The change of interfacial tension with the surfactant concentration occurs with a specific trend. Typically, at low concentrations of a surfactant there will a small change in the surface tension. At a critical concentration there will be a large change in interfacial tension with the increase of concentration. In the third region, the increase of surfactant concentration will have small effects on the interfacial tension. A typical plot of the change of interfacial tension with the increase of surfactant concentration is presented in Figure 2.8 -(a) [10].

The CMC is the concentration where the surfactant molecules start to rearrange themselves inside the bulk fluid and form micelles (see Figure 2.8). This formation of micelles is due to the nature of termination chemical compounds of the surfactant and the large concentration of molecules. If micelles are formed this indicates that the surfactant concentration in the bulk fluid is high that assures the total surface coverage, if the molecules are given enough time to diffuse to the interface [70].

Surfactants come in various types and chemical structures. They can be characterized according to their Hydrophilic-lypophilic balance (HLB) that is used to differentiate surfactants by their emulsification patterns [70]. Surfactants with low HLB (3-6) are used for water in oil (w/o) emulsions. While surfactants with HLB range from 8-18 are commonly used for oil/water emulsions. For droplet microfluidic systems the HLB number can be used to identify the phase that a certain surfactant can be added to.

The transfer between surfactants bulk concentration inside the fluid to the liquid/liquid interface is a complex process that is affected by type of surfactant, concentration, rate of micelle decomposition, and diffusion time scale. An estimation of a surfactant coverage on an interface based on Gibbs energy equation is formulated as [70]:

$$\Gamma = -\frac{1}{2.303 \cdot nRT}\left(\frac{\partial \gamma}{\partial log C_1}\right)_T \tag{2.2}$$

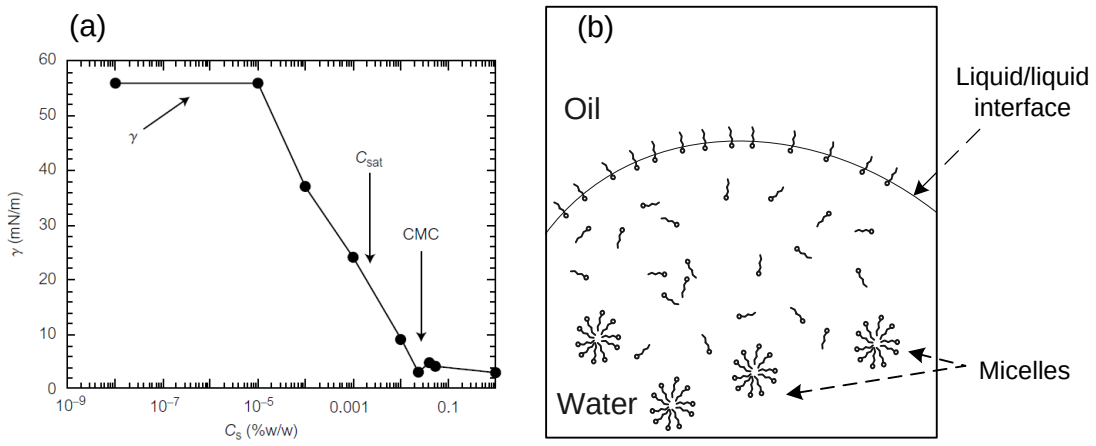

Figure 2.8: A schematic illustration of the surfactant at liquid/liquid interfaces and the relationship between the surfactant concentration and the interfacial tension. Figure (a) The effect of surfactant concentration on the interfacial tension, from Tabeling [10], and (b) an illustration of micelles formation and the orientation of surfactant molecules at the liquid/liquid interface.

where Γ is the surface concentration of the surfactant, n is the number of solute species that change due to the presence of the surfactant, C_1 is the bulk concentration of the surfactant, R is the gas constant, T is the temperature, and γ is the surface tension. The other parameter that is important is the time needed for a surfactant molecule to diffuse to the interface. The time needed for the surfactant to diffuse to the interface is a complex phenomenon in which the kinetics of adsorption, desorption at the interface, and dissociation from the micelles influences it [70]. For a simple case the time needed for a mobile surfactant molecule can be calculated from:

$$t = \frac{L^2}{D} \tag{2.3}$$

where t is the time needed for the molecule to reach the interface. L is the distance that the surfactant needs to travel, and D is the diffusion coefficient of the surfactant molecules. One implication of Equation 2.3 is that larger surfactants with lower diffusion coefficients take longer times to reach the interface.

The reduction of interfacial tension affects the droplet generation process since it reduces the forces needed to rupture the dispersed phase thread. This reduction leads to generating droplets with smaller sizes and at higher frequencies. Xu *et al.* [78] examined the changes in the formation of water droplets in n-Octane solution by altering a surfactant concentration in the dispersed phase. In their work, they used a T-junction droplet generator. Sodium dodecyl sulfate (SDS) was used as the surfactant. The measurement of droplet size was done with video analysis to the final droplet volume. The results from the video analysis confirmed that the size of formed droplets was influenced by the surfactant concentration [78].

In another study of the effect of surfactants on droplet generation Wang *et al.* [79] investigated the effect of changing the surfactant type on the final droplet volume. They used different surfactants and also varied their concentrations. Similar findings to the work of Xu *et al.* [78] the effects of surfactant concentration on the droplet size were observed. Also, Wang *et al.* [79] results show that the droplet size is sensitive to the type of surfactant [79].

2.3 Studies of Droplet Generation Process

The knowledge of droplet generation in micro-scale geometries is crucial for the proper design of microfluidic systems where the volume and the transport properties of the droplets must be known. Droplet generation in T-junction microchannels is an interesting process that has been under extensive investigations to understand the stages of the generation and know final droplet volume [34, 38, 39]. Droplet generation processes have been studied numerically and experimentally [45, 47]. A brief introduction about these techniques will be presented next.

2.3.1 Numerical Methods

Numerical methods are approaches that are used to solve complex flow equations that are difficult; or impossible, to solve analytically. For two phase flow, numerical approaches face a challenge of defining the interface between the two fluids. This is

crucial since the forces that act on the interface, normal and shear forces, affect both phases. The thickness between two immiscible phases is one molecule length which is challenging to simulate in a dynamic flow condition [70, 80, 81].

There are a couple of approaches used to describe the interface of the two phase flow such as: volume of fluid (VOF), Lattice Boltzmann method, and phase field methods [80, 81, 82, 83]. Although there are some concerns with numerical simulations for simulating droplet generation processes they still can be used to estimate the different conditions and the order of magnitude of different forces during the generation process. For example Menech *et al.* [83] used a phase field method that uses a diffusive interface to describe the boundary interface between two immiscible fluids to examine the droplet generation regimes in a T-junction design. Their work resulted in identifying two droplet generation regimes: squeezing and dripping. The main distinction between the two regimes is that pinch-off of a droplet occurs by either a squeezing force on the interface or by shear force from the continuous phase. The Capillary number (Ca) was used to identify the two regimes where below $Ca = 0.015$ the regime is called the squeezing regime.

The volume of fluid (VOF) method is the most widely used method to simulate droplet processes [80]. It uses a diffusive interface representation to describe an interface between the two immiscible fluids. One advantage of VOF is that it can track changes in the shape of the interface during different processes between the fluids, such as droplet generation [80]. The other major advantage of VOF is that it is not numerically demanding.

2.3.2 Experimental Approaches

Experimental methods are the most widely used approaches to study droplet microfluidic systems. This due to the fact that they rely on developed techniques to measure changes in the flow properties such as: electrical conductivity, dielectric constant, refractive index, and fluorescence signals [5, 41, 64, 84, 85, 86]. Experimental techniques have been used to measure various droplet properties such as: droplet speed, length, generation frequency, and volume. For example, capacitive sensors

embedded on the microchannel substrate can be used to find droplet size and speed by measuring the change of electrical properties between the carrier continuous phase and the droplet phase [85]. Another type of sensor is the microwave sensor which differentiate the continuous and the dispersed phase by their conductivity or dielectric constant [86]. These methods offer a general view of some of the droplet properties but do not provide exact changes of the fluid/fluid interface shape during generation. Exact transport properties can be found with optical based approaches that offer real time recording of the shape of droplet, size, and speed. There are many versions of optical based methods but their principle is the same which is to acquire images of a droplet with a digital image recorder at a known frame rate.

A typical optical system for examining droplet generation or transport includes a high speed camera, mostly CMOS based sensors, a light source, and a microscope that contains focusing optics. The images recorded by the camera through the microscope optics are a two dimensional projection of the droplet across its height. Figure 2.9 illustrates one format of an optical system and a recorded image for droplet generation. Other versions of optical detection approaches could be used such as: fluorescence microscopy, and confocal microscopy [87, 88].

Optical based approaches are good tools for examining droplet microfluidic processes which allow understanding of the different stages of droplet generation and how changing the fluid confinement conditions or flow properties can affect a process. Many researchers have studied droplet generation processes in various microchannel geometries such as flow focusing devices, T-junction, and orifice type generators with optical based approaches [34, 38, 39]. Results from experimental work on droplet generation were used to identify the various stages of the generation process, find the flow regimes for stable droplet generation, and to aid with developing correlations that estimate the final droplet volume at different geometrical and flow conditions [28, 47, 54, 59].

Experimental results of droplet generation studies have identified the different stages of droplet generation which are the filling stage, squeezing stage and pinch-off. Also, contradictory to what was found in the numerical simulations by Menech *et*

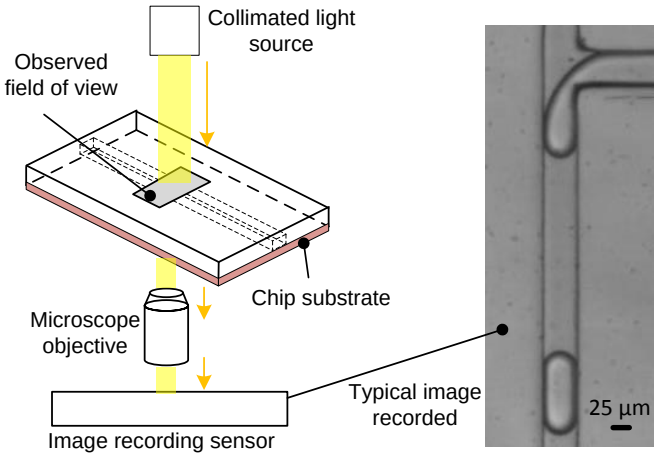

Figure 2.9: An illustration of a typical imaging approach used for studying the droplet generation process. The schematic illustration is for a bright field microscopy approach. The image on the right side of the Figure is for an actual recorded experiment for generating water droplets encapsulated by Hexadecane in polycarbonate microchannels.

al. [83] three droplet generation regimes in a T-junction were identified: squeezing [1], transition, and dripping regimes [89, 90]. These three regimes differ in the main force that causes droplet pinch-off. The new regime identified from experimental results was the transition regime where both shear force and squeezing force affect the droplet generation. Table 2.2 presents the different droplet generation regimes in a T-junction as was found from experimental work [89, 90].

Table 2.2: The droplet generation regimes for T-junction droplet generator characterized by the Capillary number [89, 90] and the corresponding dominant force in the droplet generation process.

Regime	**Ca**	**Force**
Squeezing regime	$Ca < 0.002$	Pressure
Transition regime	$0.002 < Ca < 0.01$	Pressure and shear
Dripping regime	$0.01 < Ca < 0.3$	Shear

Experimental optical imaging based studies recorded the evolution of the dispersed phase shape to estimate the ratio of forces that act on it during the generation process. Some microscopy studies of droplet generation attempt to find correlations of the droplet size generated with respect to experimental conditions. For example Garstecki *et al.* [28] found that at low Ca the droplet generation is dominated by the squeezing pressure that occurs at the back of the droplet (F_p). In this regime the droplet size can be estimated by the ratio of flow rates of the continuous and dispersed phase according to:

$$\frac{L_d}{w_c} = 1 + \alpha \frac{Q_d}{Q_c} \tag{2.4}$$

where L_d is the length of the droplet, and α is a geometrical constant. An improvement to the Garstecki *et al.* [28] model was proposed by Van Steijn *et al.* [54] where they considered the geometrical and fluids aspects to model the droplet volume. They reported that their model gave good approximations for the droplet size below

[1] It is important to distinguish between the squeezing regime and squeezing stage that was mentioned before. The squeezing stage is the stage where the interface of the dispersed phase is squeezed by the continuous phase prior to the rupture of the interface. The squeezing regime is the regime where the droplet generation process is dominated by the pressure build up from the continuous phase.

the dripping regime ($Ca < 0.01$). Other microscopy studies of droplet generation examined droplet modeling in the transition regime [64], effects of unsteadiness in the channel network on droplet generation [58, 91], and the effect of adding surfactants [78, 79].

It should be pointed out that most experimental studies with optical systems are considered qualitative flow studies since their results are for bulk properties, such as area of droplet or average speed. Quantitative flow velocity studies are harder to perform in two phase flow in microchannels since they need special equipment and experimental approaches [1, 84, 92, 93, 94]. The experimental approach/system that is widely adopted for quantitative flow studies is the micro particle image velocimetry (μPIV). A brief description about the μPIV system will be presented next.

μPIV Approach:

μPIV is a term given to the approach of applying the well-established experimental technique of particle image velocimetry (PIV) to flows in micro-scale geometries [1, 2]. PIV is a technique for finding 2D Lagrangian velocity field of a flow by recording the motion of flow tracking particles at known time intervals and finding the velocity by means of statistical cross-correlation [1]. The velocity within a small interrogation area of the flow field can be estimated from [1]:

$$u_{(i,j)} = \frac{\Delta x_{(i,j)}}{\Delta t} \tag{2.5}$$

where $u_{(i,j)}$ is the velocity component in the x-direction at location, $\Delta x_{(i,j)}$ is the change of position of the tracing particle in the x-direction, Δt is the time interval between recorded the images, and *(i,j)* is the location of the interrogation area in the flow field. The two dimensional velocity vectors at the interrogation areas are found from:

$$\vec{V}_{(i,j)} = \vec{u}_{(i,j)} + \vec{v}_{(i,j)} \tag{2.6}$$

where $\vec{V}$ is the velocity vector at the location (x_i, y_j), and $\vec{u}_{(i,j)}, \vec{v}_{(i,j)}$ are the x-component and y-component of the velocity fields respectively. PIV is a well-established experimental technique that has been used to study the flow fields of

enclosed and open flow systems [1, 95, 96, 97]. The technique is well developed with many versions that were used to estimate complex flow properties such as fluid acceleration [98], pressure distribution [99, 100], combustion flows [101], and shear force [102]. The main assumptions associated with PIV are:

- The seeding particles exactly follow the flow [103, 104, 105] .
- The light sheet from the laser is very thin and represents a slice within the flow.
- Particles scatter enough light that can be recorded by the sensor.
- The size of particles are small compared to the interrogation area.
- The time difference Δt is small to avoid acceleration errors.

To satisfy the criteria listed above different light sources (i.e. pulsed and continuous lasers, and light emitting diodes) have been used with numerous image detection formats (i.e. CCD, and CMOS type cameras) along with light conditioning and image focusing optics. One challenge in applying PIV to microchannels is that even the thinnest achievable light slice can illuminate the whole microchannel volume. Furthermore, regular particles that are used in PIV will not scatter enough light at the microscale to distinguish their movement [1, 2, 93]. These two challenges are addressed by using fluorescence microscopy [1, 2, 93]. By guiding the light through a microscope objective thin light sheets can be imaged by the camera. Fluorescent particles address the problem of emitting sufficient light signal to be detected by the image sensor. A typical illustration of the optical path of the light and the field of view that is observed by the camera in a μPIV setup is presented in Figure 2.10.

Although it is expected that only particles that are located in the focal depth of the microscope objective are recorded by the camera in μPIV the out of focus fluorescent particles maybe recorded and contribute to calculated velocity fields. This condition is referred to as the depth of correlation. An estimation of the depth of

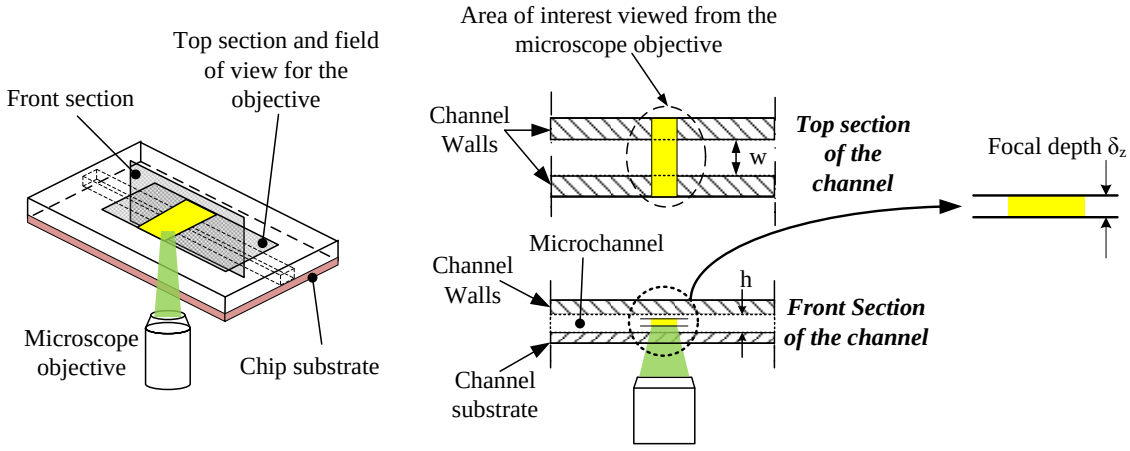

Figure 2.10: A schematic illustration of the field of view from the microscope objective identifying the important optical parameters of the objective for μPIV. The dimensions labeled in the image are the channel width w, the channel height h, and field of focus δ_z.

correction is given by [106]:

$$\delta_{corr} = 2\left[\frac{(1-\sqrt{\varepsilon})}{\sqrt{\varepsilon}}\left(\frac{n_o^2 d_p^2}{4(NA)^2} + \frac{5.95\,(M+1)^2\,\lambda_o^2 n_o^2}{16M^2(NA)^4}\right)\right]^{\frac{1}{2}} \tag{2.7}$$

where δ_{corr} is the depth of correlation, M is the magnification of the objective, d_p is the particle diameter, n_o is the immersion medium index of refraction, λ_o is the light wavelength, and ε is a threshold for the contribution of the defocused particle on the image. It is important to note that these effects are associated with volume illumination and fluorescence imaging. The above discussions were presented to give a brief introduction to μPIV in microchannels and the main aspects of applying the technique to microscale flow. Further readings are recommended such as the reviews by Lindken *et al.* [93] and Wereley and Meinhart [107]. Other readings that include Raffel *et al.* [1] and Nguyen and Wereley [2] are recommended to understand the principle of PIV and μPIV.

Application of μPIV into two phase flow droplet studies faces other challenges including: the refractive index mismatch between the fluids, and the averaging of the results. The issues associated with the refractive index mismatch are: focusing on different planes for the different fluids [108], and optical image distortions that might occur at a fluid/fluid interface [109]. To illustrate the effect of refractive index mismatch a simple example is considered. For a simple configuration light passes through an immersion medium of refractive index n_o and a glass slide of thickness t_g with refractive index n_g into a sample. If the sample had a refractive index n_i the location of the plane of focus can be approximated by Snell's law [108]:

$$z_i \approx \frac{n_i}{n_o} z_o + \left(\frac{n_i}{n_o} - \frac{n_i}{n_g} \right) t_g \tag{2.8}$$

where z_i is plane of focus of the lens, n_i is the refractive index of the fluid, n_o is the refractive index medium between the lens and glass slide, z_o is the plane of focus in the absence of the glass slide, n_g is the refractive index of the glass slide, and t_g is the thickness of the glass slide. When two fluids with different refractive indices are present in the field of view things become more complicated. An illustration of the field of view showing the variables of Equation 2.8 in the presence of two fluids is shown in Figure 2.11.

The issue of focusing on different planes in μPIV studies was examined by Kim *et al.* [108] where they reported that in the presence of two fluids with two refractive indices may have an effect on the observed plane of focus from the objective. They reported that under certain conditions the effect of refractive index mismatch can be neglected. This condition is when the depth of correlation calculated from the lens (Equation 2.7) is larger than the difference in the refractive index mismatch. The formulation of their condition was given as:

$$|z_i - z_j| < \delta_{corr} \tag{2.9}$$

Thus, the choice of microscope objective with high depth of correlation can reduce the effects of refractive index mismatch in regular microscopy. However, this approach may sacrifice the thickness of the plane of measurement and the three dimensional

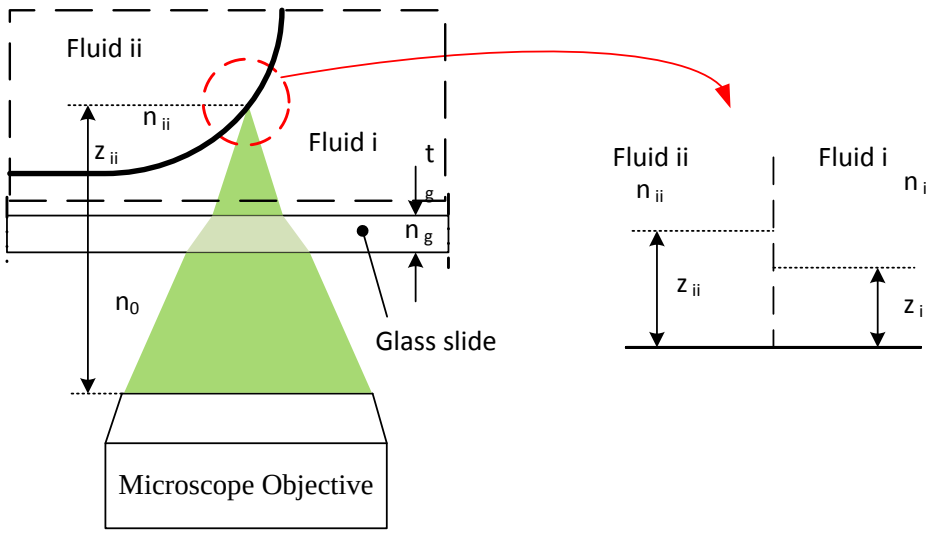

Figure 2.11: An illustration of the field of view by a microscope lens with emphasis on the effect of refractive index mismatch on the plane of focus. Adapted from Kim et al. [110].

flow pattern in the measurement plane may affect the calculated velocities.

The other issue with refractive index mismatch is the problem of image distortions at the fluid/fluid interface. An expression of the effects of image distortions at the fluids interface was reported by Yamaguchi *et al.* [109] where they reported that if the refractive index is not matched for the fluids it may create regions with images with large light distortions at the fluids interface. For that reason the matching of the refractive index of the fluids in two phase flow studies is crucial [93, 94]. This could be done by adding fluids that change the refractive index of water based solutions such as: glycerol, zinc iodide, and sodium iodide [108].

The second major challenge that faces PIV studies of droplet microfluidics is averaging of the results [29, 93, 94]. This issue appears since it is practically impossible to acquire many images of a single droplet and average the results. Averaging results is important for μPIV, and PIV in general, because it reduces the effects of random errors associated with velocity measurements [1]. This issue is addressed by taking one advantage of droplet microfluidics that it is monodisperse and averaging multi-

ple droplets generated at the same steady condition and at the same phase. This approach is referred to as phase-locking of droplets [29, 111].

The first application of high speed μPIV to study a two immiscible liquid/liquid flow was presented by Shinohara *et al.* [92]. Their work focused on examining the dynamic behavior of two immiscible fluids in a cross stream flow condition that can be used in sample extraction in microchannels [92]. In their work Shinohara *et al.* [92] used a continuous wave laser as a light source to illuminate the flow field. The images were recorded with a high speed CMOS camera with an exposure time of 500 μs. To enhance the quality of acquired images an optic fiber image intensifier was used [92]. The microchip was fabricated in Pyrex glass with wet etching techniques. Water and Butyl Acetate were used as the two immiscible fluids in the microchannels. Fluorescent particles were only added in the water phase with $d_p = 1\ \mu m$. Experimental results of the two phase cross stream flow condition showed creation of vortices at the liquid/liquid interface [92]. This behavior was attributed to the interfacial instabilities between the two fluids.

After confirming that the μPIV technique can be used to determine the dynamic flow conditions of two-phase flow, it has been applied to several droplet studies [50, 112, 113]. Fu *et al.* [114] examined bubble formation in flow focusing devices with a μPIV system. The microchannels were fabricated from PMMA. The study was performed by generating N_2 gas bubbles in different combinations of water-glycerol with a surfactant (SDS sodium dodecylsulfate) to examine the effects of altering the viscosity of the water phase. Latex particles with a diameter of $d_p = 0.88\ \mu m$ were added to the water based solution. Illumination of the flow field was done with a stroboscope and the images were captured with high speed CMOS camera. Results from the μPIV study gave valuable information about the effect of the carrier fluid velocity gradient on the bubble break up in flow focusing devices [114]. Moreover, correction factors for empirical models of bubble generation were extrapolated from the fluid velocity measurements.

Malsch *et al.* [115] published quantitative results of the velocity fields inside droplets as the droplet changes its motion due to geometrical channel changes. In their work they examined the flow of water droplets transported in a continuous

phase of Tetradecane. The experimental work was done along with CFD modeling of the flow inside the droplets to confirm the transport properties inside the droplets. Droplets were generated in a glass microchannel network that has a Y-channel intersection which induces droplet generation [115].

The quantitative experimental examination of the flow field inside the droplets was with a high speed μPIV approach [115]. A high-power LED was used to illuminate the flow field. The images were captured with a CMOS camera (Olympus i-SPEED 2). The flow tracking particles, yeast cells ($d_p = 4-5\mu m.$), were introduced in the water phase. In their work, Malsch *et al.* [115] reported the changes in the circulation zones inside a droplet was due to changes of the confinement condition in microchannels. They also observed variation of the mid-plane velocity profile inside the droplet. One concern about the work of Malsch *et al.* [115] is that the velocity measurement is averaged over the entire droplet height. This averaging was due to the depth of focus of the measurement where the focal depth was reported to be 100 μm which is relatively high compared to the microchannel height of $200\mu m$. Thus, caution must be taken since the three dimensional velocity patterns across the droplets may have an influence on the measured velocity fields.

A research group at Delft University has made major contributions to the quantitative examination and understanding of droplet generation in the T-junction microchannels [29, 116]. In their first paper Van Steijn *et al.* [29] examined bubble generation in a T-junction generator with a μPIV system. Their aim was to find the appropriate correlation factors of the T-generator model presented by Garstecki *et al.* [28] (Equation 2.4). The experimental setup of Van Steijn *et al.* [29] consists of an Nd:YAG laser as the light source and a dual frame CCD camera (LaVision, Image Intense) to capture images. The working fluids were ethanol as the continuous phase and air as the dispersed phase. Fluorescent particles $2\mu m$ (Duke Scientific) were introduced in the continuous phase with a particle concentration of 5.7×10^7 particles per ml. The flow was observed by an air objective (5X magnification) which gives a depth of focus of 100 μm. This depth of correlation was $\frac{1}{8}^{th}$ of the channel height. To assure capturing images at the same bubble generation stage an optical based detection approach was used to trigger the μPIV.

Van Steijn *et al.* [29] examined the flow patterns in the continuous phase during the bubble generation for different planes of the channel at different bubble stages. Their results indicated that the gutter region flow after the dispersed phase fully blocks the channel was estimated to be ≈ 24 % of the total flow rate supplied by the fluid source.

The role of the continuous phase flow in triggering and accelerating the dispersed phase pinch-off was reported by Van Steijn *et al.* [116] for gas bubbles formed in the continuous phase of ethanol. The study was performed with a T-junction channel design. In their work, the superiority of the μPIV technique compared to regular microscopy approaches was proven due to the in-depth examination of the flow patterns surrounding the bubbles. Their results include the changes in the velocity profile of the continuous phase prior to pinch-off, as shown in Figure 2.12.

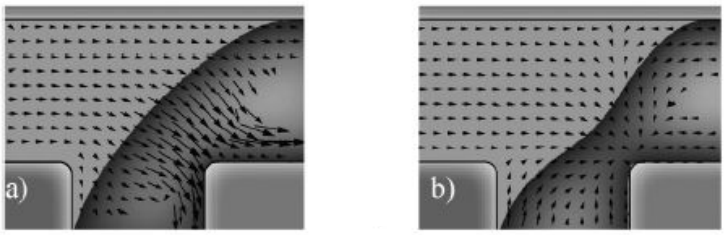

Figure 2.12: μPIV results the three dimensional flow patterns surrounding a bubble prior to pinch-off [116].

The results in Figure 2.12 revealed that start of pinch-off occurs when there is a reversal in the flow of the continuous flow at the top and bottom walls as clearly seen in the velocity fields. This flow reversal can be explained by the sudden change in the hydrodynamic resistances of the dispersed phase channel where at the start of pinch-off the resistance at the T-junction side channel is lower than that of the main stream channel containing the bubble. They reported this flow pattern is more pronounced close to the top and bottom channel walls [116]. The consequence of the

flow reversal is that it will speed the pinching process of the droplet. The findings of Van Steijn *et al.* [116] indicated that there are complex flow patterns that occur inside the continuous phase during the pinch-off of the droplet. It should be pointed out that the results presented by Van Steijn *et al.* [116] were limited to gas/liquid systems and low Ca. It is expected that the velocity patterns during droplet generation at higher Ca with liquid/liquid system may differ from what was observed in gas/liquid systems.

The examination of the role of pressure build up at the interface between the dispersed phase and continuous phase at a T-junction droplet generator was reported by Malsch *et al.* [117]. The buildup of pressure was achieved using elastic tubing for the fluid source. Thus, the pressure in the fluid feed tubing will increase until it reaches a pressure higher than the continuous phase at the entrance of the T-junction, then the fluid will enter the main channel forming a droplet. However, the exact pressure changes during this process were not measured due to difficulties probing changes of pressure at the microscale.

Their study was performed with both μPIV and high speed bright field imaging of the droplet generator [117]. The droplets were formed in a glass chip. The solutions used were Decalin as the continuous phase and NH_4SCN solution as the dispersed phase. Malsch *et al.* [117] results showed that the droplet generation system is affected with the pressure changes between the dispersed phase and continuous phase [117].

The velocity patterns inside droplets are complex and difficult to experimentally measure in regular μPIV with high precision because of the relatively large focal depth and depth of correlation [92, 93]. An improvement to the optical properties of typical μPIV systems can be achieved with confocal microscopy that allows for elimination of the out of focus effects of particles for the recorded images [118]. The first publication of a 3D map of the velocity patterns in droplets during the generation process with μPIV and confocal approach was presented by Kinoshita *et al.* [119] using a T-junction generator made from PDMS. The solutions used were silicone oil as the continuous phase and water-glycerol solution as the dispersed phase. Fluorescent particles with $d_p = 500\ nm$ were used as tracking particles in

the water-phase. A CW diode laser was used to illuminate the flow field and images were acquired with a high speed CMOS camera (Phantom 7.1, Vision Research , Inc, USA) [119].

The work of Kinoshita *et al.* [119] showed that the velocity patterns inside droplets are complex due to the confinement condition (the lubrication and gutter regions) and flow conditions. Their study showed the applicability of using confocal μPIV to examine the internal flow in droplets. The only concern about the work presented by Kinoshita *et al.* [119] was the relatively long exposure time needed to illuminate the particles and capture the images. The exposure time was 0.5 s which was limited by the time needed for the CMOS sensor to capture adequate images. Thus, the use of confocal microscpy along with μPIV is limited to low Ca.

One important point to mention about reported μPIV droplet generation studies is that most, if not all, studies were limited to the squeezing regime ($Ca < 0.002$). This is due to the challenges associated with image acquisition and phase locking droplets at high values of Ca. These were motivators for quantitatively studying the droplet generation regimes at the transition and dripping regimes, as will be presented in Chapter 4.

2.4 Transport of Fluid Segments in Channels

After the generation of droplets comes the process of transporting them through the channel network towards the regions of interest. Usually a pressure gradient in the microchannel $\left(\frac{\partial P}{\partial l}\right)$ larger than the added flow resistance from the droplet is needed to transport the droplets. The action of droplet motion affects the shape and added resistance of the droplet. Thus, examining the work that had been done on the simple geometries or fluid/fluid condition is a good starting point that can lead to a better understanding of liquid droplet transport in rectangular microchannels.

2.4.1 Transport of Fluid Segments in Capillaries

The simplest two phase flow condition in small scale geometries is the condition of gas/liquid flow in circular capillaries. Gas/liquid segmented flow in capillaries have been under research from as early as the beginnings of the 20th century by many fluid dynamicists including Taylor and Bretherton [4, 52, 120]. Early research was mostly experimental with analytical approximations with scaling approaches and was directed towards understanding the transport of segmented flow. Experiments those days utilized smart approaches for measuring the flow properties such as measuring the volume of the dispensed fluid then retrieving the expected volume of the lubrication region and measuring the changes in the electrical resistance between the conditions of presence and absence of bubbles to estimate the volume of the lubrication region properties [4, 52, 120].

One of the most cited works of segmented gas flow in capillaries is the work of Bretherton [4] where he experimentally examined the flow of long bubbles in a filled capillary and also provided theoretical models describing the motion of bubbles. The bubble that Bretherton studied was relatively long compared to the diameter of the capillary. This condition resulted in the bubble having multiple regions with respect to the flow. The main regions were: the leading edge, lubrication region, and the trailing edge region. Since the gas has low viscosity the pressure inside the bubble was assumed to be constant. A typical image of the shape of the bubble that Bretherton studied is presented in Figure 2.13. The shapes of the leading and trailing edge are affected by the surface tension. The flow in the lubrication region (CD in Figure 2.13) is mainly affected by the approximated unidirectional flow in the lubrication region. The bubble motion inside the capillary leads to shaping the leading and trailing edge according to the interfacial tension with the leading edge having an extended profile. Hence, the pressure drop of the bubble leading edge is higher than that of the trailing edge which gives a rise to the pressure drop across the bubble.

Bretherton's work revealed that the velocity of the bubble was faster than the average velocity of the liquid in the channel. From his work the ratio of the bubble

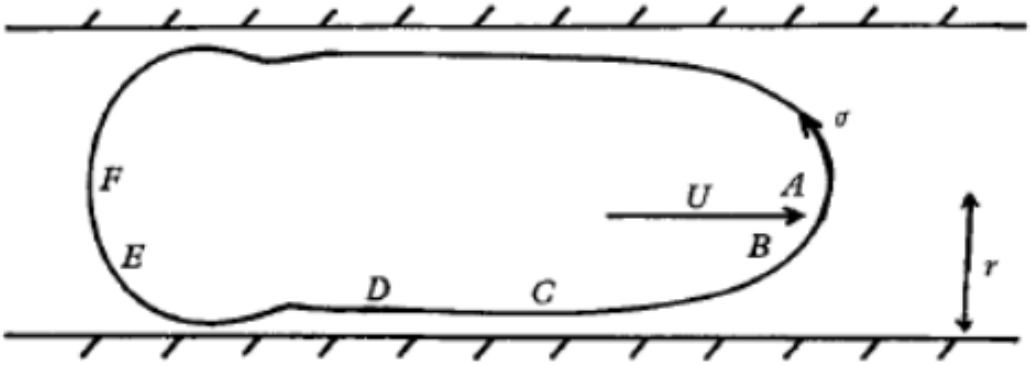

Figure 2.13: An illustration of the bubble shape that was modeled by Bretherton [4]. The bubble regions are: AB: leading edge, BC: transition from leading edge to lubrication region, CD: lubrication region with uniform thickness, DE: transition from lubrication region to trailing edge, and EF: trailing edge of the bubble. The figure was taken from [4].

velocity compared to the liquid velocity was found to match:

$$\frac{u_b - u_m}{u_b} = 1.29 \cdot (3Ca)^{2/3} \tag{2.10}$$

where u_b is the speed of the bubble, u_m is the average speed of the liquid, and Ca is the capillary number. The physical explanation for having the bubble velocity faster than the average velocity of the liquid phase is that the bubble occupies most of the capillary and will have a small region of lubrication that will reduce friction with the wall. The bubble endures the two dimensional velocity field that has a maximum value at the mid region of the channel.

From the results that bubble velocity was higher than that of the continuous phase the bubble motion in a capillary was given an analogy to a leaky piston [4, 38]. The other two parameters that Brertherton found were the thickness of the lubrication film and excess pressure that is added because of the existence of the bubble. Equations 2.11, 2.12 present the relations that Bretherton proposed for change in the

lubrication film and the excess pressure against the capillary number [52]:

$$\frac{h_\infty}{R} = 0.643 \cdot (3Ca)^{2/3} \tag{2.11}$$

$$\frac{\triangle P}{\gamma/R} = 4.52 \cdot (3Ca)^{2/3} \tag{2.12}$$

where h_∞ is the thickness of the lubrication region, R is the radius of the capillary, Ca is the capillary number, $\triangle P$ is the added excess pressure from the presence of the bubble, and γ is the interfacial tension. From Equations 2.11, 2.12 both the thickness of the lubrication film that surrounds a bubble and pressure drop change with Ca. It should be pointed out that the experimental results presented by Bretherton did not match his approximation models at low Ca.

The work of Bretherton [4] was emphasized here, and in the literature of two phase flow, because it offered an explanation of the flow aspects of two phase gas/liquid flow in small scale geometries. Gas/liquid studies that followed Bretherton aimed to prove the accuracy of his analysis.

Later work examined the flow of gas segments in a liquid phase with experimental and numerical approaches and tried to find friction loss coefficients that can be applied to describe a flow in a capillary and aid with the design of the gas/liquid systems [41, 42, 121]. Results showed that the approximations that were proposed by Bretherton were valid and applicable for describing gas liquid flow in capillaries [41, 42, 121].

An example of the study of gas/liquid flow in small scale capillaries was presented by Kawahara *et al.* [41]. In their work they experimentally examined the distinct two phase flow patterns and pressure drop for the combination of N_2 and water in silica capillaries. One of the observations that they reported is that at higher flow rates, or Ca, the flow patterns are not stable and will be intermittent. Also in their work they provided a model that estimates the pressure drop in a capillary containing gas liquid flow based on the void fraction of the flow [41].

The transport of liquid segments in capillaries is more complex compared to the

transport of gas segments in capillaries. The viscosity of the dispersed phase affects the hydrodynamic properties of droplets during their transport [52]. Also, the presence of a viscous fluid alters the boundary condition at the fluid/fluid interface from a stress-free condition in the case of ideal gas/liquid systems to no-slip condition [52]. These differences will influence the hydrodynamic properties of droplets in circular capillaries. There were many numerical and experimental studies that focused on the transport of liquid segments in capillaries [122, 123, 124, 125]. Experimental studies examined both the average hydrodynamic properties for transporting a train of droplets [41] or single droplet properties [123]. Most numerical studies focused on the single droplet properties and the change of the hydrodynamic properties of the flow, such as thickness of the lubrication region [124, 125].

Jovanović *et al.* [123] experimentally studied the hydrodynamics of liquid segments and the pressure drop of individual liquid segments in silica capillaries and compared the results with two proposed models. The two models differ on how to treat the lubrication region surrounding a droplet. The first model takes a stagnant film approach and the second approach considers a moving film approach. They took into consideration the contribution of all pressure drop contributors and formulated the total pressure drop according to:

$$\triangle P_{total} = \triangle P_{dispersed} + \triangle P_{continuous} + \triangle P_{interfacial} \tag{2.13}$$

where $\triangle P_{total}$ is the total pressure drop in the capillary, $\triangle P_{dispersed}$ is the pressure drop associated with the bulk fluid content of the dispersed phase, $\triangle P_{continuous}$ is the pressure drop associated with the carrier continuous phase, and $\triangle P_{interfacial}$ is the pressure drop from the curved interface that is formed because of the interfacial tension between the fluids. Their experimental findings showed that treating the film that surrounds the fluid segment as a stagnant film gives a good estimation for the pressure drop of droplets and was very close to the measured pressure drop [123]. In their work they also attempted to optically measure the thickness of the lubrication region that surrounds a droplet. Their measurements showed that changes in the lubrication regions for liquid/liquid segments were in the same order of what Bretherton [4] had estimated before for gas/liquid systems.

2.4.2 Transport of Fluid Segments in Rectangular Channels

The complexity of the transport of fluid segments will increase when the cross section shape of the channel is non-circular. The reason for the complexity is the change in the confinement condition. The lubrication regions in rectangular channels will have two main parts: gutter regions located at corner walls, and thin film regions that separate the bulk of the fluid segment from the walls. Complexity of droplet flow arises since the size of the gutter regions and relative motion of the continuous phase in the gutter regions will have a direct impact on the hydrodynamics of droplet transport. Similar to what was done with fluid/fluid flow in capillaries the next discussions will first present a brief overview of gas/liquid systems and then liquid/liquid systems in rectangular microchannels.

Interest in gas/liquid flow in rectangular shaped channels was an expected progression after studying the transport of gas/liquid transport in capillaries. Also, one motivator was to understand the flow in industrial systems that have small rectangular shaped channels that support segmented gas liquid flows, such as monolith reactors [126]. Research on two phase gas/liquid systems in rectangular shaped channels had been performed with experimental or numerical approaches [126, 127, 128, 129]. Experimental studies were performed on mm to μm sized channels with a focus on the generated flow patterns and the bulk average pressure drop of segmented flows [126, 127, 128, 129].

Fries *et al.* [5] studied the hydrodynamic properties of gas segments carried by various liquids. In their work they performed optical examination of the thickness of the lubrication regions in the 200 μm square channel with laser scanning confocal microscopy (LSM). The principle of the LSM and typical images recorded by the system are presented in Figure 2.14.

The experimental results presented in Figure 2.14 -(b) show the relative size of the corner gutter thickness compared to the wall lubrication regions. Fries *et al.* [5] reported that at low $Ca < 0.001$ the thickness of the gutter region is independent of Ca. Moreover, Fries *et al.* [5] also proposed a pressure drop model that was based on the void fraction condition that occurs during the transport of a train of droplets.

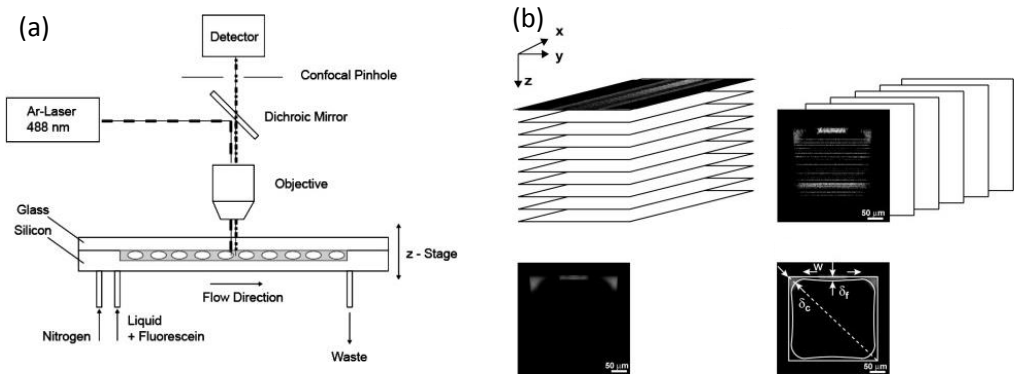

Figure 2.14: A schematic of the experimental approach used by Fries *et al.* [5] to study gas/liquid transport properties in square microchannels. Typical outcomes from their experiments are presented in the figure. Included with permission.

Their model showed good agreement with their experimental results.

An interesting reading that reviewed some the important literature of segmented gas flow in capillaries and rectangular channels was presented by Kreutzer *et al.* [130]. In their review they summarized the important factors and phenomena that are of interest to researchers of segmented gas/liquid flows in capillaries and rectangular microchannels. One important property that they reported was the difference in the thickness of the lubrication regions between circular and rectangular microchannels [130]. According to what they reviewed the thickness of the lubrication regions in rectangular microchannels is a function of Ca. Also, the ratio of the thicknesses between the corner (gutter) thickness compared to the thin film thickness is estimated by:

$$\frac{h_{g,square}}{h_{\infty}} = 0.7 + 0.5 \cdot Exp(-2.25 \cdot Ca^{0.445}) \tag{2.14}$$

where $h_{g,square}$ is the film thickness from the edge of the corner, h_{∞} is the expected film thickness from a circular channel. The film thickness estimated in Equation 2.14

is only for the gutter region and does not represent the film region that separates the bulk of the droplet from the side walls. The thickness of the lubrication film region is estimated by:

$$h_{\infty,square} = 0.6933 - 0.0977 \ln(Ca) \tag{2.15}$$

where $h_{\infty,square}$ is the film thickness that separates the walls of the square channel from the gas bubble. It should be pointed out that Equations 2.14 -2.15 were correlated from experimental results [130]. The estimations of the film thickness surrounding a bubble in square microchannels can give an idea on the order of magnitudes of the film thicknesses that surround liquid droplets, similar to what was presented earlier in capillary flows. Although, in real conditions the estimations of the lubrication region might differ from real situations that bubbles endure, they still can give approximations to the changes in the confinement condition.

From the brief review of some of the literature of segmented two phase flow in capillaries and rectangular microchannels it can be sensed that the area is vast and could not be covered in one chapter, nor in one book. The many flow patterns that can occur depending on the flow, fluids, and confinement condition adds to the complexity of the flow phenomenon. However, the brief overview discussed above aimed to present some of major work and approaches used by researchers to examine the flow properties of segmented flow patterns in circular and rectangular channels.

Segmented Liquid/Liquid Flow in Rectangular Microchannels

After presenting an overview of some of the work that had been done on the hydrodynamic segmented fluid/fluid flow in capillaries and gas/liquid flow in rectangular channels attention will be directed towards liquid/liquid studies in rectangular microchannels. The transport of liquid droplets in rectangular microchannels has been studied with numerical and experimental approaches with an aim to understand the behavior of droplets in rectangular microchannels [34, 38, 131]. The studies were motivated by the necessity of knowing the droplet transport properties for proper design of complex microfluidic systems that will be used for handling and the controlling of individual or trains of droplets. Complex transport processes such as droplet

merging [132], droplet splitting [133, 134], and droplet sorting [135, 136] are some of the flow control processes that were studied in microchannels with droplets. Among the transport properties of droplets the excess pressure of droplets (ΔP_{drop}) is important since it can be used to find the nature of hydrodynamic resistance change in microchannels. This property is affected by the flow conditions, droplet geometrical shape and fluid types [6, 34, 38, 72, 137]. Thus, assessment of the excess pressure (ΔP_{drop}) is important for design of complex droplet systems. Furthermore, knowledge of the magnitudes and changes of the excess pressure (ΔP_{drop}) with respect to experimental conditions is crucial. It should be pointed out that other hydrodynamic properties of droplets such as the hydrodynamic resistance of droplets ($R_{hyd,drop}$) are related to the excess pressure (ΔP_{drop}) by the geometrical properties of droplets.

Focus will be directed towards experimental techniques over numerical approaches since they offer measurements of the actual hydrodynamic properties of droplets in real operation conditions compared to the local droplet changes that are usually estimated by the numerical simulations. Generally there are two experimental approaches for measuring the excess pressure added by droplets in microchannels, these are: direct and indirect. In direct methods the pressure is directly measured with pressure sensors at channel sections where droplets are present [72, 137]. Indirect methods are based on measuring other flow properties and inferring the pressure drop from the relationship between the measured property and the pressure drop. For example measuring the flow rate in the presence and absence of droplets can be used to estimate the droplet excess pressure [6, 137]. Typical examples of a direct and an indirect measurement approach are presented in Figure 2.15.

From the literature Adzima and Velankar [72] used a direct approach to measure the hydrodynamic properties of droplets in rectangular microchannels. In their approach they compared the measured pressure drop in the absence of droplets to the pressure drop in the presence of droplets and calculated the hydrodynamic resistance of droplets, as seen in Figure 2.15 -(a). The fluids that were used by Adzima and Velankar [72] were hexadecane with Span 80 as the continuous phase and water as the dispersed phase. Their results showed that the added pressure from droplets is a function of the size of droplet [72].

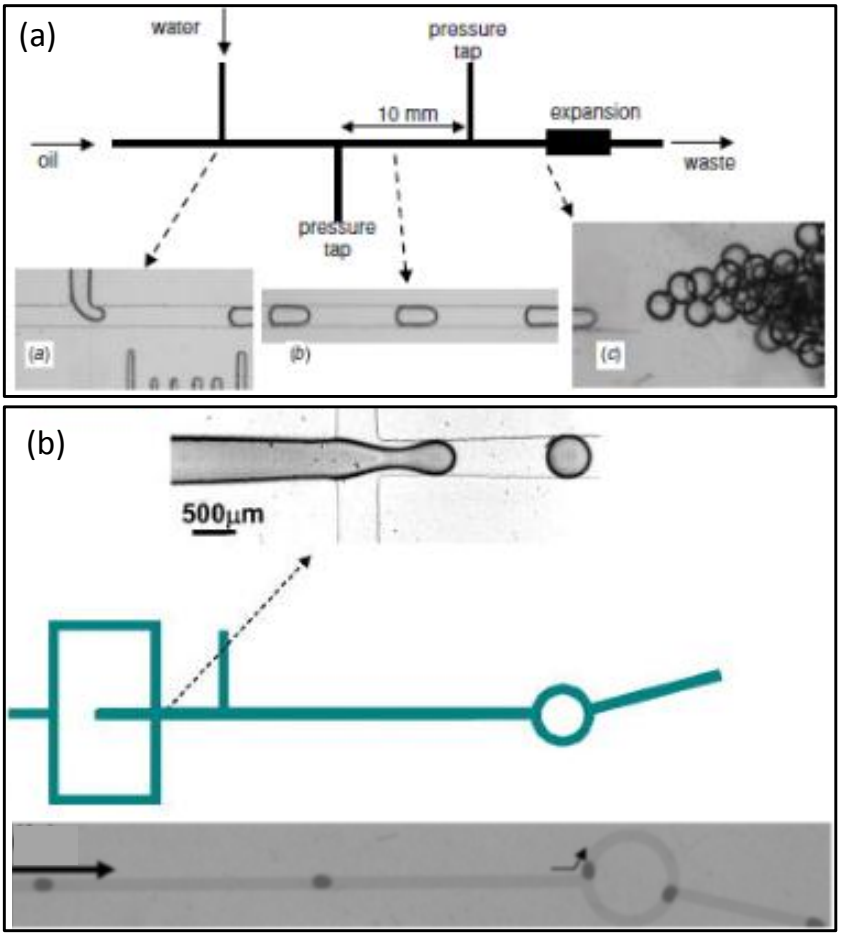

Figure 2.15: A direct and an indirect approach used to examine the hydrodynamic properties of liquid droplets in rectangular microchannels. Figure (a) The channel network design for a direct droplet pressure measurement approach reported by Adzima and Velankar [72], and (b) The channel design with images of droplet generation and transport of the indirect droplet pressure measurement approach reported by Labrot *et al.* [137] (Used with permission.).

There are some issues that should be mentioned about the work of Adzima and Velankar [72]. First in their calibration for the pressure and flow rate relation without droplets the relation showed a non-linear pressure (P) and flow rate (Q) relation. This trend is not expected for laminar flow in microchannels and the authors acknowledged that it was unexpected but they didn't offer a decisive explanation for it, nor its effect on their measurements. Also, although acknowledging that swelling PDMS is present they performed calculations by neglecting its effect. Nonetheless, the work of Adzima and Velankar [72] was the first in microchannels that used a direct approach to measure the excess pressure.

Labrot *et al.* [137] measured the pressure drop of water/glycerol droplets in oil with both a direct and indirect approach. Their indirect approach was based on finding the trafficking pattern for trains of droplets when they come into splitting junctions of channels with different hydrodynamic resistances (See Figure 2.15 -(b)). The advantage of this approach is that it is simple to implement in the microchannels without the addition of complex devices that may influence the flow. Their indirect approach was done with two types of designs: a small loop design and a large loop design. Labrot *et al.* [137] defined an equivalent droplet length $L_{d,e}$ as a measure of the added resistance of droplets. This length was calculated from the expected hydrodynamic resistance of a rectangular channel. They proved that indirect approaches can estimate the pressure drop associated with the addition of droplets with the same order of magnitude of accuracy as the direct pressure measurement.

The results of Labrot *et al.* [137] confirmed the relation between the added resistance with the size of droplets [137]. An interesting finding that they reported is that the viscosity ratio between the dispersed phase and the continuous phase will have no effect on the droplet resistance when the ratio is below 1 $\left(\frac{\mu_d}{\mu_c} \leq 1\right)$. When the viscosity ratio is above 1 $\left(\frac{\mu_d}{\mu_c} > 1\right)$ the viscosity of the dispersed phase influenced the droplets resistance. They attribute this increase of droplet resistance to the change of viscous dissipation as well as the change in the flow patterns inside and between droplets.

A parameter that affected the overall resistance of a train of droplets that Labrot *et*

al. [137] reported was the distance between droplets (droplet spacing λ). They reported that if the distance between droplets is smaller than 6 mm in their experiments the measured resistance will be smaller than what it should be. The explanation for this trend is that there is a cooperative effect where a train of droplets with small spacing between them will reduce the apparent droplet resistance [137].

Fuerstman *et al.* [62] used an indirect approach to estimate the pressure drop of bubbles where they recorded the patterns of bubble transport and sorting choice through two identical channel junctions. From the number of bubbles that move in a channel and their size the bubbles pressure drop was estimated. Fuerstman *et al.* [62] also examined the effect of adding different concentrations of surfactants on the pressure drop of bubbles in microchannels. They found that the slip factor $\left(\beta = \frac{u_b}{u_m}\right)$ for bubbles was less than 1 when surfactants were used. This result indicated that the carrier liquid speeds up in the gutter regions and passes the bubble. Another interesting finding was that the resistance of the bubbles depends on the concentration of surfactant used. If no surfactants were present or very high concentration of surfactants the pressure drop along bubbles is dominated by the leading and trailing curved interfaces. In contrast, at moderate surfactant concentrations the pressure drop is dominated by the length of bubble.

Jin *et al.* [15] measured the resistance of liquid droplets by monitoring the motion of an optically trapped particle. Their approach used a two stream channel one for the transport of droplets and the other where a particle is optically trapped. By examining the displacement of the particle due to the change in the flow in the main channel an estimation of the added resistance of a droplet can be found. They examined the resistance of water droplets in hexadecane with Span 80, and hexadecane droplets in water without any surfactant. Jin *et al.* [15] showed that the excess pressure (ΔP_{drop}) from the droplet increases with the length of droplet up to a certain value where after it the excess pressure decreases with increasing length of a droplet.

One unique approach that examined the resistance of droplets in rectangular microchannels was presented by Vanapalli *et al.* [6]. Their approach relied on creating a comparator merging chamber for two channel networks with similar hydrodynamic

resistances and pumping the same fluid. If one channel had a larger flow rate, or there was a cause of pressure drop, it will case a deflection in the flow pattern at the comparator region. Changes in the flow pattern were identified by using a dye added to one stream of the continuous phase fluid. Figure 2.16 illustrates the comparator approach used by Vanapalli *et al.* [6] along with typical images of the different stages of the experiment.

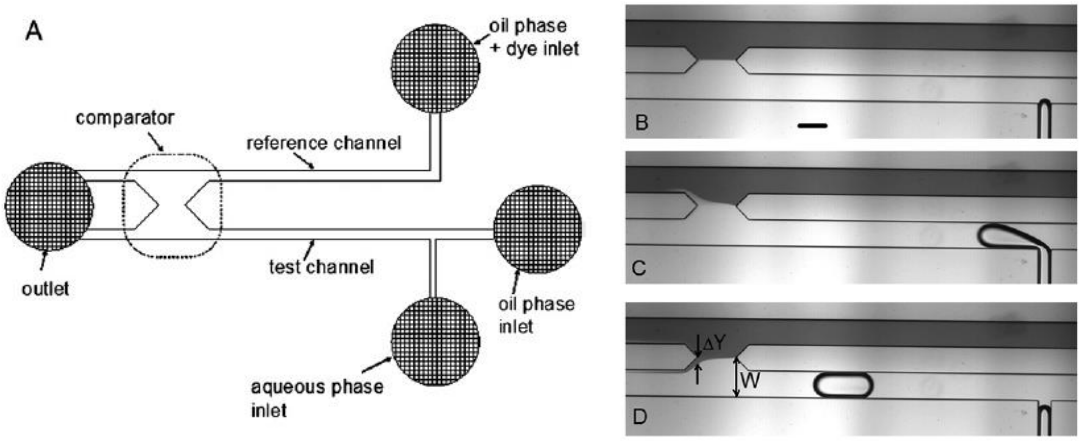

Figure 2.16: A schematic of the comparator approach that was used by Vanapalli *et al.* [6] to measure the hydrodynamic resistance of droplets. Figure (A) A schematic of the channel networks that lead to the comparator region, (B) The balanced flow rates in the absence of any droplets, (C) The deflection at the comparator during droplet generation, and (D) Deflection at the comparator as the droplet migrates in a microchannel. The Figure was taken with permission from Vanapalli *et al.* [6] (Copyright 2010 Royal Chemical Society).

Vanapalli *et al.* [6] used mineral oil as the continuous phase and deionized (DI) water with various ratios of glycerol as the dispersed phase. Sudan Black B dye was added to mineral oil to add contrast to one of the oil streams and was pumped through one side of the network. Their work examined the effect of viscosity contrast, size of droplets and Ca on the excess pressure of droplets.

Vanapalli *et al.* [6] found some interesting results regarding the resistance of droplets in microchannels. They reported that the excess pressure is independent of

Ca for small droplet sizes that they were able to measure. It should be pointed out that the smallest droplet size that they studied was at least $1.5 \cdot w_c$ of the channel. A summary of the important work in the literature that examined the resistance of droplets or bubbles in microchannels is presented in Table 2.3.

From what was presented in the literature review about the measurement of droplet properties there are several concerns regarding the measurement approaches. First, most of the studies for measuring droplet resistance were performed in PDMS which has a pressure compliance [25, 138]. This inherent property of PDMS could be a source of error in the measurement. Secondly, PDMS swells with most oils that are used in segmented liquid/liquid flow [7]. The extent of swelling, unfortunately, could not be accurately measured in real conditions and thus its effect on the transport properties of droplets is not known. Thirdly, the hydrodynamic properties of small confined droplets that are close to the channel width (non-dimensional length of $1 \leq \frac{L_d}{w_c} \leq 1.5$) were not reported due to experimental challenges associated with droplet generation and hydrodynamic measurement techniques. Fourthly, the effect of surfactants presence on the hydrodynamic properties of droplets hasn't received attention for microfluidic liquid/liquid droplet system. These questions were the source of motivations for studying the hydrodynamic properties of small liquid droplets in PC microchannels. The work on this project involved the design process of a channel network that allowed for generating evenly spaced monodisperse small droplets, surface treatment to alter the surface properties of PC for stable droplet generation, and the measurement approach. These major parts of the project will be discussed in Sections 3.1.2.2, Chapter 5, and Chapter 6.

Table 2.3: A summary of some important work that examined droplet excess pressure in rectangular microchannels. Important information is included such as: the channel material, fluids used and major finding of each work.

Ref.	**Channel Material**	**Fluids**	**Approach**	**Notes**
1	PDMS	Hexadecane + Span 80 and Water	Direct	Droplet excess pressure is a function of drop volume
2	PDMS	Oil and combinations of water/glycerol mixtures	Direct and indirect	Factors that were examined: droplet volume, spacing between droplets, and viscosity ratio. Drop viscosity does not play a role up to a certain value. Spacing between droplets can affect the total resistance of droplets.
3	PDMS	Gas bubbles in Water/glycerol with surfactants (SDS and Tween 20)	Indirect	The concentration of surfactant will have an impact on the hydrodynamic resistance of bubbles.
4	PDMS	Mineral oil and water/glycerol mixture	Indirect	Effect of size of droplet, *Ca* and viscosity ratio. Results show two regimes depending on droplet size.
5	PDMS	water droplets in Hexadecane with Span 80 and Hexadecane droplet in water.	Indirect	There is a relation between the length of droplet and the resistance. The relation depends of the *Ca*.

Cited literature: 1- Adzima and Velankar [72], 2- Labrot *et al.* [137], 3- Fuerstman *et al.* [62], 4- Vanapalli *et al.* [6], and 5- Jin *et al.* [15].

Chapter 3

Microchannel Designs, Fabrication, Fluids, and Experimental Systems

3.1 Microchannel Designs, Materials, and Fabrication

There were two main projects that were performed in this work: a quantitative study of droplet generation with μPIV, and droplets transport studies. Every project had its distinct microchannel design and specific fabrication procedure. Reasons for choosing a design and a specific channel material over other material options for each project will be explained. Also, the fabrication process for each channel material with its specific design will be presented.

3.1.1 μPIV Channel Design, Materials and Channel Fabrication

3.1.1.1 μPIV Study Channel Designs

The microchannel design that was used in μPIV experiments needed to have a T-junction droplet generator and a droplet detection region immediately after it.

The detection region should accommodate fiber optics that were aligned close to the region of interest (ROI). The optical fibers were positioned at the ROI with waveguides. These fibers were connected to a light source and a detector that were used for sensing presence of droplets. The principle of operation of droplets detection and the optimization process of the system are discussed in Appendix A.

Polydimethylsiloxane (PDMS) was chosen as the channel material for the studies of droplets generation with the μPIV system for various reasons. First, PDMS can be fabricated in-house in a fast manner. Secondly, insertion of fiber optics into waveguides is delicate and fibers are prone to break off. The breaking of fibers occurs since they lose their flexibility by removing the coating (fiber jacket) which leaves the cladding and fiber core. If a fiber breaks inside a waveguide it is hard, if not impossible, to extract it and the microfluidic chip cannot be used. Thus, it is better to have an easy to fabricate microchannel material as a channel substrate. Thirdly, silicone oil (the continuous phase) naturally wets PDMS. Fourth, PDMS has a similar refractive index to the silicone oil (refractive index of silicone oil 1.99). Thus, it is optically favorable to use PDMS in μPIV studies.

The channel design consists of a T-junction segment generator that is connected to a main stream channel. Both the side T-junction channel and the main stream channel had large hydrodynamic resistances for stable droplet generation [59, 58]. A typical illustration of the design of the channel is shown in Figure 3.1 -(b). The waveguide widths were chosen to be 140 μm so that they can accommodate the fibers (125 μm) that will be inserted through them.

3.1.1.2 Materials for PDMS Microchannel Fabrication

Microchannels that were used in the μPIV study were made from PDMS with the soft lithography technique. The underlying principle of soft lithography is that liquid PDMS when cured replicates the mold that it covers. For that reason a master mold was fabricated with UV sensitive photoresist where only the regions of the channel network design were hardened. An illustration of the fabrication procedure is presented in Figure 3.1 -(a). The details of the developed in-house soft lithography

fabrication protocol will be presented later. The materials that were used in the microchannel fabrication can be listed as follows:

- Microchem photoresist (SU8-2005,2075, Microchem)
- PDMS base and curing agent (Sylgard 184 silicone elastomer kit, Dow Corning).
- Silicon wafer (WRS Materials).
- Glass slides (VWR).

3.1.1.3 PDMS Microchannel Fabrication

The main steps for the fabrication of microchannels for μPIV studies are described below:

Fabrication of silicon wafer with hardened microchannel features: This fabrication process involved a multilayer coating of SU8 photoresist on a silicon wafer and curing the desired regions of the microchannel network. The procedure for creating channel features on a silicon wafer was done as follows:

1. Dehydrate the silicon wafer by placing it on a hot plate at 200^o for 10 min. Afterwards, wait for 10 min to cool down before spin coating SU8 photoresist.
2. Spin coating SU8-2005 to a thickness of 5 μm. Then, perform the soft bake procedure according the SU8 manual. Finally expose the coated wafer to UV to graft the SU8.
3. Spin coat SU8-2075 to a height of 74 μm. This step was done twice to reach a height of 148 μm for the hardened SU8. Between the steps of spin coating proper soft bake times were done on the coated wafer.

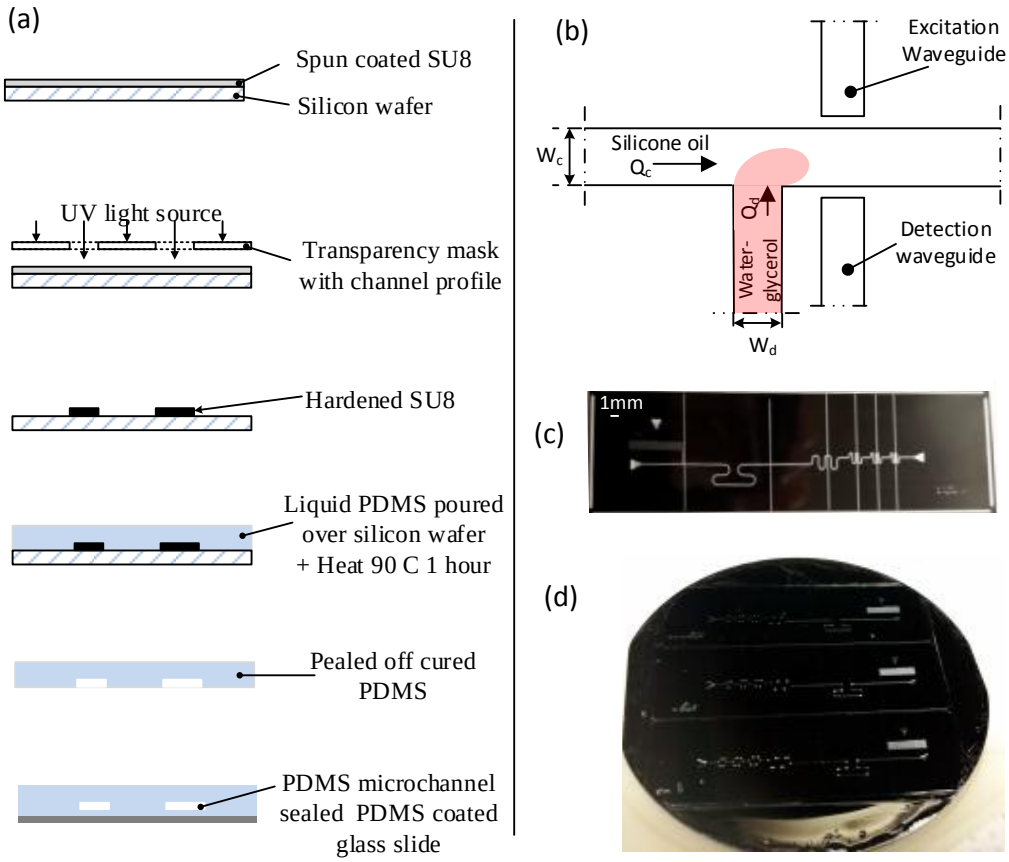

Figure 3.1: An illustration of the PDMS microchannel fabrication with images and schematics of important parts of the fabrication. Figures according to their labels: (a) A simple flowchart of the fabrication principle of soft lithography, (b) Design principle of the T-junction of the microchannel, (c) Transparent print containing the design, and (d) Silicon wafer containing hardened SU8 microchannel features.

4. Cover the SU8 coated silicon wafer with the transparency mask (20,000 dpi, CAD/Arts) that contains the channel network designs (see Figure 3.1 -(c)). Then expose the silicon wafer with UV light. The regions of SU8 that that were exposed to UV light were hardened.

5. Remove the uncured SU-8 with SU-8 developer.

Replication of hardened master: The PDMS base and curing agent were mixed with 10:1 w/w and degassed in a vacuum oven with a vacuum of 172 kPa (25 psi) for 30 min. Afterwards, liquid PDMS was poured over the silicon wafer that contained the channel designs (see Figure 3.1 -(d)). The liquid PDMS was cured on a hotplate at 90 C for 1 hr. Afterwards, the cured PDMS was then removed and access ports were then punched with a 2 mm biopsy punch.

Substrate fabrication: The substrate of the microchannel was a glass slide coated with PDMS. The coating was done by spin-coating liquid PDMS (10:1 base to curing agent) at 1300 rpm. Then, the glass slides were put on a hotplate at 90^oC for at least 10 min.

Channel bonding: The cured PDMS that contained channel features and glass slides covered with PDMS were cleaned with acetone, deionized water, and dried with N_2 gas. Afterwards, both cured PDMS and coated glass slides were exposed to O_2 plasma for 8 s. The system that was used was PDC-001 Harrick plasma cleaner. The other settings for the treatment were: 66.7 Pa vacuum (500 mTorr), and power of 29.6 W.

An undesired outcome of the plasma treatment is the change of the surface to a hydrophilic state. This rendered hydrophilic state will not support the stable generation of water droplets in silicone oil. However, the PDMS recovers back to a hydrophobic condition with the aid of heat treatment. For that reason all bonded chips were put on a hotplate at 190^oC for at least one day [64].

3.1.2 Droplet Transport Channel Designs, Materials, and Fabrication

Droplet transport studies were performed in Polycarbonate (PC) microchannels because of the advantages of PC compared to PDMS. The main benefits of PC include: PC does not swell when exposed to oils that are commonly used by researchers in the microfluidics community. Secondly, PC resists geometrical changes with pressure that are used to pump fluids in microchannels. Thirdly, PC surfaces can be altered to a hydrophobic condition for stable droplet generation.

There were two main versions of PC microchannel networks that were fabricated throughout this work. The first type of designs was an in-house fabricated simple T-junction designs, and the second type of designs was more complex with multiple inlets and different zones. The first type of designs was used to optimize surface treatment of PC with Dodecylamine (DDA) to have stable wetting properties. The second types of designs were used in the droplet hydrodynamic studies. Details about the design aspects and fabrication procedure of each design version will be presented next.

3.1.2.1 PC Design 1, Design, Materials, and Fabrication

Design 1 Properties: The main purpose of this design was to optimize the surface treatment of PC. Thus, it should be simple, and easy to fabricate. For those reasons, simple T-junction designs were used. One side of the T-junction is at least twice as long as the short side. The fabrication of these designs was done by a milling machine located at the UW student machine shop.

Materials used for Designs 1: Materials used for the fabrication of Design 1 can be listed as follows:

- Two sizes of industrial grade PC with thicknesses of 6 mm and 2.5 mm. The length and width of the pieces used were $7.5 \times 4cm^2$.
- Stainless steel tubing with OD 1/16" and ID 1/48" or 1/32". These tubing were used to interface the inlets ports of the microchannel with tefon tubing.
- Teflon tubing with an outside diameter (OD) 1/16" and an inside diameter (ID) of 1/32". This tubing was used to interface the fluid source with the microchannel stainless connectors.
- Proper connectors to interface the fluid sources with the tubing and inlet ports (Upchurch connectors).

Fabrication of Design 1: The T-junction design was machined on a slab of PC with a milling machine. PC slabs with $75 \times 40 \times 6\ mm^3$ (l × w × h) were used as substrate for the microchannel. The machined microchannel width and depth were $800 \times 800\mu m^2$. The lengths of the channel section ranged from 4.5 to 5.5 cm for the long branch of the T-junction. The short branch of the T-junction length ranged between 2.5 to 3 cm. After machining the channel ports for the fluid connectors were drilled. Then the ports were threaded with a tap size (0-80) to match the thread on the stainless steel tubing. It was used to interface the fluid sources with the tubing. Afterwards the machined parts of the channel were cleaned in an ultrasonic bath and detergent then washed with water.

The substrate of the microchannel was a slab of PC that had the same width and length but with a 2.5 mm height. Creating a permanent bond between separate pieces of thermoplastic is achieved by establishing chemical bonds between molecules at the surface of the separate pieces [16, 26]. The bonding of a machined PC and non-machined piece was done with a combination of solvent then applying heat and pressure. Both the machined side and the bare side of the substrate were sanded with an 800 grit sand paper. Then, both pieces were washed with water, isopropanol, and then dried with air. Afterwards, both pieces were exposed to vapors of Methyl ethyl ketone (MEK) for 75 sec in a fume hood. Then, the two exposed surfaces were aligned and put together and immediately placed in a Carver press to pressure seal

the exposed pieces. The Carver press was set to 120^o C and pressure was applied for 10 min. To assure uniformity of pressure that was applied on the pieces of PC steel plates along with thick cured PDMS slabs were used to sandwich the two PC pieces that were needed to be bonded. Figure 3.2 presents a typical microchannel that was used in the optimization of the surface treatment.

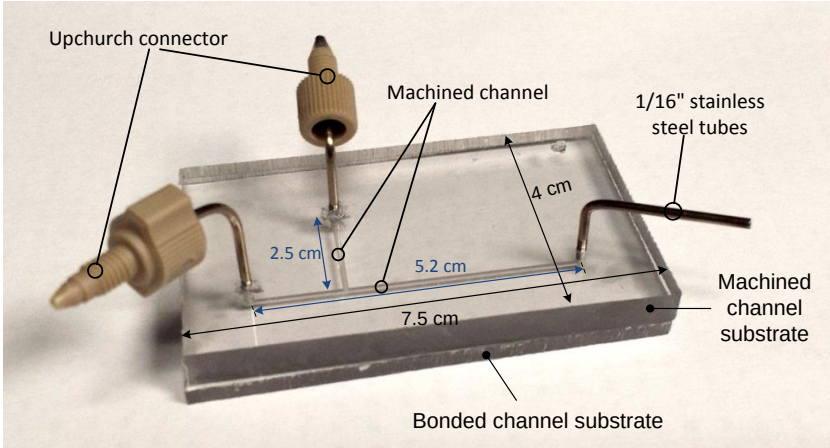

Figure 3.2: A typical PC Design 1 channel that was used in the optimization of DDA treatment. The geometrical aspects of the channel along with the other main connectors that were used to interface the chips with fluids sources are labelled in the figure.

3.1.2.2 Design of Channels in Droplet Transport Project

Microchannel networks that were used to study the hydrodynamic transport properties of droplets were designed to meet specific criteria that include: stable generation of droplets with a certain size and spacing, droplet size should be controllable to a certain degree ($L_d \geqslant W_c$), ability to change the spacing between droplets after generation, the flow rate and pressure must be known at a section of the channel network. For those reasons a four port microchannel network design was chosen as a starting point. Three of the ports are fluid source ports while the fourth one was the outlet. All of the source ports were connected to a pressure system that serves as the fluid supply with a known pressure. The first two ports (or inlets) are used

to generate droplets. The third inlet controlled spacing between pairs of droplets, while the fourth port served as the outlet of the network. This outlet was connected to a flow sensor that measures the flow rate of the pumped oil.

The details of the design for the channel network was built on the knowledge from the literature of droplet microfluidics systems and also on what was experienced at the UW microfluidics lab for passive droplet generation in T-junction microchannels made from PDMS. For example, it was reported that droplet generation in passive flow conditions is affected by changes in the hydrodynamic resistance in the channel network. This change occurs when there is an added resistance from droplets that were generated. Hence, under certain conditions changes in resistance downstream the T-junction affects the flow in T-junction generator. This effect is considered a feedback effect and was discussed in Section 2.2.1 [58].

To overcome the feedback effect the hydrodynamic resistance of the microchannel network must be high enough so that droplet generation under steady conditions is relatively isolated from what occurs downstream. The hydrodynamic resistance of a rectangular microchannel can be found from Equation 3.1 [12]:

$$R_{hyd} = \frac{12\mu L}{h^3 w} \frac{1}{\left[1 - \sum_{n=1,odd}^{\infty} \frac{1}{n^5} \frac{192}{\pi^5} \frac{h}{w} \tanh\left(n\pi \frac{w}{2h}\right)\right]} \tag{3.1}$$

where R_{hyd} is the hydrodynamic resistance of a microchannel, L is the channel length, h is the height of the channel, w is the width of the channel, and L is the length of the channel. For a channel with a width that is larger than it height ($w > h$) Equation 3.1 can be simplified to:

$$R_{hyd} = \frac{12\mu L}{h^3 w \left[1 - 0.630 \frac{h}{w}\right]} \tag{3.2}$$

Thus, for designing different parts of a microchannel network Equation 3.2 must be used to find the channel geometry to eliminate, or reduce, the feedback effect that may occur from droplets transport in the channel network.

The other design consideration was the size of the generated droplets. The droplets size is strongly influenced by the geometrical properties of the T-junction. For a T-junction with a constant height the ratio between the widths of the dispersed phase section to the continuous phase (w_d/w_c in Figure 3.1 -(b)) affects the generated droplets size. Hence, in order to study droplets that are close to the width of the measurement channel section the channel network should have a wider section compared to the T-junction. The transition of the channel width should be incremental and close to the inlet of the third port.

Based on the design considerations and general design rules presented in the literature for passive droplet generators a channel network with three regions was proposed. There were three main regions were: the droplet generation region, the droplet transport section, and the droplet resistance measurement region. The general conditions that were applied for each section of the design were:

1. The hydrodynamic resistance of the channel containing the dispersed phase must be higher than the continuous phase branch that leads to the T-junction.

2. The resistance of the channel network after the T-junction must be the highest in all the network to stabilize droplet generation and transport.

3. The hydrodynamic resistance in the region of the transport properties measurement must be less than that of the region where droplets are transported (point 2).

4. Most of the pressure drop occurs in the microchannel network and tubing connections with fluid sources must have very small resistance compared to the microchannel network.

Based on the design considerations mentioned before and design rules listed above a three region channel network design was used. The first two regions were for the T-junction generator and droplet transport. The third region is where the droplet transport properties will be measured. The third region is connected to the dilution stream and the outlet of the network. The width of the continuous channel that is

used for droplet transport was $w = 75\mu m$. The width of the channel where droplet properties were examined was $w = 100\mu m$. The height of the microchannel network was $h = 50\mu m$. The microchannel network design that was used in this project is shown in Figure 3.3.

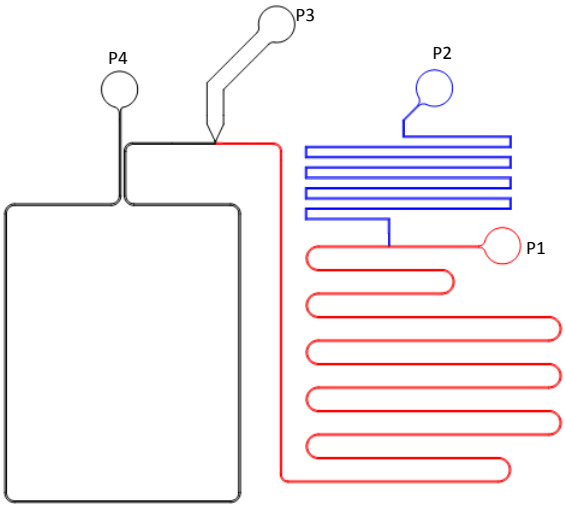

Figure 3.3: A schematic of the design that was used in the current work for the droplets transport studies. The blue region represents the channel that carries the dispersed phase, the red region represents the region where droplets are generated and transported, and the black region represents the region where the droplet resistance measurement occurs.

The three sections of the design according to the color coding in Figure 3.3 are as follows: dispersed phase section (blue region connected to P2), droplet generation and transport region (red region, connected to P1), and measurement section (black region from P3 to P4). Droplet generation occurs at the T-junction between the first and the second sections that are influenced by fluid pressures P1 and P2. The fluid junction at P3 is used as the dilution stream junction to control the spacing of pairs of droplets that are being transported in the microchannel network. P4 is connected to a flow sensor that is open to atmosphere. The actual dimensions of the design shown in Figure 3.3 are listed in Table 3.1.

The channel network that was used in the droplet transport studies was out-

sourced to an off-campus company (FlowJem, Toronto) that specialize in the fabrication of microchannel networks in thermoplastics. This is due to the fact that fabrication of microchannels with the dimensions that were commonly used ($w_c = 100\mu m$ and $h = 50\mu m$) are very difficult with commercial CNC machining systems.

Table 3.1: The dimensions of the channel network segments used in the hydrodynamic study of droplet transport.

Channel Segment	Width (μm)	Length (mm)
Dispersed region (Blue)	75	107.4
Continuous region (Red)	75	179.3
Measurement Region (Black)	100	77.3

3.2 Fluids

There were various combinations of fluids used in the current studies. There were fluids that were used as experimentation fluids, and fluids that were used for the surface treatment of microchannels. The various types of fluids used are presented next.

3.2.1 Fluids used in the μPIV Experiments

The fluids that were used in examining the droplet generation with the μPIV were silicone oil (10 cSt, Sigma Aldrich), water, and glycerol. Silicone oil was chosen as the continuous phase since it should naturally wet hydrophobic PDMS since it has the same chemical structure [1]. A mixture of water and glycerol was used as the dispersed phase. Glycerol was mixed with water with a mass ratio of 52 % to closely match the refractive index of silicone oil and PDMS. This refractive index was measured with a refractometer. There were two types of water-glycerol mixture that were used: with

[1]Both PDMS and Silicone oil have the Silicon (Si) attached to two Methyl (CH_3) groups [69].

or without a surfactant. The surfactant that was used was Sodium Dodecyl Sulfate (SDS, Sigma Aldrich) and it was added with a concentration of 0.57% w/w. This concentration of SDS is above the CMC. The main desired function of SDS is to lower the interfacial tension between the water-glycerol mixture and Silicone oil.

Polystyrene fluorescent particles with a diameter of $1\mu m$ (FluoSpheres 535/573, Invitrogen) were added to the dispersed phase used in each experiment. The particle concentration was 0.03 % v/v. It should be mentioned that the particles did not have an effect on the interfacial tension between the water-glycerol mixture and silicone oil. This was proven by interfacial tension measurements that were done with a Wilhelmy Plate tensiometer where the presence of the fluorescent particles did not change the interfacial tension between silicone oil and water-glycerol. The physical properties of the fluids used in the current experiments are presented in Table 3.2.

Table 3.2: Physical properties of the fluids used in the μPIV studies of droplet generation.

Fluid	Density kg/m^3	Viscosity mPa.s	Interfacial Tension mN/m	Refractive index
Water-glycerol	1147	6.41	33.2	1.395
Water-glycerol with 0.57% SDS			12.2	
Silicone Oil	930	10	-	1.399

3.2.2 Fluids used in the Droplet Transport Projects

For the droplet transport project the channels were made with Polycarbonate (PC). The surface of the PC was modified with DDA. For that reason only a limited number of fluids could be used which will wet the modified PC for stable droplet generation. From what was reported in the literature there were a couple of candidates as a continuous phase. The two that were tested were silicone oil and hexadecane. From what was observed of droplet generation at the T-junction hexadecane had better wetting properties compared to silicone oil. Thus, all experiments used hexadecane

as the continuous phase and water based solutions as the dispersed phase. In some experiments the viscosity of water was altered by adding glycerol with mass ratio of ≈ 37.2 % to closely match the viscosity of hexadecane.

In all experiments blue food dye was used to color the water based solution and it was mixed with 10% V/V. This was done to enhance the contrast between the dispersed phase and the continuous phase leading to better image processing results. The key component in the food dye was propylene glycol which does not affect the surface tension at low concentrations [139]. This was also confirmed with surface tension measurements where the addition of the dye didn't have a huge effect on the interfacial tension between the two fluids.

In addition to the viscosity contrast an interfacial contrast was examined. This was done by adding surfactants to fluids in some experiments to examine their effect on the hydrodynamic properties of droplets. There were three scenarios for the presence of surfactants that were studied in the current work. These were:

Surfactant in droplets above CMC: This was done by adding Tween 20 ($C_{58}H_{114}O_{26}$) to the water phase with 2% or 0.2% w/w according to the fluid.

Surfactant in droplets below CMC: This was done by adding Tween 20 to the water phase with 0.0004% w/w.

Surfactant in the continuous above CMC: This was done by adding Span 80 ($C_{24}H_{44}O_6$) to hexadecane phase with 1% w/w.

The most important property that was examined in the current work was the interfacial tension between the two fluids of each experiment. The interfacial tension between the fluids were measured with a tensiometer that uses a Wilhelmy plate approach with a platinum plate of ($9 \times 12mm^2$). The properties of the fluids are presented in Table 3.3.

Table 3.3: Physical properties of fluids that were used in the droplet transport project.

	Density	Viscosity	Interfacial tension γ mN/m	
Fluid	g/ml	mPa.s	Hexadecane	Hexadecane + Span 80
Fluid 1	0.998	1.02	27.1	1.94
Fluid 2			5.57	-
Fluid 3	1.115	3.3	27.75	-
Fluid 4			3.1	-
Fluid 5			17.49	-

Note: The fluid combinations are as follows: Fluid 1: Water & Dye (10% V/V), Fluid 2: Water & Dye (10% V/V) and 0.2 % Tween 20, Fluid 3: Water, Glycerol 37.2% w/w & Dye (10% V/V), Fluid 4: Water, Glycerol 37.2% w/w & Dye (10% V/V) 2% Tween 20, and Fluid 5: Water, Glycerol 37.2% w/w & Dye (10% V/V) 0.0004 % Tween 20.

3.2.3 Miscellaneous Fluids and Solvents

Various chemical solvents were used in different steps of channel cleaning. These solvents include: wash acetone, isopropanol, methanol, and ethanol. All these chemical were bought from the Chemical Store at the University of Waterloo. MEK (Methyl Ethyl Ketone) was used as a solvent for Polycarbonate to aid with bonding polycarbonate to a substrate.

Surfactants were used throughout different experiments under certain conditions to alter the interfacial tension between the fluids. These were: SDS, Tween 20, and Span 80. The addition of a surfactant to a certain phase is based on its solubility and applicability to adsorb at the fluid/fluid interface. The surface treatment of PC was based on grafting DDA on the surface of PC. DDA (98 % purity, Sigma Aldrich) was used to graft on the surface. DDA was dissolved in Ethanol with different concentration as will explained later in Chapter 5.

3.3 Experimental Systems

There were two main experimental systems that were used in the current work: the μPIV assembly system, and the system that was used for the droplet transport project. Components of each system are presented next.

3.3.1 μPIV Experimental Assembly

The μPIV system integrated two main setups that were: droplet detection and triggering assembly, and the μPIV system assembly. These two systems were assembled in a way that one system serves as the external actuator, or trigger, for the other system. Details about the main parts of each system are presented next.

3.3.1.1 μPIV System

Section 2.3.2 gave an introduction to the PIV principle and the main components of typical systems. The system used in the current study consists of:

Microscope (Nikon Ti-Eclipse): This is an inverted microscope used for holding the sample, guiding the light from the laser to the sample, and mount the camera that is used to observe the field of view. The microscope has a number of objectives (20X, 40X, and 60X).

Laser (ESI - Nd:YAG): A dual head Nd:YAG laser was used to illuminate the field of view. This laser emits light at a wavelength of *532 nm* with a pulse duration between 10-15 ns [1]. The laser power is 15 mJ. This laser can operate with a Frequency of 15 Hz.

Camera (Hamamatsu C8484-05CP): This is a dual-frame 1.4 Mega Pixel CCD camera (1344×1024 $pixel^2$). Each pixel has a physical size of 6.45×6.45 μm^2. The camera was positioned on one port of the microscope with an F-mount adapter with a magnification of *0.5 X*. The camera can acquire images with a

Frequency of 12.2 Hz. The shortest time between two consecutive image pair is $< 200\ ns$ [140].

MotionPro (IDT Vision) Timing hub: This device is used to synchronize light emission by the Nd:YAG laser and image acquisition by the Hamamatsu CCD camera. The timing hub is able to synchronize 8 channels. The system can be either triggered internally by the computer that it is connected to or by an external trigger according to software that runs the experiment.

Computer and Software: Dynamic Studio (V2.3, Dantec Dynamics) was used to control the timing between the different components of the μPIV system. The important settings in the software are:

- Type of image acquisition (single frame or dual frame).
- Number of images to be acquired.
- Internal or external triggering

Dynamic Studio also serves as the software for the data analysis. Details about the analysis approach will be presented in the results section.

Figure 3.4 presents a photograph of the main components of the μPIV system and the trigger parts.

3.3.1.2 Droplet Detection and μPIV Triggering System

The droplet detection system was based on optical detection with a sensor that detects light and converts it to a voltage. Light from the used light source was guided to the area of interest fiber optics embedded in waveguides, as shown in Figure 3.1 -(b). The components that were used are:

Light source: There were two light sources that were tested: a Helium Neon laser (HeNe, 633 nm) and an infra-red laser IR (780 nm). The two light sources were used in different configurations as will be explained later in Section A. The final trigger assembly used the infra-red laser.

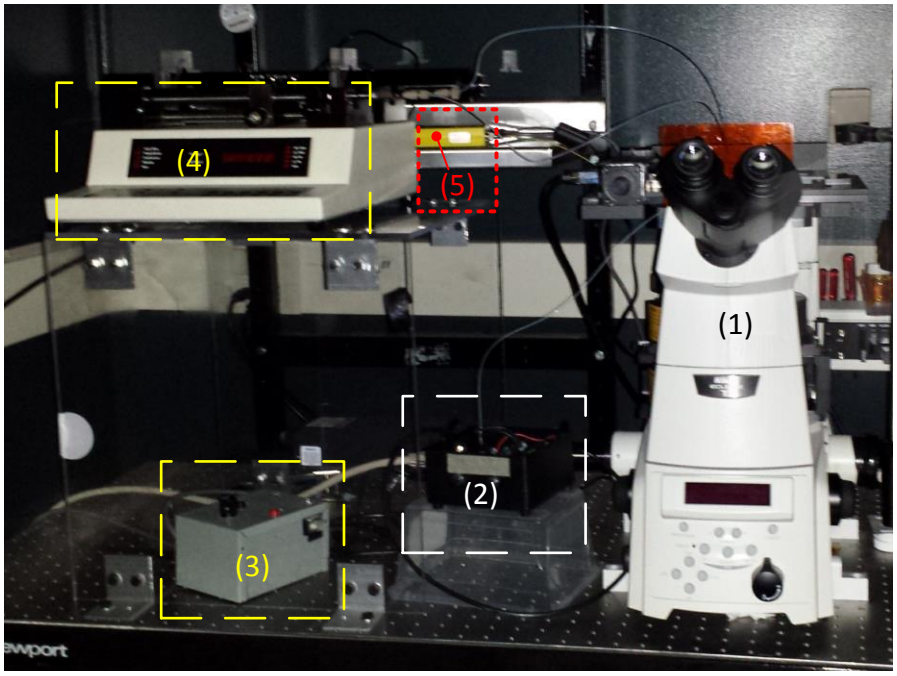

Figure 3.4: The assembled μPIV and triggering systems. Numbered items are as follows: 1- Nikon Ti-Eclipse microscope, 2- Droplet detection setup that contains the PMT, 3- Delay generator, 4- Syringe pump (Harvard apparatus pump 33), and 5- IR laser diode.

Light detector: A photomultiplier tube (PMT- H9656-02. Hamamatsu) was used to detect the droplets.

Light guiding assembly: Single-mode and multi-mode fibers were both used. All fibers were stripped to its cladding diameter $\approx 125\mu m$

Voltage conditioning circuit: This circuit was used to condition the voltage signal from the detector to stay within the signal limitations of the synchronizer.

Delay circuit: The delay circuit functions in a way that it will generate a delay on the signal that is supplied by the delay circuit source.

The assembled microchannel embedded with the fiber optics are shown in Figure 3.5. Optimization of the μPIV trigger approach and setup went through multiple testing stages. The details of the optimization are presented in Appendix A.

3.3.2 Droplet Transport and Resistance Measurement System

Studies of the hydrodynamics of droplet transport in microchannels aimed to examine hydrodynamic resistance of droplets in microchannels, droplet speed, and relative speed to the continuous flow average speed (slip factor of droplets). The measurement approach will be presented a later chapter. The two basic functions of the droplet transport experimental system are: recording droplet motion, and measuring flow conditions. Thus, the experimental system should include: pressure system, flow measurement system, and droplet observation and image recording systems.

The experimental setup consisted of a Nikon Ti-E Eclipse microscope equipped with multiple microscope objectives (4X, 10X, 20X). Bright field microscopy was used in the experiments. Image acquisition was done with a high speed camera with a CMOS sensor (Phantom 210, Vision research). The fluids were supplied with a pressure control system (Fluigent, MFCS system). The flow rate was measured with a high precision flow sensor SLG1430-480 (Sensirion). This flow sensor was pre-calibrated to measure water flow rate. However, other solutions can be used but

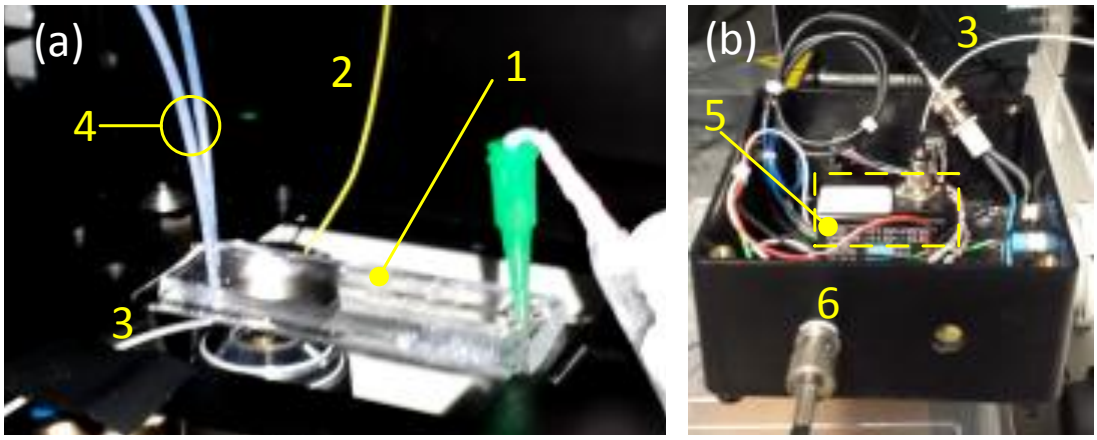

Figure 3.5: Photographs of the PDMS microchannel used in the μPIV study and the assembled droplet detection system. Figure (a) The PDMS chip used in a μPIV experiment with the fluid connections and the inserted fibers, and (b)- The droplet detection sensor and its circuit. The numbered items are as follows: 1- PDMS chip, 2- Single-mode fiber from the laser source, 3- multi-mode fiber sensing light from AOI and transferring it to the light sensor, 4- Teflon tubing used to pump fluids, 5- PMT, and 6- BNC that outputs a voltage to either the synchronizer or the signal delay circuit depending on the triggering approach.

the signal from the flow sensor should be calibrated to account for the different fluid properties. Calibration of the flow sensor for hexadecane was done with a high precision syringe pump (Harvard Apparatus Pump 33, accuracy ±0.35%) and Gastight glass syringe (Hamilton Company 2.5 ml). Figure 3.6 presents the experimental assembly that was used in the current work.

The connections between the pressure system well assembly (see Figure 3.6) and the microfluidic chip was done with 1/16" Teflon tubing (McMaster-Carr) with an inner diameter of 1/32". The connections between the tubing and the reservoir ports of the PC microchannel were done with high pressure Upchurch connectors F-300 or F-333 (IDEX Health & Science).

3.3.3 Miscellaneous Experimental Systems

Other experimental systems were used for measurement purposes throughout this work. Viscosities of fluids were measured with a Brookfield rheometer (Dv-iii ultra, Brookfield) equipped with a coned spindle (cpe 40). Interfacial tensions were measured with a surface tensiometer that uses a Wilhelmy plate approach to measure interfacial tensions between fluids.

Surface treatment of PC with DDA used a syringe pump (Pump 33, Harvard apparatus). Gastight syringes (1 ml and 2.5 ml, Hamilton syringe) were used to pump the fluids with the syringe pump. The temperature was kept constant either by a hot plate or by temperature controlled ultraviolet incubator (SI-905, UVP/Analytika Jena AG).

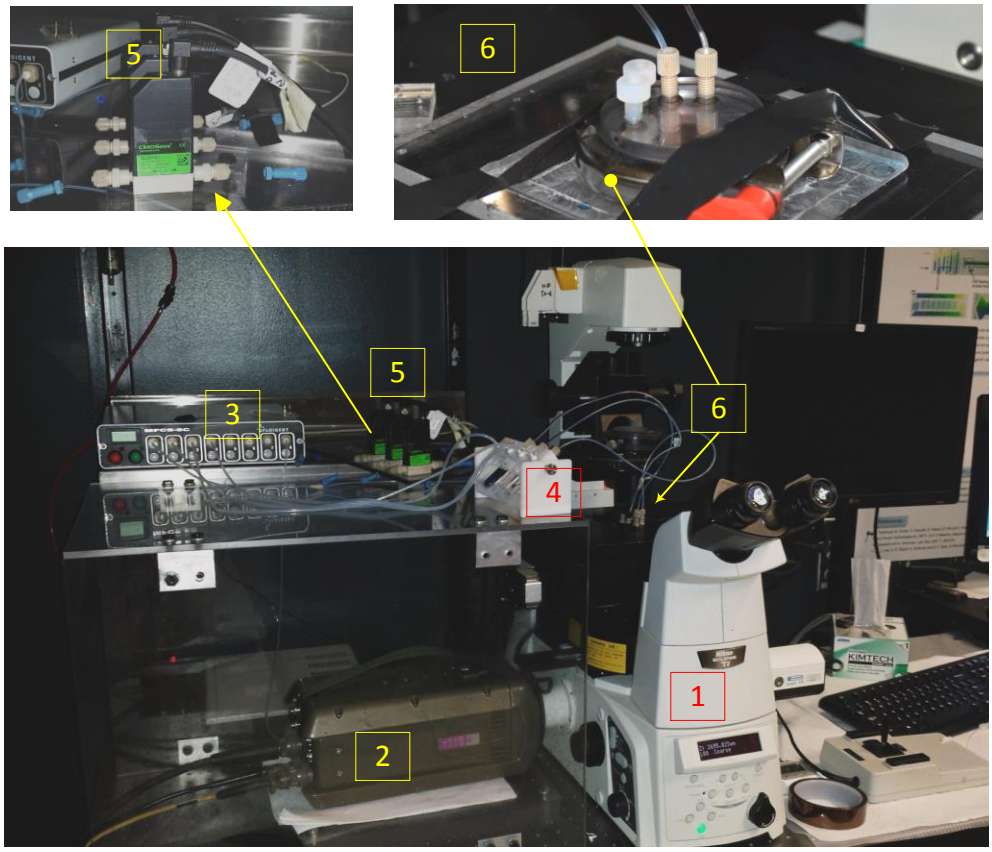

Figure 3.6: A photograph of the experimental setup used in the study of droplet transport and resistance measurements in PC microchannels. The main components of the setup are numbered as follows: 1- Microscope Nikon Ti-Eclipse, 2- Phantom 710 (High speed camera), 3- Fluigent pressure control system, 4- Fluid reservoirs, 5- Sensirion (SLG1430-480) flow sensor, and 6- PC microchannel assembly. Items 5 and 6 were enlarged for a better view.

Chapter 4

Quantitative Studies of Droplet Generation in the Squeezing, Transition, and Dripping Regimes with a μPIV System

In this chapter quantitative velocity field experimental studies of droplet generation in a T-junction microchannel design will be presented. The studies examined the squeezing, transition, and dripping droplet generation regimes and aimed to find the differences between the regimes from a quantitative velocity field perspective. The studies utilized a μPIV approach with phase locking the droplet position with droplets detection approach. For each examined droplet generation regime two types of dispersed phases were used: without a surfactant and with a surfactant above CMC. The Ca identifying the generation regime was kept constant for the two types of fluid combinations. The studies focused on the end of filling and start of pinch-off stages at different planes for each studied flow condition. Results indicate that there are similarities between the flow patterns in dispersed phase during the generation of the liquid segment when Ca was matched [1].

[1]This work is accepted for presentation at the *17th International Symposium on Application of Laser Techniques to Fluid Mechanics, Lisbon, Portugal, July 07 − 10, 2014* [141]

4.1 Introduction

The process of droplet generation in T-junction rectangular microchannels has been studied with numerous approaches that examined the evolution of the dispersed phase interface during droplet generation and the final volume of droplets [39, 28, 34, 38, 64]. Most of the experimental droplet studies are performed with microscopy based techniques to examine the effects of changing the flow conditions, geometrical, and fluids properties on the generation process. Quantitative velocity field studies have been done to examine the velocity patterns inside the continuous phase [29, 116], the dispersed phase [142], or both phases [143, 144]. The studies reported in the literature are limited to low Ca where most of the reported studies focused on the squeezing regime of droplet generation due to hardware limitations. For example, Oishi *et al.* [145] used confocal microscopy with μPIV and the shortest exposure was 1005 μs leading to a Δt between two consecutive frames to be 2020 μs. This time difference is large time and limits the speed of image acquisition and the speed of flow that could be measured. This limitation can be traced back to the camera sensor type where they used a high speed CMOS camera that requires longer exposures and less sensitive compared to typical dual frame CCD cameras used in PIV studies [146].

Even with dual frame intensified CCD cameras that could record Δt up to $\approx \mu s$ ranges between successive images there is a challenge in phase locking the droplet stage with an external droplet detection approach. The importance of phase locking arises since in order to average the PIV results at least 100 images of identical droplets must be acquired. An example of a phase locking system was presented by Van Steijn *et al.* [29] that was based on optical detection of bubbles in the microchannel. Van Steijn *et al.* [29] used an LED as the light source and focused the light on a location downstream of the T-junction bubble generator. Detection was done with a photodiode. The signal recorded by the photodiode was affected by the presence or absence of bubbles since there is a large refractive index mismatch between liquid and gas in the channel.

Adopting the triggering approach that was presented by Van Steijn *et al.* [29] is challenging for droplet detection in microchannels for two reasons. First the refractive

index mismatch that is needed to use photodiodes as droplet detectors in liquid/liquid condition is not appropriate since the signal magnitude is low compared to gas/liquid condition. Secondly, special optics will be needed to focus the external light from the light source, ie LED, on a spot. This process is difficult and challenging to perform in microchannels. For those reasons an optical detection approach that utilizes embedded fiber optics is a better option. A droplet detection system using the principle of embedded fiber was reported by Guo *et al.* [147]. Hence this approach was used to detect droplets during the generation process and trigger the μPIV system. Details about the optimization process for the optical detection approach are presented in Appendix A.

With the developed optical detection system that allowed for phase locking droplets μPIV studies of droplet generation in a T-junction microchannel operating in the squeezing, transition, and dropping regimes were performed. The experimental work focused on examining the velocity patterns at different planes of the droplet stages at the examined regimes to quantitatively find the differences in the velocity patterns between those regimes. Details about the experimental methodology and results are presented next.

4.2 Experimental Setups and Methodology

There were two main experimental systems that were used in the current study: droplet detection and triggering assembly, and the μPIV system assembly. These two systems were assembled in a way that one system serves as the external trigger for the other system. Details about both systems components were presented in Section 3.3.1. Figure 4.1 presents a schematic of the main components both the trigger system and the μPIV system with an illustration of the path of the signal transferred from the trigger system to the μPIV components.

The microchannel network was fabricated from PDMS according to the procedure covered in Section 3.1.1. Silicone oil was used as the continuous phase and a water-glycerol mixture was used as the dispersed phase. The water-glycerol had the same refractive index as the oil to avoid refractive index mismatch issues that may affect

the images acquired by the μPIV camera [108, 110]. Properties of the fluids used in the studies are shown in Table 3.2.

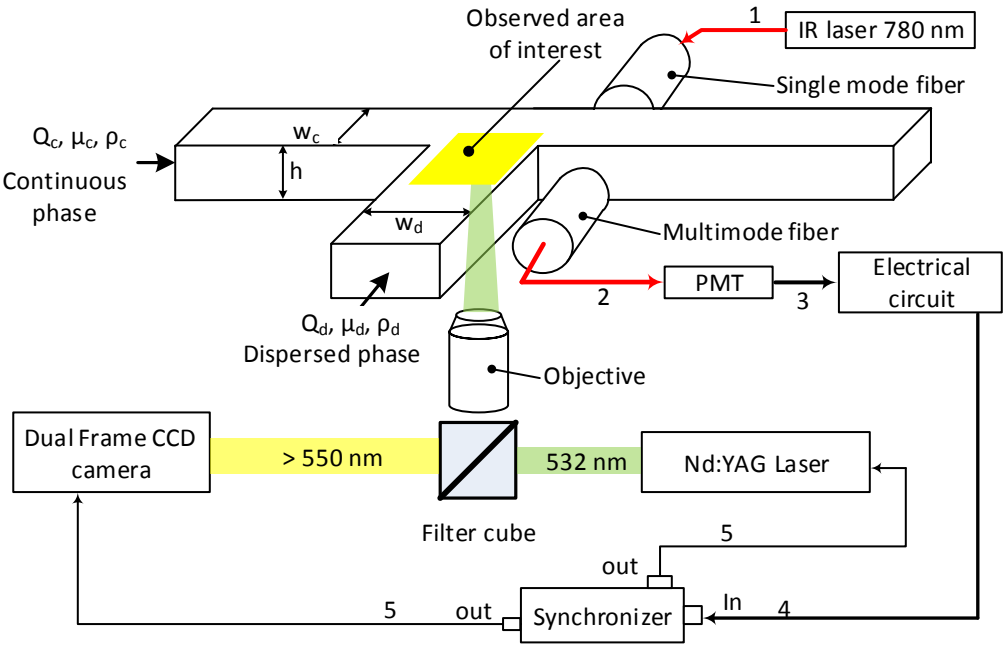

Figure 4.1: A schematic illustration of the main components of the trigger circuit assembled with the μPIV system. The figure illustrates the path of the signal from the trigger setup to the μPIV components.

Fluid pumping in all experiments was performed with a high precision syringe pump (Pump 33, Harvard Apparatus). An experiment starts with pumping silicone oil in the microchannel network for at least 30 minutes. This priming step assures proper wetting of silicone oil with the PDMS microchannel before introducing the dispersed phase. Afterwards, the water-glycerol mixture containing 1 μm fluorescent particles was introduced via the side channel of the T-junction (see Figure 3.1). In all experiments the flow rate of the dispersed phase (water-glycerol) was 25% of the

silicone oil flow rate. This ratio was chosen to create small droplets that can be observed in the field of view of the camera. Table 4.1 presents the experimental flow conditions that were studied in this work with the corresponding flow properties.

Table 4.1: The different droplet generation regimes that were studied and their corresponding flow rate of the continuous flow for each fluid combination. The expected average velocity in the main microchannel u_m is also presented for each flow rate.

Droplet Generation Regime	Ca	No Surfactant		With Surfactant (SDS)	
		Flow rate Q_c $(\mu l/min)$	Average Velocity u_m (mm/s)	Flow rate Q_c $(\mu l/min)$	Average velocity u_m (mm/s)
Squeezing	0.001	5.74	3.235	2.09	1.178
Transition	0.00275	-	-	5.74	3.235
	0.005	28.73	16.17	10.44	5.88
Dripping	0.02	114.92	64.71	41.8	23.53

The practical issues affecting droplet generation in practical systems were discussed in Section 2.2.1. Droplet generation in T-junction microchannels is sensitive to the ratios of the hydrodynamic resistance of the microchannel networks (dispersed phase, continuous phase, and downstream channel sections) [58, 59]. In a typical system the generation process needs some time to produce a uniform droplet size especially with continuous fluid supply systems. An examination of the time needed to stabilize droplet generation using Pump 33 (Harvard Apparatus) was done to identify the proper operation conditions for the μPIV experiments. This examination was done by generating droplets and measuring the droplet area after the T-junction and recording the area change with time. A typical outcome for the variation of droplet area with time for a certain syringe pump flow setting is presented in Figure 4.2.

From Figure 4.2 it was observed that there are two types of droplet area variation: long term area variation, and short term area variation. The long term area variation was the variation of droplets area after the initial setting of the flow rates. This

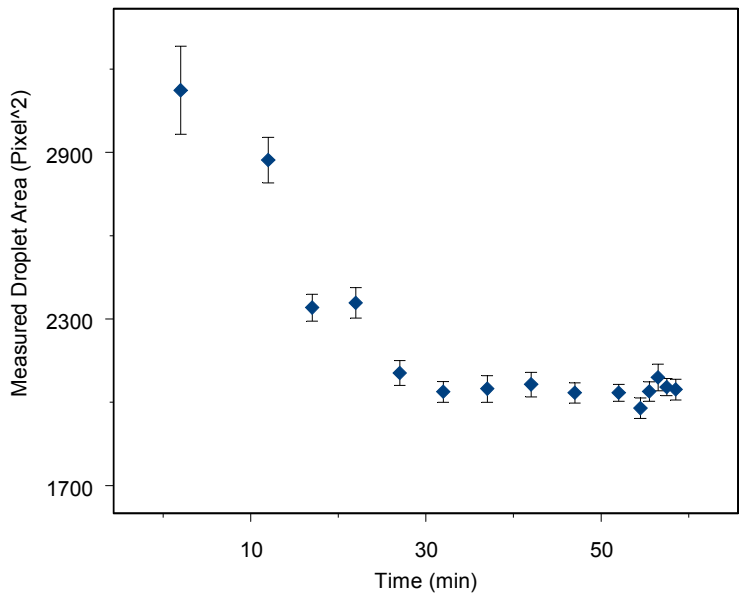

Figure 4.2: Droplet area variation with time while using Pump 33 as the fluids source. The error bars indicate the standard deviation in the measured droplet area.

variation was examined by finding the average droplet area change for a long time duration (minutes). The second type of droplet area variation is the short term variation. This variation was the changes of generated droplet area for a short duration of time (seconds to 1 min). This variation is the standard deviation of the generated droplets area. It is clear from Figure 4.2 that during the first 30 min the droplet area has large variation for long and short term variations. This pattern was clearly observed from the large standard deviations for each point and the overall change in average area. After 30 min droplet variation was small for both long term and short term variations. Hence, the syringe pump needed 30 min to stabilize the droplet generation size.

During the waiting period for the droplet generation stabilization adjustments were made to the trigger circuit assembly to assure droplet sensing. The two parameters of the trigger circuit that were adjusted were sensitivity of the PMT and laser power ($IR\ 780\ nm$). The signal from the trigger circuit was examined with an Oscilloscope (Techtronix) to assure droplet detection. Details about the operation conditions and signal recording of the droplet detection and μPIV trigger circuit are presented in Section A.

All experiments were performed with a 20X (CFI Plan Fluor ELWD, Nikon). The CCD camera C8484-05CP was mounted to a 0.5X adapter. The resulted depth of correlation for this assembly was $\delta_{corr} = 20.24\ \mu m$ [106]. After assuring that droplet generation at the T-junction reached steady condition and phase locking was successful the measurable planes of the channel were assessed. This assessment was done by locating the lowest and highest channel planes that showed a presence of particles. The measurement planes were set and the channel was divided to at least 7 planes of measurements to have a three dimensional observation of the velocity field inside the droplet [2]. Images were acquired with the camera for each measurement plane. The time difference (Δt) between two successive images was set according to the experiment and it varied from 20 - 700 μs. Two phases for droplet generation were studied: filling and start of pinch-off. Around 200 images were acquired at each

[2]Accurate three dimensional examination of the field of view can done with confocal microscopy [118, 144].

droplet plane for a certain stage.

4.2.1 PIV Analysis of Images

The acquired images were analyzed with an adaptive correlation with Dynamic Studio (v2.3, Dantec Dynamics). A 32×32 pixel interrogation area was used. A peak validation scheme with peak-to-peak = 1.35 was applied to the results from the adaptive correlation. Afterwards, a coherence filter with a width of 31 pixels was applied to the peak validated results. The final step of analysis was performing statistical averaging of the filtered results. A typical image recorded for an experimental set with samples of the analysis steps are shown in Figure 4.3. This experiment was for a plane located at $z = 60\ \mu m$ from the bottom channel wall for a droplet prior to pinch-off for a water-glycerol mixture without SDS. This set was for a transition regime, as presented in Table 4.1.

The first image shown in Figure 4.3 -(a) presents an actual image acquired in a μPIV experiment. The flow tracking particles are identified as the small dots with a bight intensity. This image was analyzed with its pair acquired at Δt with an adaptive correlation process. Results from the adaptive correlation Figure 4.3 -(b) showed velocity vectors that do not correspond to the anticipated flow direction. For that reason extra processing was done to filter the outliers. Figure 4.3 -(c) presents the result after applying a peak validation with 1.35 peak-to-peak. Most of the outliers were rejected since they did not meet the peak-to-peak criterion. Rejected peaks are plotted with a red color in Figure 4.3. However, some outliers were still present. These were removed with a coherence filter that was applied. From Figure 4.3 it is clear that the analysis procedure that was performed was sufficient in eliminating outliers associated with cross-correlation of two digital images.

The above mentioned steps were performed for all recorded images for each examined set. The final step was to perform statistical averaging of all valid vector fields. The outcome of a μPIV experiment was a velocity vector field of droplets at a certain stage. This velocity field is quantitative since it gives the velocity of small regions that were defined by the interrogation area (the chosen interrogation area

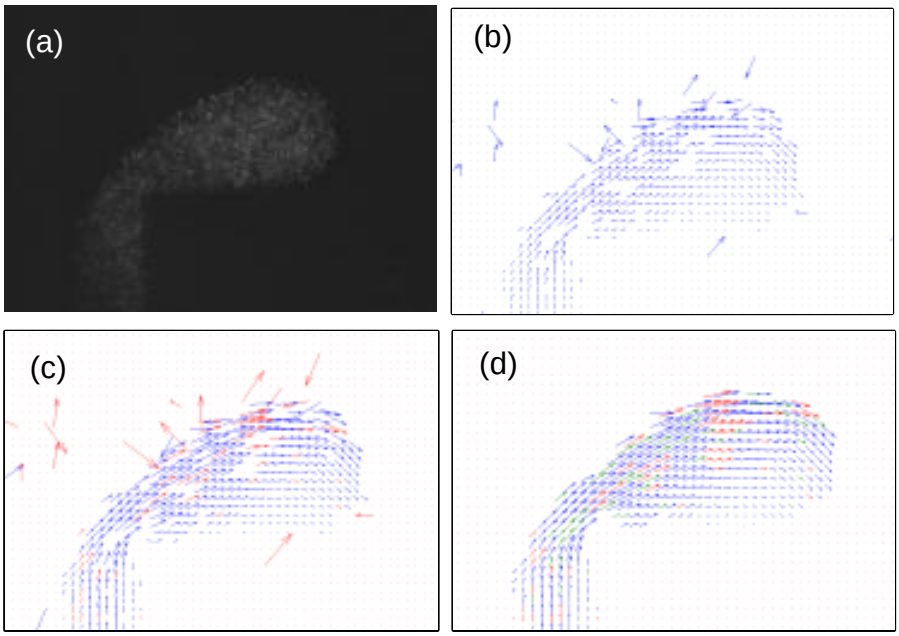

Figure 4.3: A typical image recorded in a μPIV experiment and the typical progression of the analysis steps. Figures are as follows: (a) Raw image, (b) Velocity vector plot after adaptive correlation with 32×32 pixel interrogation area, (c) Velocity vector plot after peak validations, and (d) Velocity vector plot after coherence filter.

32×32 pixels). The velocity vector fields as raw data are useful to identify the flow direction and the magnitudes of velocities at different regions.

The absolute magnitude of the velocity can be used to identify the maximum and minimum velocity regions in measured planes. It also can be used for applying a contour on velocity vector plot. The two velocity components were in the x and y direction and the magnitude of the velocity was calculated from the resultant of the two vector components with Equation 4.1.

$$|V| = |\sqrt{u^2 + v^2}| \tag{4.1}$$

where $|V|$ is the positive value of the resultant of the velocity vectors, u is the velocity in the x-direction, v is the velocity component in the y-direction.

4.2.2 Secondary Analysis of the Velocity Profile

The velocity vector map that was found from the μPIV experiments represents a profile of the velocity field that occurs in the dispersed phase (the droplet phase). These velocity vector fields are a quantitative measurement of the flow. With extra post processing secondary flow field patterns can be found which can identify critical regions in the flow field.

Streamlines Streamlines are defined as the lines that are always tangent to the velocity component. These lines can identify the direction of the flow of the fluid parcels inside the found flow field and if the velocity field speeds up or slows at some regions. For a two dimensional velocity field the streamlines can be found by integrating Equation 4.2 [148]:

$$\frac{dy}{dx} = \frac{u}{v} \tag{4.2}$$

The streamlines were plotted for some velocity vector plots when needed to illustrate general changes in flow. The streamlines plots were limited to planes that were expected to be dominated by a two dimensional flow condition.

Velocity Gradient Another secondary flow property that could be estimated from the velocity vector plot is the velocity gradient. This property can be used to estimate the shear force that acts on the interface between the two fluids. For a two dimensional Newtonian flow with a known velocity field the velocity gradient can be calculated from:

$$\frac{\partial V}{\partial X_i} = \left(\frac{\partial u}{\partial y} + \frac{\partial v}{\partial x} \right) \tag{4.3}$$

where $\frac{\partial V}{\partial X_i}$ is the velocity gradient, $\frac{\partial u}{\partial y}$ is velocity gradient of the x-component in the y-direction, and $\frac{\partial v}{\partial x}$ is the velocity gradient of the y-component in the x-direction. The velocity gradient indicates the regions in the flow that endures the major velocity changes. The shear stress of the flow can be calculated by multiplying the velocity gradient with the viscosity of the fluid.

4.3 Experimental Results

One of the aims of the velocity studies is to examine the differences for the droplet generation between different regimes. Proper representation of the results is important in order to reach to accurate conclusions. The velocity field results for one plane, similar to the one presented in Figure 4.3, are compiled with the results of the other planes for the same droplet position into a 3D velocity field. A typical 3D velocity vector plots for one set of experimental condition is presented in Figure 4.4.

The results presented in Figure 4.4 were for the filling stage for water-glycerol with SDS. It is clear from the figure that the velocity plots are symmetric along the height of the channel (*z-axis*). It is observed that at different planes the velocity vector plots differ in their magnitudes and location of the maximum velocity regions. This difference is due to the nature of confinement and the flow nature of the continuous and dispersed phases.

Although not exact but the three dimensional shape of the droplet could be identified from the velocity plot of Figure 4.4. The increase in the droplet projected area away from the top and bottom walls with the maximum projected area located

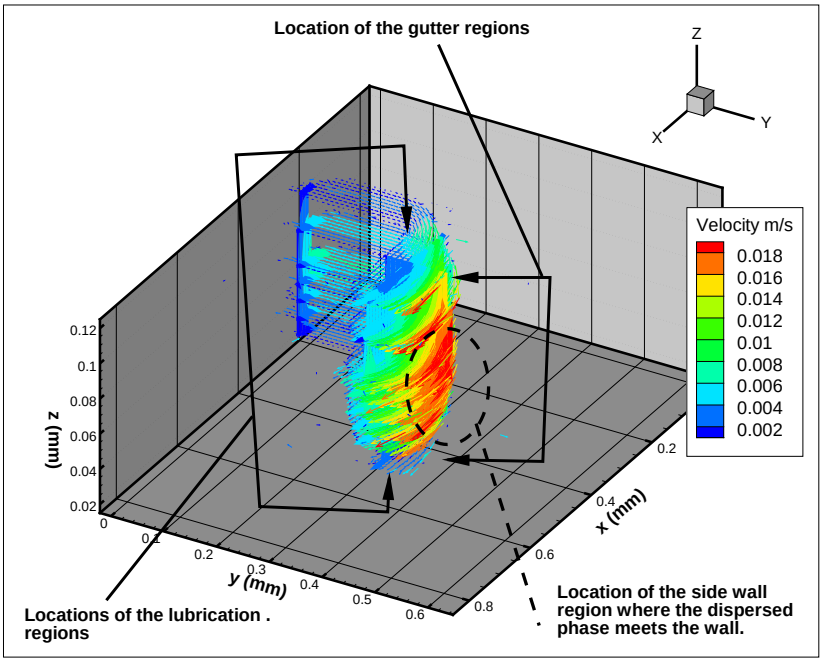

Figure 4.4: A three dimensional velocity vector plot for an experiment of droplet generation in the transition regime ($Ca = 0.005$) for water-glycerol with SDS. The locations of the important regions of the encapsulation regions of the droplet are identified in the plot.

at the middle plane is evidence of the three dimensional shape of a droplet and the success of the μPIV system in finding it. The main regions that surround a droplet in a T-junction generator are: the lubrication films at the top, bottom and side walls, and the gutter regions at the corners of the top and bottom walls. These regions are illustrated in Figure 4.4.

It was seen in Figure 4.4 the flow patterns along the planes are symmetric above and below the middle plane. For that reason it is acceptable to take one half of the three dimensional velocity plots as a representation of the three dimensional flow around a droplet, as will be done in later discussions. There are other regions that must be identified for the droplet phase to simplify the upcoming discussions. These regions are: the T-junction entrance, the back end droplet (BOD), and the leading edge of the droplet. The back end of the droplet (BOD) is the region from the T-junction entrance up to the side wall of the channel. This region is subjected to the buildup of pressure from the flowing continuous phase. Figure 4.5 presents the regions for the droplet that will be used to discuss the experimental results.

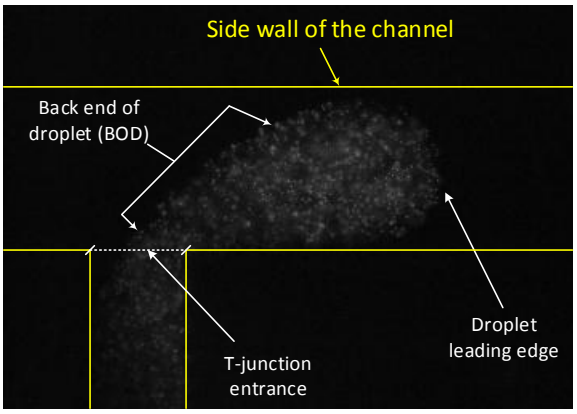

Figure 4.5: A typical image recorded with the camera of the μPIV system of droplet generation in the filling stage. The main regions for the droplet are identified in the figure along with the side walls of the microchannel.

A method that can be used to simplify the discussions about the droplet generation for different regimes is to use non-dimensional numbers. These numbers can

be for the geometrical and flow conditions. The non-dimensional velocity field was found by dividing the measured velocity from the vector plot with the average velocity of the continuous phase for each specific condition (see Table 4.1). The x and y geometrical coordinates in the images were changed to a non-dimensional form by subtracting the location of the first corner of the T-junction and dividing the outcome with the channel width (200 μm). The plane location in the z-axis was changed to a non-dimensional form by dividing the plane location with the channel height (h = 148 μm).

4.3.1 Droplet Generation in the Squeezing Regime

The squeezing regime of droplet generation is identified by having $Ca < 0.002$. This regime was characterized by having the droplet phase filling the channel and blocking it. Then the continuous phase pushes the dispersed phase at the back of the droplet and causes the droplet pinch-off. Experimental and numerical studies reported f that the droplet pinch-off is due to the buildup of pressure on the interface [30, 83]. Hence, the filling stage where plugging of the channel starts is important since immediately after it pressure build up occurs the droplet starts to pinch-off. Typical results from the μPIV experiments for the filling stage for the water-glycerol mixture without SDS are presented in Figure 4.6.

It is clear from Figure 4.6 -(a) that the filling stage during droplet generation is a complex process where the velocity fields differ depending of the location of the studied plane, as was seen before in Figure 4.4. The complexity can be observed by the velocity maps at different heights of the channel. A decomposition of the velocity vector and velocity gradients contour plots for different planes are presented in Figures 4.6 (b), (c), and (d). At different planes the magnitudes and direction of the velocity fields were affected by their location with respect to the confining walls (top, bottom or side walls), the incoming droplet flow, and the continuous phase flow.

For the plane located close to the top wall ($z/h = 0.81$) shown in Figure 4.6-(b) the highest velocity is located at the edge of the droplet, or liquid/liquid, interface.

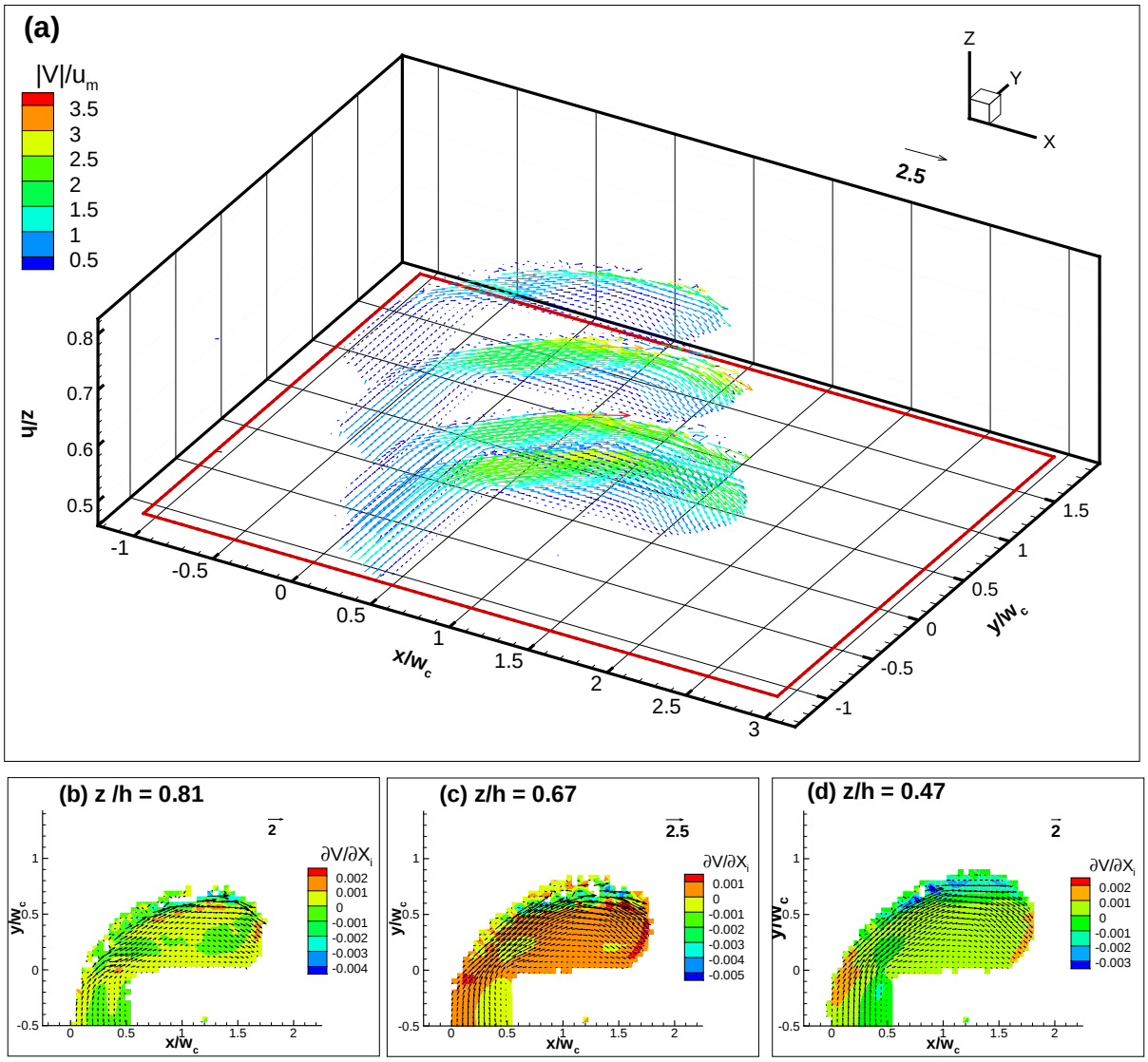

Figure 4.6: The upper planes representing the three dimensional velocity vector plots for the filling stage in the squeezing regime ($Ca = 0.001$) for water-glycerol without SDS. The lower images present the velocity gradients at different planes along with velocity vector plots. Figure (a) The 3D velocity vector plot, (b) The velocity gradient and velocity vector plots at z/h = 0.81, (c) The velocity gradient and velocity vector plots at z/h = 0.67 , and (d) The velocity gradient and velocity vector plots at z/h = 0.47.

This fluid interface was in contact with the gutter region where the continuous phase has the highest flow rate compared to the other regions of the droplet. The majority of the droplet phase at the highest plane was in contact with the lubrication film that separates the dispersed phase from the top wall. Since this region has a very shallow height the flow within the gap is slower than that of the gutter region (see Figure 2.5, 4.4). An estimation of the velocity gradient at the highest measured plane ($z/h = 0.81$) indicates that the highest velocity gradient occurs at the edge of the liquid/liquid interface close to the gutter region. The variation in the velocity gradient was indicative of the regions of the dispersed phase that are subjected to the highest shear.

The projected area of the droplet increased as the location of plane of measurement was close to the middle plane, as clearly shown in Figure 4.6 -(a). The velocity fields at the lower plane (plane $z/h = 0.47$) exhibited some changes compared to the top plane ($z/h = 0.81$) where the velocities at the edge of the liquid/liquid interface were slower than the bulk velocity coming from the entrance of the T-junction. The reason for this decrease was that region is in contact with the lubrication region of the side wall (see Figure 4.4). From the velocity vector plots across all planes it was observed that the maximum velocity during the filling stage occurred at planes that are subjected to the flow of the gutter regions ($z/h = 0.81$ *and* 0.67). The velocity gradients for the planes closer to the middle plane ($z/h = 0.47$ *and* 0.67) showed similar trends to what was observed in the upper plane ($z/h = 0.81$). High velocity gradients were identified at regions close to the liquid/liquid interface close to the side wall.

Results of the flow patterns during the filling stage shown in Figure 4.6 revealed interesting velocity fields with respect to the location of the planes. Another important phase for droplet generation is the start of pinch-off. Capturing the start of pinch-off for a droplet was achieved by imposing a delay on the signal from the trigger circuit which allowed for acquiring images at the start of pinch-off. The velocity profiles in the dispersed phase during start of pinch-off are presented in Figure 4.7.

The flow patterns shown in Figure 4.7 were for the upper, middle and lower planes of the channel. For the upper and lower planes ($z/h = 0.13$ *and* 0.81) the location

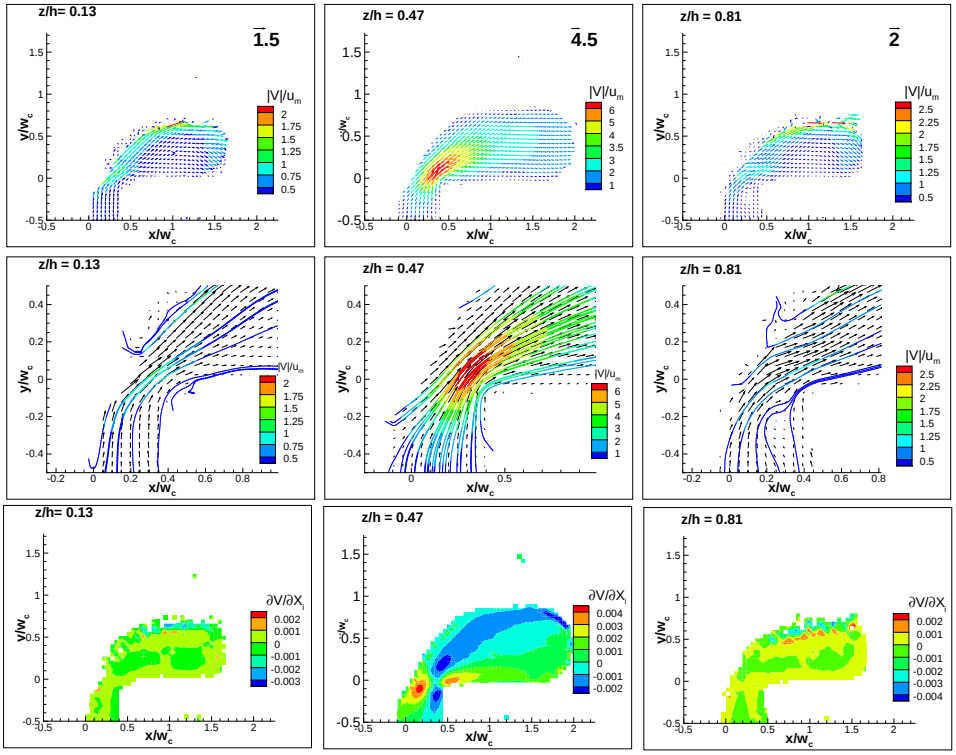

Figure 4.7: The velocity vector and velocity gradient contour plots at different planes during droplet pinch-off in the squeezing regime ($Ca = 0.001$) for water-glycerol without SDS. The upper images present the velocity fields during start of pinch-off at different planes. The middle images show the velocity field close at the corner of the T-junction at the start of pinch-off. The third row of images present the velocity gradient at the start of pinch-off. Information about the location of the planes and the magnitude of the flow properties are listed in each plot.

of the maximum velocity was close to the edge of the liquid interface located at the gutter regions. This was similar to what was observed in the filling stage at the top wall (Figure 4.6).

At the middle plane ($z/h = 0.47$) the region with high velocities was close to the corner of the T-junction. The reason that the velocities were high close to the T-junction was the reduction in the dispersed phase thread that fills the droplet. This reduction reduces the area of the thread and from the conservation of mass the velocity increases its speed compared to the non-squeezed interface of the filling stage. The lowest velocities at the middle plane were located at the regions where the droplet phase was in contact with the side walls of the channel, similar to what was observed during the filling stage.

By examining the velocity vector plots at the corner of the T-junction (second row of Figure 4.7) it was noticed that at the top and bottom planes ($z/h = 0.13$ *and* 0.81) there were more disturbances in the vector fields. These disturbances were indicative that the pinch-off starts at the top and bottom planes and grows towards the middle plane. The velocity vector plot for the middle plane ($z/h = 0.47$) shown in the second row of Figure 4.7 demonstrated a smoother velocity profile close to the corner compared to the top and bottom planes.

The velocity gradient contour plots for the start of the droplet pinch-off stage for the different planes were shown in the third row of Figure 4.7. The patterns and discussions that were presented earlier for the filling stage close to the top channel wall are applicable for the start of droplet pinch-off in planes close to the top and bottom walls ($z/h = 0.13$ *and* 0.81). The main similarity was that the maximum velocity gradient occurred at the liquid/liquid interface adjacent to the gutter regions.

As for the middle plane ($z/h = 0.47$), at the start of pinch-off the velocity gradient patterns differed from what was observed in the filling stage. The velocity gradients showed an increased concentration of gradient close to the T-junction. This change in the velocity gradients indicates that the velocity gradients patterns at the middle plane shifts during droplet pinch-off from the liquid/liquid interface between the droplet and the continuous phase.

Having examined both the filling stage and start of pinch-off for droplet gen-

eration in the squeezing regime for water-glycerol without the SDS surfactant, it's appropriate to present results for the same number Ca for water-glycerol with SDS. The velocity and velocity gradients outcomes from μPIV experiments for the filling stage for water-glycerol with SDS are presented in Figure 4.8.

From the first look at Figure 4.8 it was indicated that the same observations and discussions that were presented earlier for the condition without a surfactant (discussion for Figure 4.6) are still applicable. The velocity gradients and velocity magnitudes had a very close trend to fluid condition without surfactant. This finding indicates that the general velocity patterns in the dispersed phase do not change in the presence of surfactants.

4.3.2 Droplet Generation in the Transition Regime

Droplet generation in the transition regime differs from squeezing regime where both pressure and shear forces play a role in the dispersed phase thread rupture and droplet generation. The transition regime is identified by having a $0.01 > Ca > 0.002$. In the current work experiments were carried for a $Ca = 0.005$ to assure that the droplet generation will be in the transition regime. Experiments were performed for water-glycerol with and without a surfactant for the droplet filling stage and start of pinch-off. Figure 4.9 presents the filing stage of a droplet during the transition regime for water-glycerol with SDS.

The velocity vector plots at different planes in the transition regimes showed interesting patterns. From Figure 4.9- (a) it is identified that at different planes the location of the maximum velocity regions change. For the highest plane ($z/h = 0.81$) the location of the maximum velocity region was at the gutter region. Close to the middle planes ($z/h = 0.47$) the regions with high velocities are located close to the side wall of the channel. This shift in the location of the maximum velocity closer to the middle planes of the channel was different from what was observed in the squeezing regime. This finding is an indication of the high shear that acts on the dispersed phase interface close to the side wall.

The velocity gradient contour plots for the transition regime are shown in Fig-

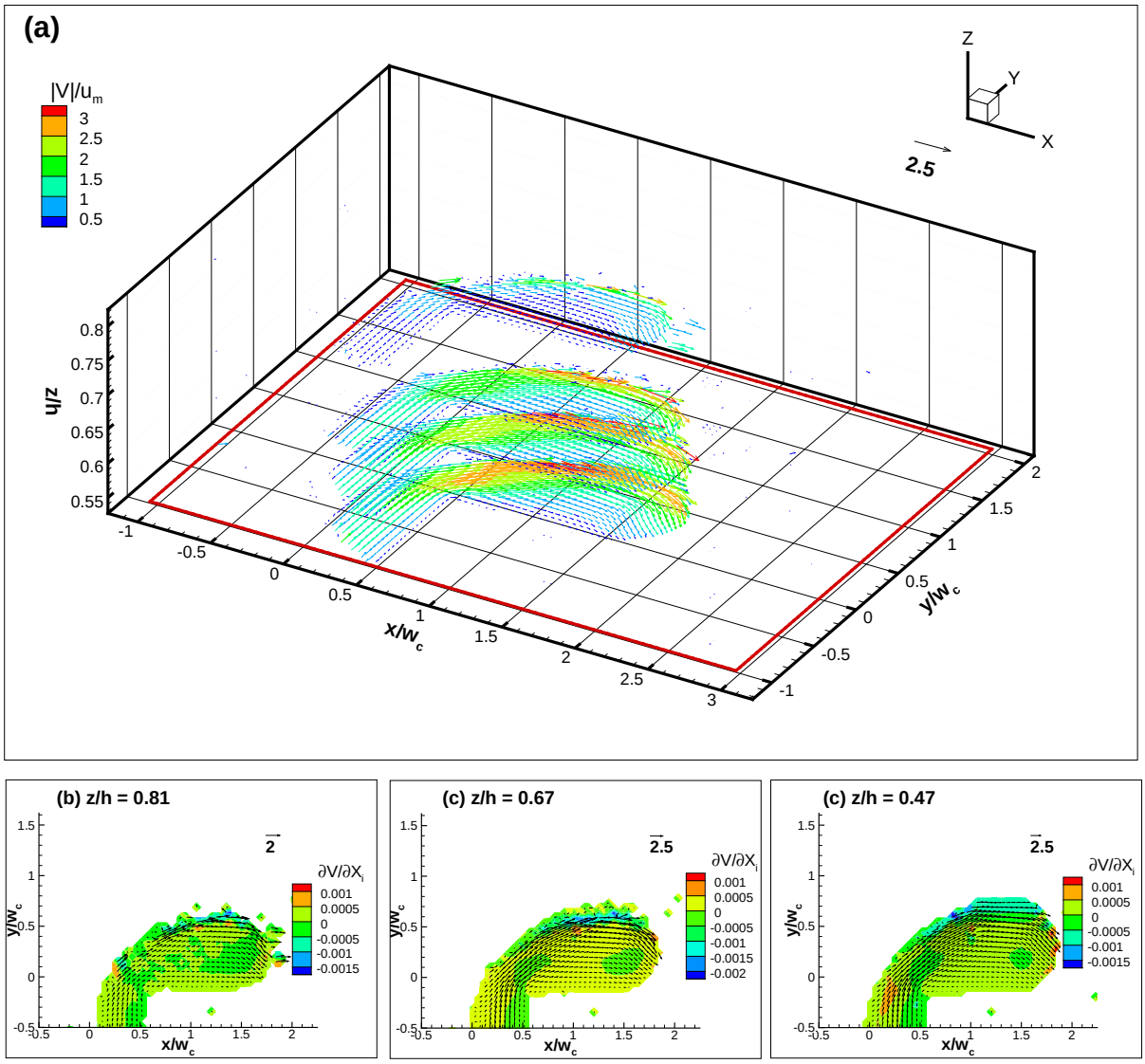

Figure 4.8: The upper planes representing the three dimensional velocity vector plots for the filling stage in the squeezing regime ($Ca = 0.001$) for water-glycerol with SDS. The lower images present the velocity gradients at different planes along with velocity vector plots. Figure (a) The 3D velocity vector plot, (b) The velocity gradient and velocity vector plots at z/h = 0.81, (c) The velocity gradient and velocity vector plots at z/h = 0.67 , and (d) The velocity gradient and velocity vector plots at z/h = 0.47.

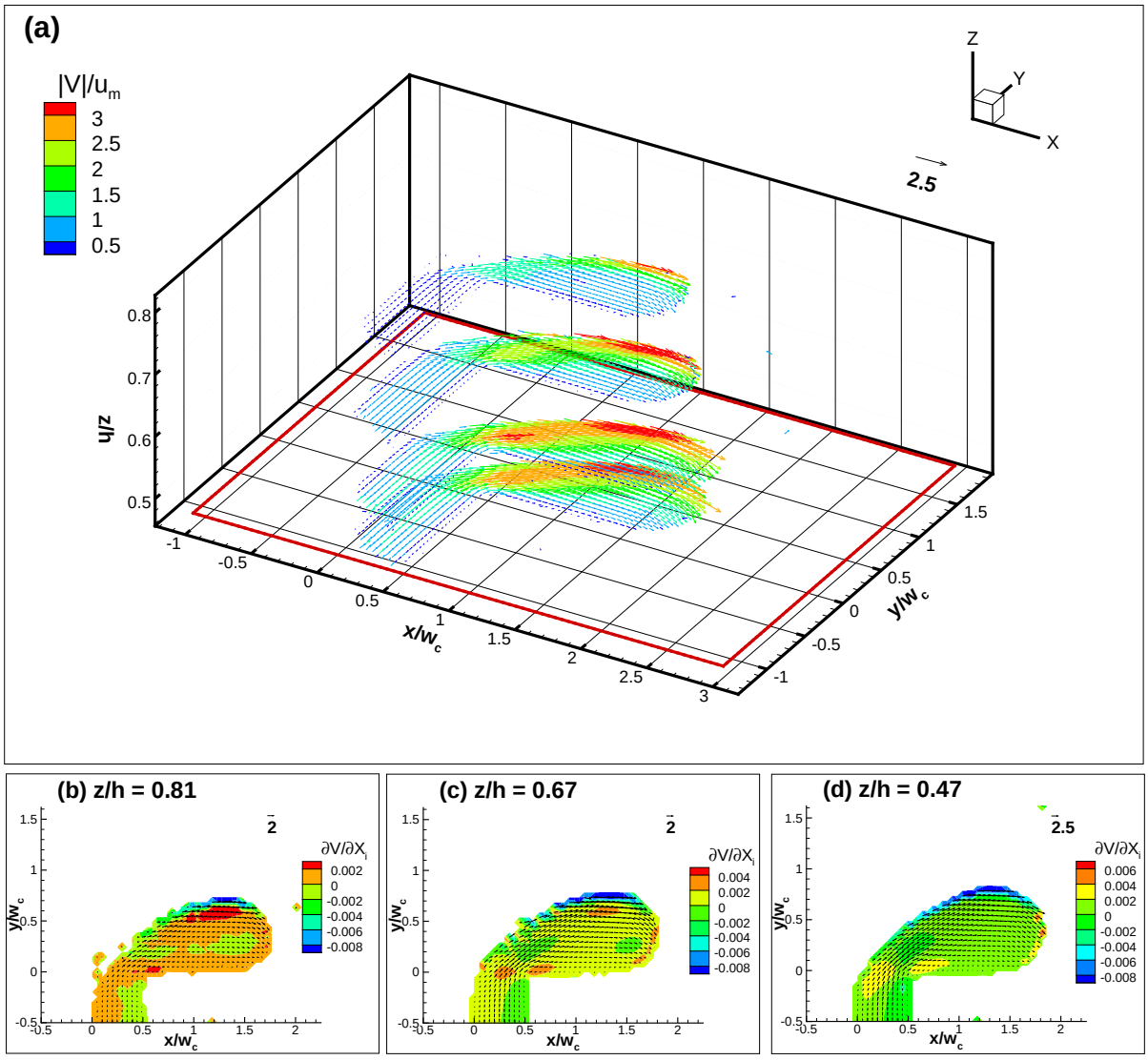

Figure 4.9: The upper planes representing the three dimensional velocity vector plots for the filling stage in the transition regime ($Ca = 0.005$) for water-glycerol with SDS. The lower images present the velocity gradients at different planes along with velocity vector plots. Figure (a) The 3D velocity vector plot, (b) The velocity gradient and velocity vector plots at z/h = 0.81, (c) The velocity gradient and velocity vector plots at z/h = 0.67 , and (d) The velocity gradient and velocity vector plots at z/h = 0.47.

ures 4.9 -(b-d) present interesting patterns. At the top plane ($z/h = 0.81$) the maximum velocity gradient was close to the gutter region, similar to what was observed in the squeezing regime. At planes that are close to the middle plane the gradient was high at the edge of the dispersed phase close to the side wall. The magnitude of the velocity gradient showed that it was continuous and high from the gutter region at the top wall down towards the middle plane. This pattern of continuity in the velocity gradient is proof of the high shear that acts on the interface.

It should be pointed out that the start of droplet pinch-off velocity and velocity gradient plots were examined for the transition regime and showed similar patterns to what were observed at the start of pinch-off in the squeezing regime. Also, the discussions of the presence or absence of surfactant in the squeezing regime are applicable to the transition regime. Hence, those discussions and plots were not included in the current chapter.

4.3.3 Droplet Generation in the Dripping Regime

The dripping regime is the regime that the droplet pinch-off is induced by the shear from the continuous phase flow. The dripping regime that was studied in this work had a $Ca = 0.02$ for both fluid combinations (without or with surfactant). The experiments were very challenging and the most difficult to perform. One reason was that due to the location of droplet detection fibers the droplet shape will be distorted and started to pinch-off, which led to missing the filling stage of droplet generation. This problem was circumvented with the signal delay generator that was mentioned before [3]. The second reason was that droplet pinch-off in the dripping regime is very fast (μs range) and was close to the time needed for the trigger circuit to detect and send a signal to the μPIV system.

The experiments that were done for the dripping regime focused on the filling

[3]The function of the delay generator was to impose a delay of δt that allowed for capturing droplet generation at the required phase. This step was very time consuming for experiments in the dripping regime since it involved changing the time of the delay for several iterations to achieve proper droplet phase locking. Moreover, the delay generator had a jitter of around 20 μs which was in the same order of magnitude of droplet generation time scale.

stage and the start of pinch-off of droplets. The velocity vector and velocity gradient contour plots for the progression of the filling stage up to before pinch-off during the dripping regime for the experiment without SDS are presented in Figure 4.10.

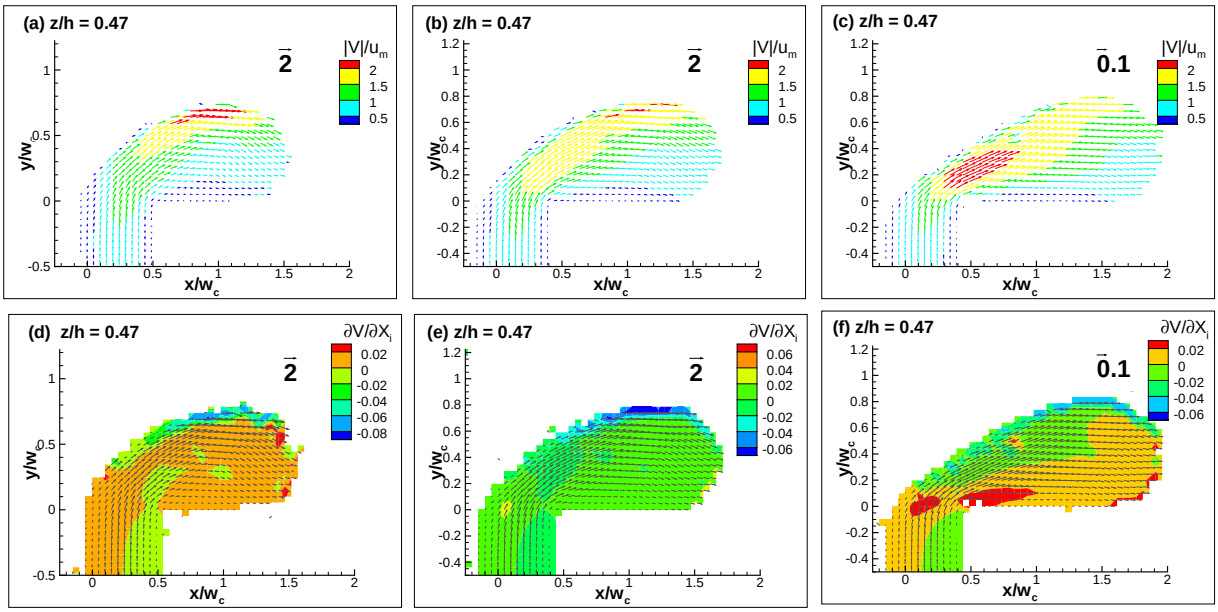

Figure 4.10: The velocity vector and velocity gradient contour plots at the middle plane for different stages of droplet generation in the dripping regime (Ca = 0.02) for water-glycerol without SDS. (a) Velocity vector plot during the filling stage 1, (b) Velocity vector plot during the filling stage 2, (c) Velocity vector plot at the start of interface squeezing, (d) Velocity gradient during filling stage 1, (e) Velocity gradient during filling stage 2, and (f) Velocity gradient contour plot at the start of interface squeezing.

From the velocity vector plots in Figure 4.10- (a), and (b) it is clear that the filling stages of the dripping regime share similarities with velocity vector plots of the transition regime for the same plane (z/h =0.81). The region of the maximum velocity occurred at the liquid/liquid interface that was in the vicinity of the side wall as seen in Figures 4.10 -(a), and (b). As the interface of the dispersed phase started to be squeezed at the T-junction the location of the region with the maximum

velocity shifted towards the entrance of the T-junction, as shown in Figure 4.10 -(c).

The velocity gradients presented in Figure 4.10 -(d), (e), and (f) showed some interesting patterns. First, during the filling stages of the dripping regime (Figures 4.10 -(d), and (e)) the velocity gradients were similar to what was observed in the transition regime. The highest region with velocity gradients were at the edge of the droplet interface to the side wall. This pattern is indicative of the high shear. Figure 4.10 -(e) presented the velocity gradients close at the start of interface squeezing in the dripping regime. The velocity gradient patterns showed that there will be a region with high gradients at the corner of the T-junction when the dispersed phase interface is squeezed.

The droplet pinch-off in the dripping regime differed from what was observed in both the squeezing and transition regimes. The dispersed phase thread pinch-off did not occur at the corner of the T-junction. Instead the dispersed phase thread pinch-off happened downstream of the T-junction. Figure 4.11 presents the velocity and velocity gradient plots for different planes at the start of pinch-off in the dripping regime for water-glycerol with SDS.

It is clear from Figure 4.11 that the velocity vector plots at start of pinch-off for the dripping regime differed from what was observed in other studied regimes. At the planes close to the top wall the droplet phase thread has detected from the supply thread from the T-junction. At those planes the region with the high velocity was at the edge of the liquid interface that is close to the gutter region. At the middle plane the region with the highest velocity was close to the corner of the T-junction. The region with highest velocity regions across the height of the droplet phase was located at the middle plane ($z/h = 0.54$).

The plots at the second row of Figure 4.11 ((a2), (b2) , and (c2)) focus on the region close to the T-junction during the start of droplet pinch-off in the dripping regime. It is observed that the liquid thread pinch-off occurs with the thinning of the thread. Also, the velocity patterns at the trailing of edge of the droplet showed a uniform direction with the flow. This result was different from what was observed in the squeezing and transition regimes where at the planes close to the channel top wall velocity disturbances were observed.

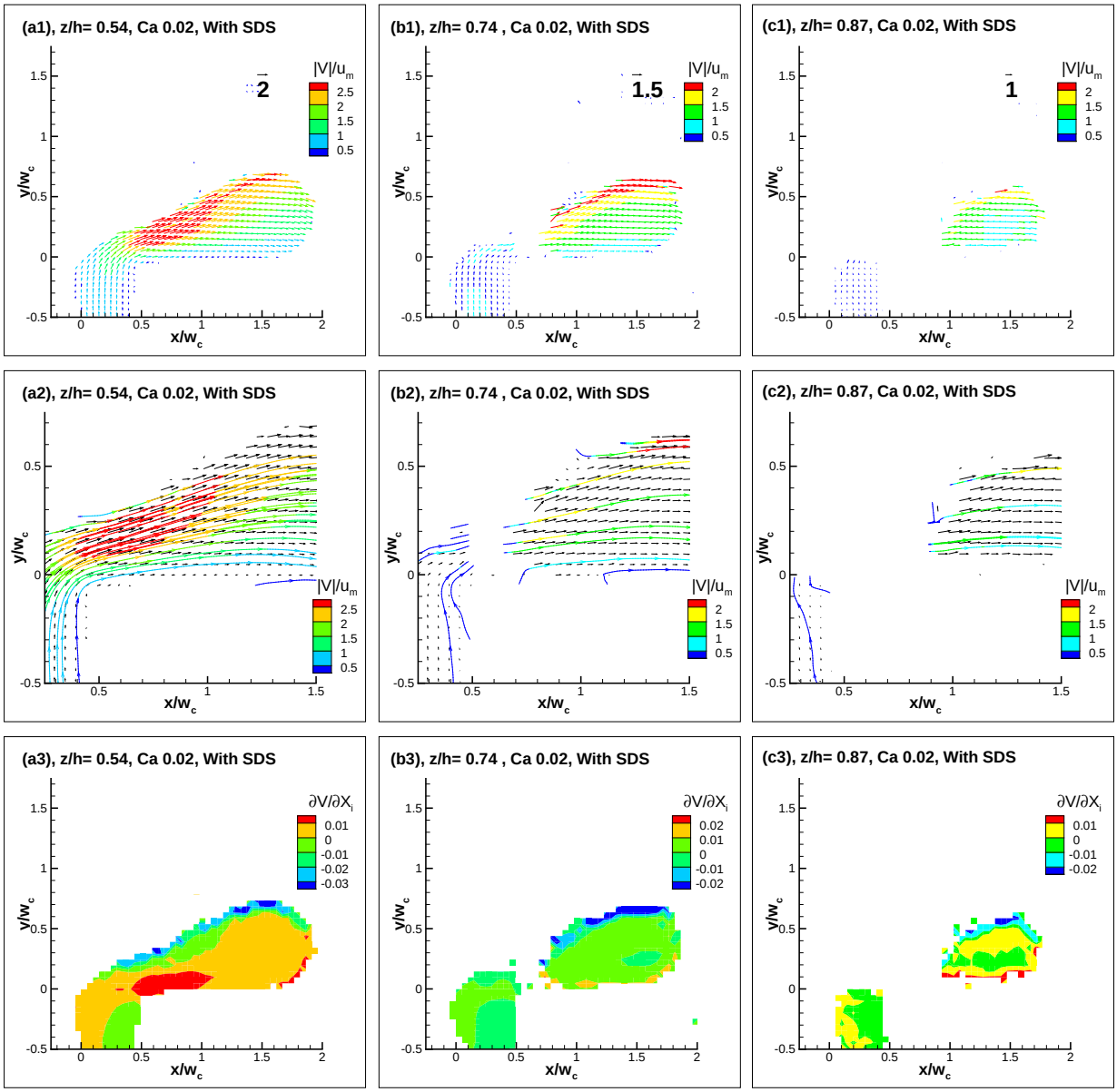

Figure 4.11: The velocity vector and velocity gradient contour plots at different planes across the channel height during the start of droplet pinch-off in the dripping regime ($Ca \approx 0.02$) for water-glycerol with SDS. Information about the location of the plane is indicated in each figure.

The velocity gradients during the droplet pinch-off in the dripping regime are presented in the third row of Figure 4.11 (Figures (a3), (b3) , and (c3)). The velocity gradients were similar to the observed velocity gradient in the transition regime where the region with high gradients were located at the edge of the droplet interface close to the side wall located at $y/w_c = 1$. This region is subjected to a high shear from the continuous phase.

4.3.4 Droplets After Pinch-off

The results presented above focused on examining the differences between the droplet generation regimes for the filling and start of pinch-off stages. It is interesting to examine the velocity vector and velocity gradient contour plots after pinch-off of the droplet. An experiment was done that focused only on the droplet pinch-off stage during the transition regime for water-glycerol without a surfactant. Since the most interesting flow patterns occurred at the middle plane and the planes close to the top and the bottom walls, their results will be presented and discussed in this section. The velocity vector and velocity gradients contour plots at different stages of droplet generation at the middle plane are presented in Figure 4.12.

From Figure 4.12 -(a) it is evident that the stage prior to droplet pinch-off was similar to what was presented before in the squeezing regime where a high velocity region occurred close to the T-junction. The corresponding velocity gradient shown in Figure 4.12 -(d) indicated that high velocity gradients were located at the edge of the dispersed phase interface close to the side wall ($y/w_c = 1$) and at the T-junction.

Immediately after pinch-off the droplet velocity vector plots of the middle plane showed interesting patterns, as presented in Figure 4.12 -(b). The region of the high velocities was located at the trailing edge of the droplet. This was due to the fast movement of the droplet trailing edge interface since it needs to attach to the droplet body and form a curved interface. Thus, the speed of the interface was very high compared to other locations of the droplet. The corresponding velocity gradients indicate that at this phase the velocity gradients vary across the droplet phase shown in Figure 4.12 -(e).

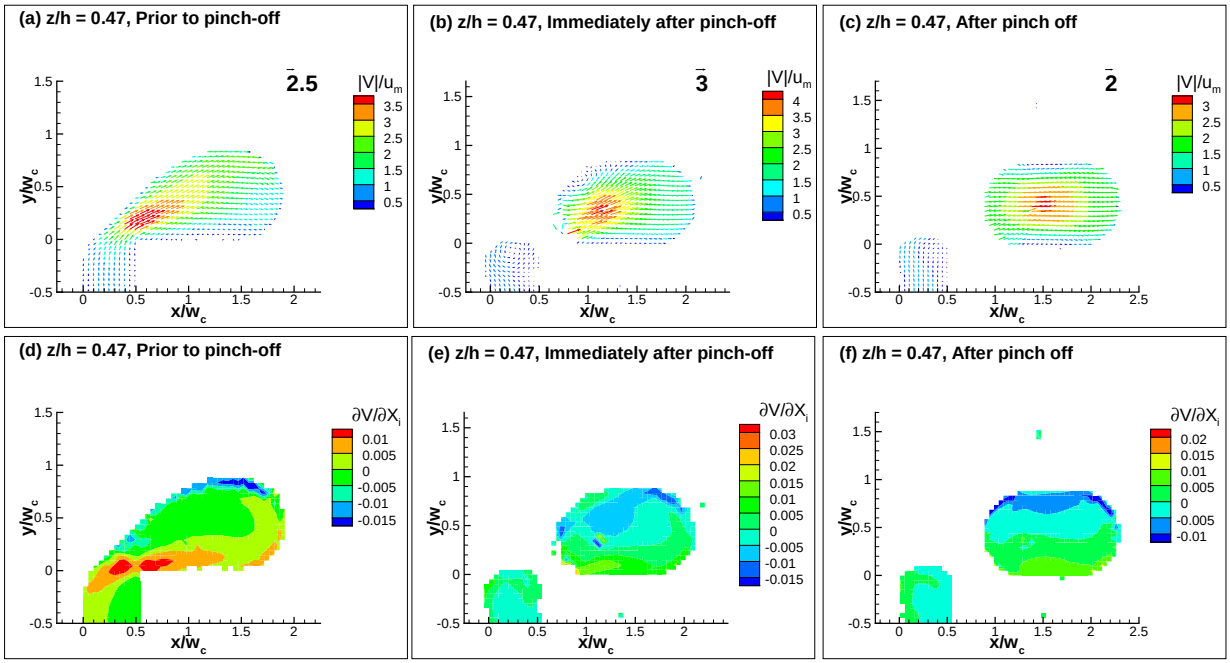

Figure 4.12: Velocity vector and velocity gradient contour plots at different phases for droplet generation in the transition regime ($Ca = 0.005$) for the middle plane $z/h = 0.47$ for an experiment of water-glycerol without SDS. The figures are as follows: (a) Velocity vector plot at start of pinch-off, (b) Velocity vector plot immediately after pinch-off, (c) Velocity vector plot after pinch-off and shape stabilization, (e) Velocity gradient contour plot at start of pinch-off, (e) Velocity gradient contour plot immediately after pinch-off, and (f) Velocity gradient contour plot after pinch-off and shape stabilization.

After pinch-off it was expected that the velocity vector field will be symmetric along the center of the droplet. This condition was proven and is shown in Figure 4.12 -(c). The velocity gradients at the middle plane after droplet pinch-off showed that the velocity gradient is symmetric across the droplet phase as seen in Figure 4.12 -(f). The locations of high gradients were at the curved leading and trailing edge of the droplet interface.

The plots of the middle plane for droplet pinch-off in the transition regime presented in Figure 4.12 showed interesting results. To have further insight on the velocity patterns an examination of the same droplet stages but at the lower plane ($z/h = 0.13$) are presented in Figure 4.13.

From Figure 4.13 it is observed that some of the arguments presented for the filling stage at the middle plane (results of Figure 4.12) may not be applicable. The velocity vector profiles show that the highest regions for different stages occur at different places depending on the phase. In the start of pinch-off (Figure 4.13-(a)) a high velocity region occurred at the edge of the liquid/liquid interface and the corner of the T-junction. Immediately after pinch-off (Figure 4.13-(b)) the maximum velocity occurred at the liquid interface that was moving to reshape the droplet, similar to Figure 4.12 -(b). After pinch-off and the droplet recovered to a symmetric shape there were two locations for the maximum velocity: the leading and trailing edge of the droplet. This finding was clearly observed in Figure 4.13 -(c). This result differed from what was shown in the middle plane (Figure 4.12-(c)).

The velocity gradients shown in Figure 4.13-(d) present similar patterns to the velocity gradients observed in the middle plane (Figure 4.12 -(d)). There were two regions of high velocity gradients one close to the corner of the T-junction and the other at the liquid interface close to the side wall. Immediately after pinch-off the velocity gradients were complex. After the droplet recovers to the shape that minimizes its surface tension, with curved leading and trailing edges, there were high velocity gradients located at the leading and trailing edge of the curved interface, as seen in Figure 4.13 -(f).

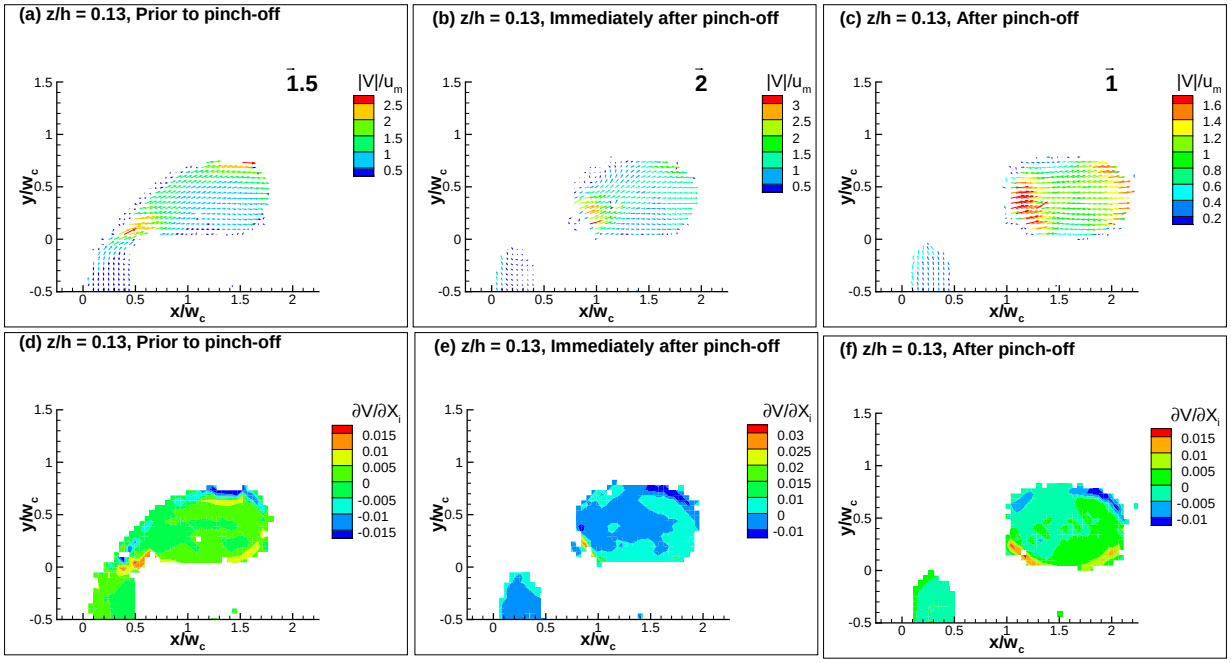

Figure 4.13: Velocity vector and velocity gradient contour plots at different phases for droplet generation in the transition regime ($Ca = 0.005$) for the middle plane *z/h = 0.13* for experiment water-glycerol without SDS. The Figures are as follows: (a) Velocity vector plot at start of pinch-off, (b) Velocity vector plot immediately after pinch-off, (c) Velocity vector plot after pinch-off and shape stabilization, (e) Velocity gradient contour plot at start of pinch-off, (e) Velocity gradient contour plot immediately after pinch-off, and (f) Velocity gradient contour plot after pinch-off and shape stabilization.

4.4 Discussion

4.4.1 Velocity Vector Plots

The μPIV results presented in the current study indicate that there were two regions that experienced the largest changes in their velocity field from filling to pinch-off. These planes were: planes close to the extreme walls (top and bottom), and the middle plane. The planes that were close to the extreme walls were subjected to two types of flow: flow of the gutter region, and flow in the lubrication region (see Figure 4.4). At those planes the highest velocities occur at the gutter region where the dispersed phase was subjected to the high shear from the continuous phase. An example of such velocity patterns for planes located close to the extreme walls are presented in Figure 4.14.

The reason that the flow in the gutter regions is fast can be explained by examining the dispersed phase confinement shape prior to droplet pinch-off. As the dispersed phase occupies the main channel it will form the lubrication and gutter regions. Since the lubrication region is very thin compared to the thickness of the gutter region [42] it will have a higher hydrodynamic resistance and flow in the gutter region will be larger. This pattern was experimentally observed many times for different flow regimes.

From what was presented in the results it was observed that the velocity patterns for droplet generation were complex. The complexity rises from the fact that the flow patterns inside the droplet are enduring a dynamic changes at different phases of droplet generation. Also, the nature of confinement adds another dimension to the complexity of the velocity patterns inside the droplet where the velocity patterns change according to position of the plane with respect to the top, bottom and side wall. This complexity can be observed by the changes in the location of the highest velocity regions inside the dispersed phase between planes and at different phases. A summary of the locations of the maximum velocity regions during the different droplet generation regimes that were examined are presented in Table 4.2.

An interesting observation was that the presence of surfactant (SDS in dispersed

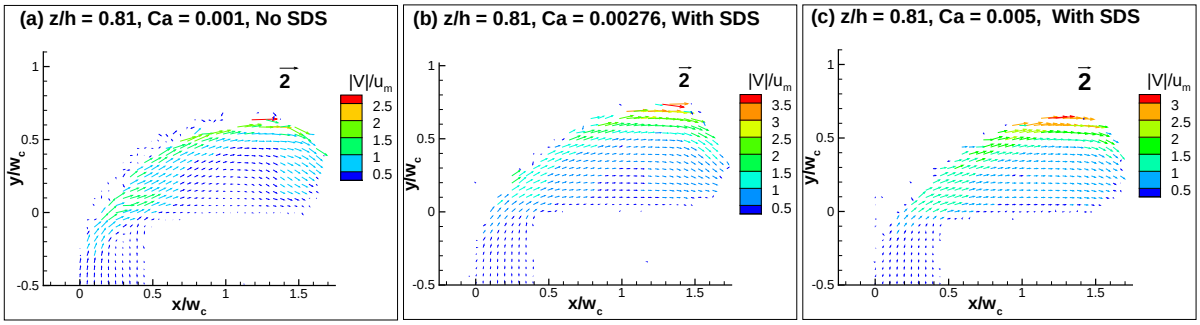

Figure 4.14: Velocity vector plots at the highest studied plane ($z/h = 0.81$) of three different experiments. The experimental condition for each figure is as follows: (a) Squeezing regime with no SDS ($Ca = 0.001$), (b) Transition with SDS ($Ca = 0.00278$), and (c) Transition with SDS ($Ca = 0.005$).

Table 4.2: The location of the highest velocity regions in the dispersed phase for the studied droplet generation regimes in the filling and start of pinch-off stages.

Droplet generation regime	**Location of maximum velocity during**	
	Filling stage	**Start of pinch-off**
Squeezing $Ca \approx 0.001$	At the gutter region	After the T-junction entrance
Transition $Ca \approx 0.005$	At the side wall	At the T-junction entrance
Dripping $Ca \approx 0.02$	Close to the side wall	At the distorted liquid/liquid interface

phase) above the CMC (critical micelle concentration) did not alter the general flow patterns inside the droplet as long as the Ca was matched. But, due to the reduction of the average velocity in the continuous and dispersed phases when matching Ca the magnitude of velocities and other flow properties were reduced.

It is important to emphasize that the velocity magnitudes were converted to a non-dimensional form by dividing the measured velocities from the μPIV experiments with the average velocity of the continuous phase (see Table 4.1). From what was observed in velocity field results the maximum velocity was around 3.5 more than the actual measured velocity for all tested results $\left(V_{max} \approx 3.5 \times \frac{|V|}{u_m}\right)$.

4.4.2 Velocity Gradient

The velocity gradients of the dispersed phase during the droplet generation for different generation regimes were examined in the current work to have an in-depth view of the velocity patterns. The gradients can be used to identify the regions that are exposed to a high shear. The velocity gradient was calculated from the two dimensional velocity vector plots for each examined condition. The results of the velocity gradients must be taken with consideration for the regions that are expected to have a three dimensional flow pattern, such as at the extreme planes close to the leading and trailing edge.

The velocity gradients showed interesting results for the different droplet generation regimes and different planes. In general, during the filling stage and at the extreme planes high velocity gradients were present at the edge of the liquid interface close to the gutter region of the channel that is located close to $y/w_c = 1$. At the middle plane and depending on the droplet generation regime the velocity gradient slightly differed. The most important conclusion was that during the transition regime the high velocity gradient in the filling stage provided a proof that shear is present in that regime.

It is important to emphasize that the results for the velocity gradients are qualitative. Although calculated from the quantitative Lagrangian velocity fields found

from the μPIV experiments they are not quantitative. This is due the fact the experiments were designed to find the velocity distribution up to a certain accuracy. In order to perform experiments that focus on higher order dynamic flow properties experiments should be designed around the property that is intended to be measured. For example, the use of larger magnification and smaller flow tracking particles will improve the spatial resolution that might be sufficient in improving the accuracy of velocity gradient estimation. However, arguments about the velocity gradients, although qualitative, are still valid and are evidence of interesting phenomena that occurs during droplet formation.

The results from the μPIV experiments were put in a non-dimensional form to unify the conditions. The non-dimensional parameter of the plane location was z/h which is the location of the plane of measurement divided by the channel height. It should be pointed out that lowest studied plane was located at $z/h = 0.13$ while the highest plane for most studied cases was at $z/h = 0.81$ [4]. There are two reasons that can cause this limitation for examining different planes: the depth of correlation of the optical assembly, and swelling of PDMS. The depth of correlation for the current assembly was found to be around 20.24 μm. Thus, for each examined plane location the true observed region had a thickness of 20.24 μm. The other source of reduction in the overall height is PDMS swelling. However, swelling is more severe in low and large aspect ratio (Aspect ratio = h/w_c) channels.

As a final comment, this work studied the droplet phases during generation at different stages. It is expected that the rapid changes in the velocity fields in the dispersed phase, especially at highest or lowest planes, are met with interesting flow dynamics in the continuous phase. Unfortunately, a μPIV examination of the continuous phase was not possible in the current setup because of experimental difficulties. These challenges include the difficultly in adding fluorescent particles to the continuous phase (silicone oil). The reason was that commercially available fluorescent latex or polystyrene particles will not disperse uniformly in oils. The only

[4]The highest plane that was measured from all experiments was located at $z/h = 0.87$. This was only for one experimental condition in the dripping regime. It is expected that the high flow rate in this regime may have caused deformation of the PDMS and allowed for examining the flow at this location.

commercially available particles that can disperse in oils are quantum dots (nano-scaled particles, $d_p = 20nm$). Unfortunately, they cannot be used for fast μPIV experiments since they need long exposures. The second major challenge, if the first one is solved, is the need of a high frequency laser with short pulses (μs to $nano$ s) that works at a different wavelength than that of the Nd:YAG laser. This is needed since the second phase must be studied at a different wavelength than that of the fluorescence of particles in water based solutions to differentiate the two liquid phases.

4.5 Conclusion

A μPIV system was used to examine and compare important phases for droplet generation in squeezing, transition, and dripping regimes for two fluid combinations with and without surfactant. The surfactant that was used in the study was SDS and was mixed with the dispersed phase with a concentration above CMC. Silicone oil was used as the continuous phase and water-glycerol mixture was used as the dispersed phase. All experiments were performed in PDMS microchannels since it provides proper wetting to silicone oil.

The experimental results indicate that at planes close to the top or bottom walls the velocity and velocity gradients patterns share similar trends in the filling and start of pinch-off for the droplet. The middle plane differed from the extreme planes for both the filling and start of pinch-off. The filling stage for the transition regime was similar to the dripping regime. The start of pinch-off shared similarities between the squeezing and transition regimes. Droplet pinch-off in the dripping regime differed from both the squeezing and transition regimes.

Chapter 5

Surface Treatment and Droplet Generation in Polycarbonate Microchannels

This chapter will present the approach used to alter the surface of polycarbonate (PC) microchannels from a hydrophilic state to a uniform hydrophobic condition sufficient for the generation of isolated water droplets in a carrier oil phase. The treatment approach was based on flow induced surface grafting of Dodecylamine (DDA) with the aid of heat. The other major part of the chapter will discuss the droplet generation process in PC microchannels and the difference between it and droplet generation in PDMS microchannels.

5.1 PC Microchannels and its Surface Treatment

The ability to engrave millimeter to micrometer features in materials and form confined channel networks is thought to be one the main reasons for the widespread of microfluidics research and applications during the past 15 years [10, 2]. Polymeric

materials are now the most widely used material types to make microchannels since they can be fabricated in many ways and offer many advantages such as good optical properties and low fabrication costs.

In this work, the droplets hydrodynamic transport properties were studied in Polycarbonate (PC) microchannels since it does not swell nor will it deform with low pressures [1]. PC is a thermoplastic that is naturally hydrophilic since it has a contact angle less than 90^o [2]. It has many engineering and biomedical uses since it comes in different grades including: industrial, optical, and medical grades. The generation of liquid segments that are fully encapsulated by another liquid is hard to achieve in bare PC since it is hard to achieve proper wetting conditions. An example of liquid segment generation patterns that were observed when using silicone oil and water as W/O (water in oil) or O/W (oil in water) segments are shown in Figure 5.1.

It is clear from Figure 5.1 that the surface condition of native PC does not support the generation of W/O nor O/W liquid segments. This was clear from the attachment of the liquid interface at the channel walls (interface pins) as well as the non-curved shape of the liquid/liquid interface between the fluids. For example, the highlighted regions in Figures 5.1 -(a), (b) and (c) present the interface of water as it pins to the PC channel wall when generated in silicone oil. The same discussion is applicable for generating silicone oil segments in a water-glycerol mixture, as shown in Figures 5.1 -(d), (e) and (f). It should be mentioned that another organic phase was tested which was hexadecane and similar patterns of interface attachment, shown in Figure 5.1, were observed.

Thus, for stable generation of liquid segments in another carrier liquid the surface condition of PC must be altered to a state that prefers a liquid type, organic or non-organic. In other terms the surface of PC must be changed to either a favorable hydrophilic or a favorable hydrophobic condition in order to generate isolated liquid segments.

[1] Modulus of Elasticity for PC is $E_{pc} = 2.6\ GPa$ while for PDMS, the most widely used microchannel material, is between $E_{PDMS} = 360$ - $870\ kPa$ based on the mixing ratio and curing process [16, 149].

[2] The measured the contact angle for the industrial grade PC with a contact angle measurement system was found it to be $82^o \pm 2.02^o$.

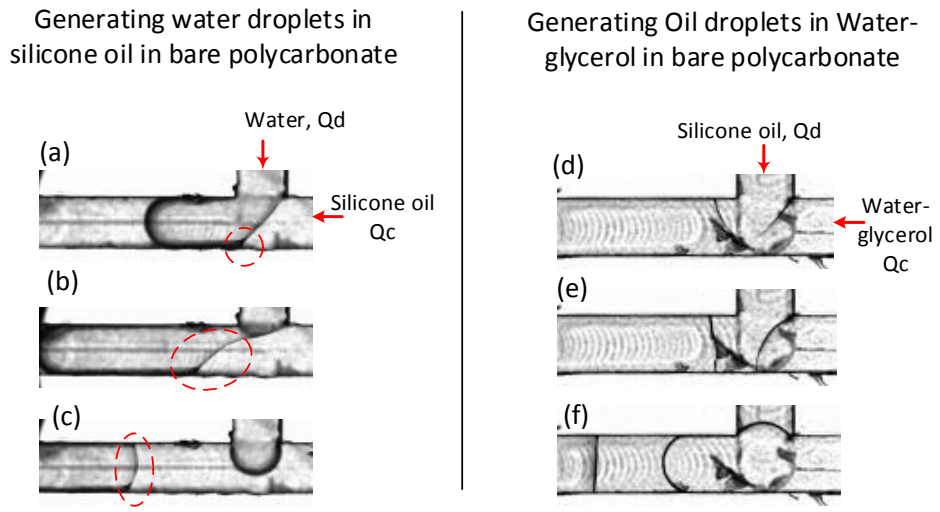

Figure 5.1: Droplet generation in native PC microchannels. Figures (a),(b) and (c) are different stages of generating a water segment in silicone oil, and Figures (d),(e) and (f) are different phases for the generation of a segment of silicone oil in water-glycerol mixture. The channel was fabricated in-house with the approach presented in Section 3.1.2.1 and channel shown in Figure 3.2.

From the literature review that was presented in Chapter 2 the approach that is applicable to be used in the current work was reported by Jankowski *et al.* [27]. Their approach was based on active surface grafting of Dodecylamine (DDA, $C_{12}H_{27}N$) in an enclosed channel with the aid of heat [27]. From their work they reported general rules for a successful surface grafting of DDA on PC surfaces.

Although Jankowski *et al.* [27] presented guidelines for treating PC to a hydrophobic state, their report was missing critical information about the surface treatment procedure for channels with different cross sectional areas (different surface to volume ratio). Their approach of DDA grafting is a function of flow condition with respect to the cross sectional area of the channel [3]. Thus, for microchannels that have different cross sectional areas the flow conditions presented by Jankowski *et al.* [27] may not be appropriate.

Since the current studies involve the use of channels with different cross sectional areas the approach that was used by Jankowski *et al.* [27] must be examined and optimized. The optimization process of the surface treatment of PC microchannels went thought two steps: first treating simple T-junctions geometries (see Figure 3.1.2.1) and examine their wetting, and secondly treating the complex microchannels networks that will be used in the droplet transport project. The variables that were optimized were: the concentration of DDA, the duration of the treatment, and the average velocity of the DDA solution in the microchannel.

5.2 DDA Surface Treatment Procedure

The treatment procedure was adapted from the work of Jankowski *et al.* [27]. The surface treatment trials were done with a continuous flow of DDA solution at a constant temperature at 60^o. The temperature was kept constant with an incubation chamber (SI-905, UVP/Analytika Jena AG). The solutions were pumped with a syringe pump (Pump 33, Harvard apparatus). To assure a stable flow rate Gastight syringes were used to pump the fluids. Teflon tubing with 1/6" OD (outer diameter)

[3] It should be mentioned Jankowski *et al.* [27] did not provide the height (h) of the channels that they treated.

was used to transfer the fluids between the syringe and the chip in the incubation chamber. Proper connections (Upchurch connectors, IDEX Health & science) were used to interface the fluids sources to the tubing and the microchannel ports. The DDA solution was prepared by w/w ratio in Ethanol. Proper mixing of the DDA solution was done with sonic cleaner prior to using the fluids in the treatment. It was noticed that preparing fresh DDA solutions, at most one day before the treatment, gave the most consistent results.

The treatment of the channels started with examining the channel network with a microscope to see if there were any defects or debris in the channel that might alter the flow and treatment. Afterwards, the channel network was left in the chamber for at least 45 min at 60^o to assure that the channel reached a constant temperature. The prepared DDA solution was then pumped through the chosen port for specific time duration. The time varied from 1.5-3 hours for different samples. Then, the treated channel was blown with air to remove all of the DDA solution inside the channel network. Afterwards, Isopropanol (IPA) was pumped through the channel network that was treated with twice the flow rate setting of the DDA solution for 0.5 hours. The final step of the treatment was to remove any IPA by blowing air [4]. The first trials for treating PC were done to simple T-junctions that were fabricated in house according to Section 3.1.2.1. Then the treatment was done to more complex channel networks. Typical outcomes for the attempted surface treatments of PC surface with DDA are presented in Figure 5.2.

It is clear from the different photographs shown in Figure 5.2 that under different treatment conditions the outcome of the DDA treatment changes. An interesting observation that was seen during the different trials of the treatments was that grafting of DDA alters the topography of the PC surface. This change was manifested by the presence of grainy structures on the surface of PC, as clearly shown in Figure 5.2 - (b2), (e), and (f) compared to images before treatment (a) and (d). The presence of grainy structures were also observed by Jankowski *et al.* [27] and they examined their features in non-bonded slabs of PC. Also, in other conditions cracks appeared

[4]It is important to mention that after each treatment all connections and syringes used were washed in the sonic cleaner multiple times in fresh baths of Ethanol or IPA to remove the residue of DDA that sticks to the connectors.

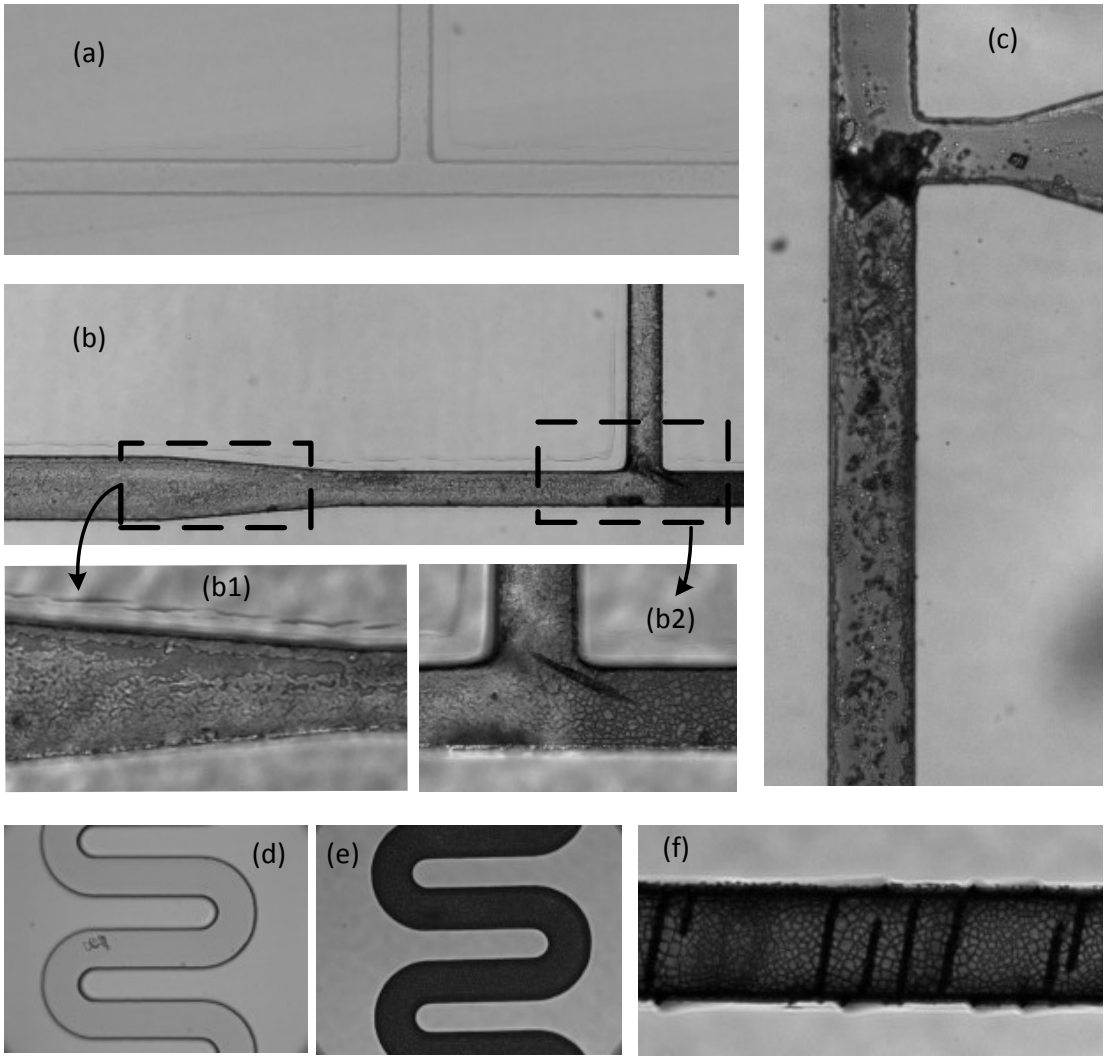

Figure 5.2: Images for PC microchannels before and after DDA treatment. Figure (a) the T-junction before the DDA surface treatment, (b) The T-junction after the DDA surface treatment flowing with 5% DDA and 4 mm/s average flow rate, (b1) A magnified image of the section leading to the T-junction, (b2) A magnified image of the treated T-junction, (c) A section of a T-junction containing defects treated with 5% DDA and 2 mm/s average flow rate of solution, (d) A section of serpentine channel before treatment, (e) A section of the serpentine channel after DDA treatment with 6% w/w for 2.5 hours, and (f) A section of a straight channel after DDA treatment showing cracks in the channel.

along the walls of the PC, also shown in Figure 5.2. These cracks appeared when pumping DDA solutions at average speeds that are less than 0.5 mm/s inside the microchannels or prolonged treatment time ($>$ 2.5 hrs).

One observation was that at high flow rate conditions (average velocity of 4 mm/s and above) results in having regions of the microchannel that were not covered with DDA. This pattern is clearly shown in Figure 5.2 -(b1). Those non covered regions of the surface of the channel will affect the wetting of the channel and may cause regions where the interface of the dispersed phase pins to.

Also, in situations where the concentration was above 5.5 % there were more chances in getting cracks on the surface of the channel. The highest concentration that was examined was 7 % w/w of DDA in Ethanol where it showed the most cracks. An example of such cracks if shown in the Figure 5.2- (f). Although, cracks were present in some treated microchannels they did not have an effect on the transport of droplets, from what was observed in video recordings.

The other approach to examine the properties of the surface of PC after DDA treatment was to observe the droplet generation and transport in the treated microchannels. Typical results for droplet generation and transport after surface treatment with DDA for various treated channels are presented in Figure 5.3.

The main indicators of proper wetting were: the smooth transition of the interface prior to droplet pinch-off, and the curved shape of the leading and trailing edges for formed droplets. In conditions where the DDA treatment was not successful the droplet interface will pin to the channel walls during droplet generation or during the transport. Another indication of an unsuccessful surface treatment is the occurrence of a flat interface at the leading or trailing edge of a droplet. The different photographs shown in Figure 5.3 are good representations of the various scenarios of the surface treatment outcomes. Figure 5.3 -(a) shows the proper wetting condition for stable droplet generation with isolated droplets moving across the channel. This wetting condition was the appropriate case for performing hydrodynamic studies of liquid droplets. The rest of the scenarios shown in Figure 5.3 -(b), (c), and (d) represent the conditions where the surface treatment was unsuccessful since there is either droplet interface pins during the droplet transport (Figures 5.3 -(b), (c), and

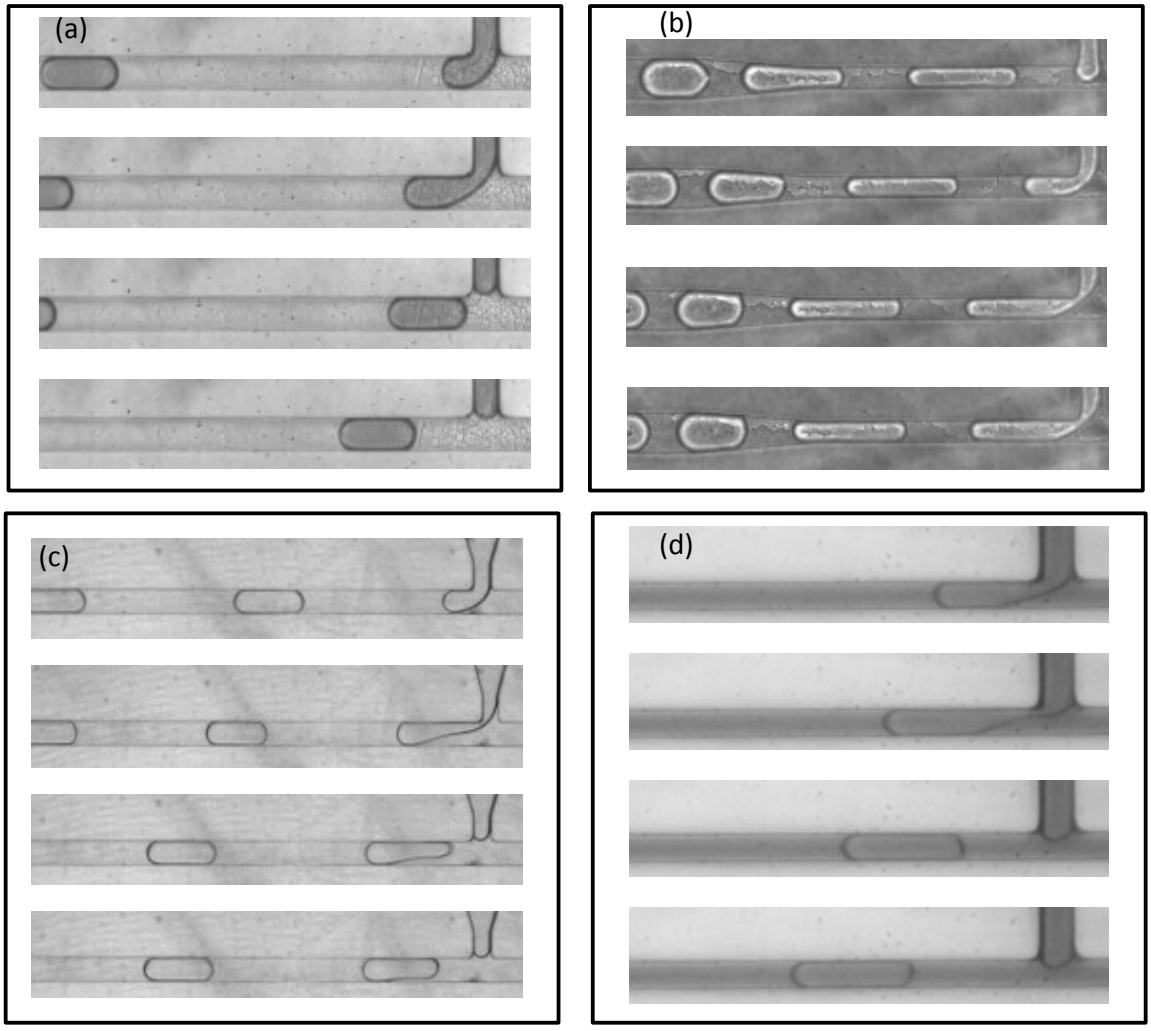

Figure 5.3: Various conditions for droplet generation at a T-junction and transport for various PC microchannels treated with DDA. The different photographs show diverse wetting conditions for channel treatment. The solutions used were water based in the disperse phase and hexadecane in the continuous phase. Figure (a) Proper wetting for stable droplet generation, (b) Unsuccessful treatment where droplet interface pins to channel walls at different locations in the channel, (c) Non uniform wetting at T-junction and the interface pins to some wall locations, and (d) Non uniform wetting at T-junction and multiple locations of droplet interface pins to the walls during droplet transport.

(d)) , or non-uniform transition of the interface during the droplet pinching off in the generation (Figure 5.3 -(c), and (d)).

The results that were observed from the droplet generation of the surface modified PC microchannels defined the general rules for the success of grafting DDA on PC microchannels. These rules include the average velocity of the DDA solution, continuity of the flow rate, the stability of temperature, and duration of the treatment. From what was observed the average velocity for the DDA solution in a microchannel should be in the range: 0.7-1.2 mm/s. Also, it should be pointed out that the flow should be continuous and not disrupted as much as possible. Sources of flow disruptions in microchannels include the presence of gas bubbles in the channel networks, the mismatch of the syringe diameter with the flow rate inside the channel [65], and the presence of debris in the microchannel (See Figure 5.3 -(c)). The duration of the treatment should be between 1.5 to 2 hours.

5.3 Surface Treatment of Complex Channel Networks

The first couple of DDA treatment optimization tests showed that altering the surface property of PC microchannels can be achieved in simple T-junction designs. Those results motivated the further investigation of examining the surface treatment in complex channel network designs that will be used in the droplet hydrodynamic transport project. The channel designs that were examined had multiple ports as inlets and outlets, as shown in Figure 3.3. Thus, the rules that were found for the surface treatment of PC microchannels for simple T-junction design should be adjusted for the complex channel networks.

The hardest rule to maintain for proper surface treatment was keeping the average velocity inside a microchannel section in the range of 0.7 - 1.2 mm/s. This difficulty arise since in complex channel networks with different junctions the flow splits in the branches according to the junction type, the flow condition, and the hydrodynamic resistances of the microchannels. Moreover, the DDA solution should

flow continuously without disruptions or increasing the time of exposure throughout the channel network.

The step for balancing the flow rates of splitting junctions was done with balancing the hydrodynamic resistance ratios. This can be done by simple calculations or by using the electrical circuit analogy of channel networks and finding the resistance and flow rate conditions. Tina-Ti v.9 (Texas Instruments) was used to find the flow conditions complex channel networks from the analogy of electrical circuits to fluid flow. With Tina-Ti changing the location of the constant current [5] source with respect to the flow splitting junction gives the amount of current that splits between the branches of the junction. In the case of a junction having very high current draw or no current at all, the source location should be changed or another current source should be added.

To illustrate the different treatment scenarios an example of treating a complex microchannel network will be presented next. A schematic of the microchannel network and the electrical circuit analogy for the resistance of the network is shown in Figure 5.4. For that channel network and by using one port as the fluid source the scenarios of the surface treatment can be as follows:

Scenario 1 using 1^{st} inlet as the source: From the resistance ratios it can be seen that the flow will divide into section 2 and 3. However, when the flow reaches the dilution stream (section 4) it should choose the dilution stream channel and will not flow and treat the test section (section 5).

Scenario 2 using 2^{st} inlet as the source: Most of the flow will go to section 1 and will not go to sections 3, 4 or 5.

Scenario 3 using 3^{rd} inlet as the source: The flow will split between sections 5 and 3+1 according to the hydrodynamic resistance ratio with most of the flow going to section 5. Section 2 of the design will not be treated because of the resistance ratio and the splitting of flow from mainstream to branch.

[5] The constant current source was used to emulate the condition from the syringe pumps since syringe pumps provide constant flow rates.

Scenario 4 using 4^{th} inlet as the source: The flow will only go through sections 5 and 4. The rest of the sections will not be treated since the hydrodynamic resistance is very high.

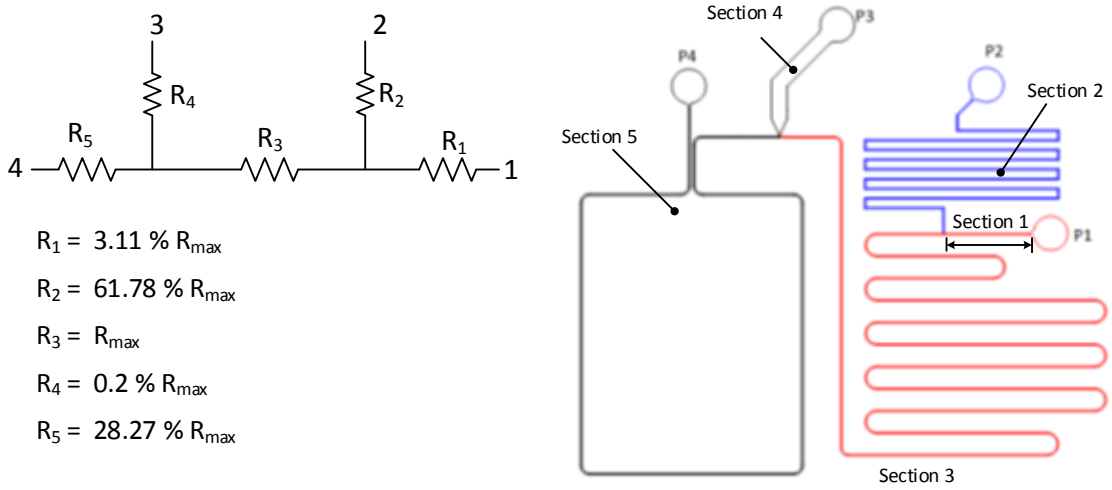

Figure 5.4: A schematic illustration of a microchannel network and its electrical circuit analogy. The numbered ports in the electrical circuit schematic indicate the inlets of the current source that is similar to the actual flow port in the channel schematic. Indicated in the Figure the ratios of the electrical resistances to the maximum total resistance of the entire channel network.

From what was presented in the treatment scenarios above it is expected that the best treatment scenario is Scenario 3 by using the 3^{rd} as the main fluid source. This will assure the stable flow rate and treatment of the important channel regions of the microchannel. An improvement to this scenario can be achieved by using two ports as fluid sources. This improvement was done by pumping the DDA solution through the second inlet but with a flow rate lower [6] than the flow rate from the third inlet. This will improve the wetting condition of the dispersed phase channel and also section 1.

[6]Electrical circuit analysis with Tina-Ti showed that a 20% flow rate in from the second inlet will not cause any flow disturbance for the flow coming from the third port.

Another flow balancing approach that can be used is to connect the outlets ports of the channel network with tubing with different hydrodynamic resistances. Most tubing used for the fluid supply has a circular cross section. It is known that the hydrodynamic resistance of a channel with circular cross section is [12]:

$$R_{hyd,cir} = \frac{8\mu L}{\pi R^4} \tag{5.1}$$

Where R is the diameter of the tube, and L is total length of the tube. Thus, if the tubing diameter is changed to one that has half the radius with the same length there will be an increase of hydrodynamic resistance by 16 times. Hence, by using different tubing with different radius flow could be balanced.

The final point to mention about the surface treatment of PC microchannels with DDA is that sometimes it is hard to achieve proper conditions of surface treatment in all microchannel sections. For that reason, some junctions will not be treated properly due to the flow restrictions. In these situations it is acceptable to sacrifice a channel junction that is not important for the study. For example, considering the channel network shown in Figure 5.4 the important regions of the design were: the T-junction (Section 1), the region of the channel that connects the T-junction to the dilution junction (Section 3), and the measurement section (Section 5). In these regions it is important to have a uniform treatment of the DDA on the surface. The dispersed phase channel network (Section 2) is not important except at the region where the T-junction is formed. Thus, if it was not possible to treat it with proper flow conditions, this section could be neglected by treating it with the improper flow condition.

5.4 Droplet Generation in PC Microchannels

For passive droplet generation in the squeezing, transition or dripping regime it was expected that the microchannel material will not have an effect on the droplet generation process in T-junction designs as long as the wetting condition was satisfied. This is due to the fact that the process of droplet generation is a function of the geo-

metrical aspects of the T-junction, flow conditions, and fluid properties [28, 54, 64]. The droplet generation process in T-junction microchannels was found to have three main stages: droplet filling, squeezing of interface and pinch-off. Most of the work that was reported in the literature about droplet generation focused on the volume of droplets as a function of the flow and channel geometrical properties such as height and widths of the channel [54, 47]. However, there is another parameter that might be of importance in some situations that is frequency of droplet generation [64]. When the frequency is considered the lag stage, or lag duration, between the formations of successive droplets is important.

In passive generation of droplets in T-junction microchannels made from PDMS it was observed that the lag stage includes a receding of the dispersed phase interface inside its channel imminently after droplet pinch off. This retraction of the interface increases the duration of the lag stage. Glawdel *et al.* [64] reported this phenomenon during droplet generation in T-junction designs. They examined the parameters that affect the receding of the interface and proposed a variable L^*_{lag} which identifies the distance that the interface recedes after pinch-off. Glawdel *et al.* [64] proposed that this deflection of the interface is similar to viscous-capillary pinch-off. From their experimental observation they proposed that the L^*_{lag} is a function the viscosity ratio and the Ca_d according to:

$$L^*_{lag} = \frac{\eta^{1/2}}{Ca_d} \tag{5.2}$$

where η is the viscosity ratio of the dispersed phase to the continuous phase, and Ca_d is the dispersed phase capillary number. Typical images for the retraction of the interface after droplet pinch off in PDMS microchannels are shown in Figure 5.5.

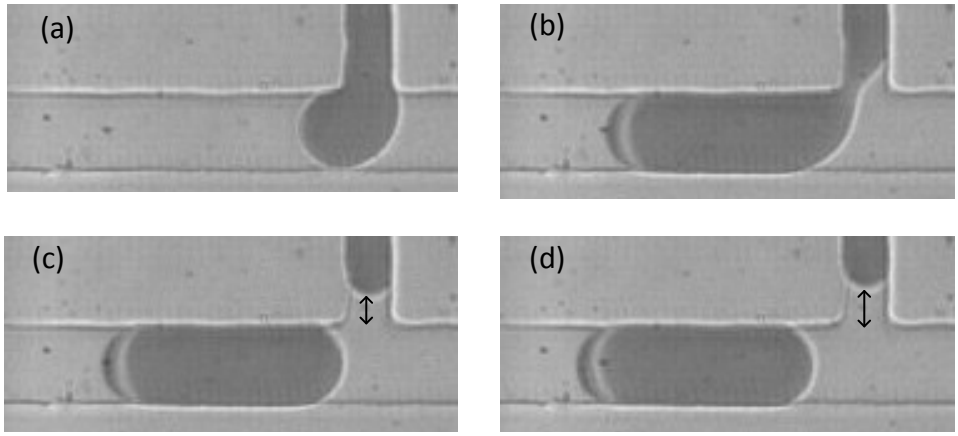

Figure 5.5: Images for the droplet generation stages in a T-junction made from PDMS. The fluids that were used were and glycerol mixture with food dye as the dispersed phase and silicone oil as the continuous phase. Figure (a) Image from the filling stage, (b) Image from the pinch off of a droplet, (c) Immediately after pinch off and the retraction of the interface, and (d) The maximum retraction of the interface for this droplet generation step.

The results shown in Figure 5.5 present the interface retraction that occurs after droplet generation in PDMS based microchannels, similar to what was reported by Glawdel *et al.* [64]. This retraction is highlighted in Figure 5.5 -(c) showing the movement of the dispersed phase interface inside the channel. Figure 5.5 -(d) indicates the maximum distance that the interface moves after the droplet is generated. It is important to emphasize that the deflection length of the interface varies with the flow rate of the dispersed phase, and the geometrical aspects of the T-junction, as was reported by Glawdel *et al.* [64]. However, this change in length of interface retraction varied for different microchannel networks fabricated from the same master mold.

The droplet generation experiments that were done with a T-junction made from DDA treated PC showed that there was no retraction of the interface after the detachment of the droplet. This was clearly shown in Figure 5.3 -(a) where after the droplet generation the dispersed phase interface stayed at the inlet of the T-

junction. This contradicts with what was noticed for PDMS microchannels where the droplet phase retracts back (Figure 5.5). These findings raised the question on what is really the source of the interface deflection during droplet generation in PDMS microchannels.

The main difference between PC and PDMS is the hardness of the material and the pressure compliance. PDMS has larger compliance compared to PC and it is expected that in situations where there is a sudden change in pressure the volume of PDMS will change more than PC. And since the droplet generation process involves rapid pressure changes at different stages of the droplet generation [30] it is expected that the impact of pressure changes will effect PDMS more than PC. Thus, the cause of the retraction of the interface is the pressure compliance of PDMS.

The proof that the pressure compliance is the cause of the interface deflection was observed unintentionally. In the priming stage of the PC T-junction microchannel for droplet generation, plugging the fluid ports sometimes introduces air pockets at the inlet of the microchannel. These air pockets will travel through the channel network of the dispersed phase and are then generated as bubbles at the T-junction. One aim for the priming step was to remove these air bubbles from the channel network since their presence in the channel will disturb the droplet generation. It was observed that when a bubble was generated at the T-junction the interface retracts back inside the dispersed phase channel. An example of such deflection is presented in Figure 5.6. This was similar to what was observed with PDMS microchannels. Hence, the reason for the retraction of the interface is due to the pressure compliance of the system. For PDMS microchannels this compliance is traced back to the nature of PDMS. In the example presented in Figure 5.6 this compliance was related to the compressibility of air.

Although the property of interface retraction appears unimportant from a general view of the droplet generation, it is significant for systems that require the knowledge of droplet spacing for passive merging and sorting applications. This importance arises since the larger the deflection the less frequent droplet generation leading to more spacing between droplets. Thus, high frequency droplet generation systems need harder material and fluids that are not affected by the sudden pressure

fluctuations that occur after a segment is generated [30].

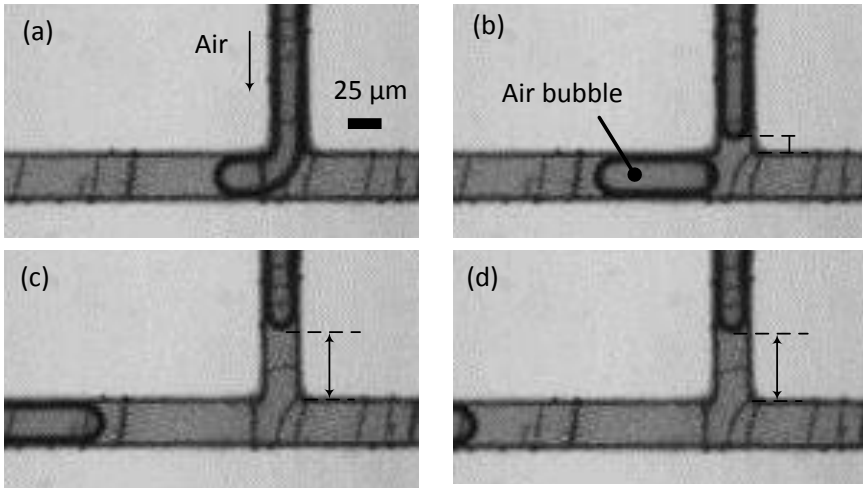

Figure 5.6: Bubble generation in a PC microchannel during the channel priming stage. The images were taken at different stages of bubble generation to show the interface deflection after the generation of the bubble. Figure (a) Filling stage, (b) Immediately after pinch of, (c) and (d) after pinch off and segment generated. The arrows indicate the amount of the interface deflection inside the channel.

5.5 Discussion

Surface treatment of PC with DDA is based on the process of DDA molecules anchoring themselves on PC. This process is a chemical reaction influenced by the convection/diffusion flow condition of the DDA solution. The concentration of DDA in the solvent affects the attachment success of DDA molecules to bare PC locations. The flow condition affects both the anchoring of the molecules and them shearing off the surface of PC. If the flow rate is high DDA molecules may not uniformly anchor themselves to the PC surface. This will lead to regions on the surface of PC where batches of DDA will graft while others are not grafted, as seen in Figure 5.2. This result in partial wetting in some regions of PC, as was observed in several experiments

that were done with treated PC (see Figure 5.3 -(b), (c), and (d)).

It is important to stress that the results presented on the treatment patterns relay on optical imaging of the microchannel prior and after the DDA treatment. The physical or chemical changes on the surface of PC were not examined since all treatments were done to bonded microchannel networks. The examination of changes in surface chemistry of PC after DDA treatment needs proper experimental approaches that emulate the actual flow condition and the separation of the channel and the substrate without affecting the treated channel. However, this type of study is out of the scope of the thesis and is an open problem for future research.

5.6 Conclusion

In this chapter the rules for treating complex networks of PC microchannels to a hydrophobic state for stable aqueous droplet generation was presented. Photographs of the surface of PC before and after treatment indicate that DDA anchors to the surface of PC and changes the topography of the surface. Droplet generation for a PC microchannel treated successfully with DDA showed stable and non-wetting droplet generation and transport in microchannels. The sets of rules and conditions for successful treatment of DDA on PC were modified from what was reported by Jankowski *et al.* [27] to criteria that can be applied to complex channel networks. One important rule is that the proper surface treatment of complex networks PC microchannels involves the proper balancing of the flow rates of the DDA solution throughout the network.

An interesting pattern that was observed for droplet generation in PC microchannels was that after the pinching-off of liquid droplets there was no retraction of the interface into the dispersed phase channel as was seen in passive droplet generation in PDMS microchannels. This non movement of the interface is related to the low pressure compliance of PC compared to PDMS. This finding indicates that T-junction microchannel fabricated from PC will have a higher droplet generation frequency for the same flow and geometrical conditions the channel compared to microchannel fabricated from PDMS or potentially other soft materials.

Chapter 6

Hydrodynamics of Liquid Droplet Transport in Rectangular Microchannels

In this chapter a study of the hydrodynamic properties of liquid droplets generated and transported in polycarbonate (PC) microchannels will be presented. The study examined the excess pressure, hydrodynamic resistance and slip factor of small liquid droplets with lengths of $w_c \leq L_d \leq 1.5 \times w_c$ as they are transported in a rectangular microchannel. Measurements for the droplet resistance were done with an indirect measurement approach where the changes in the flow rate in the presence of droplets at an applied pressure were used to estimate the hydrodynamic properties of liquid droplets. Up to the limits of the experimental system and the microchannel design droplet generation aspects the study examined changes of flow conditions and fluid properties [1].

[1]The results of this chapter were presented in the APS-March Meeting 2014 [150]. Partial funding for the fabrication of the microchannels was provided by CMC Microsystems.

6.1 Droplet Resistance Measurements

An important flow property associated with the transport of droplets, or fluid segments in general, in microchannels is the added flow resistance from their presence compared to a single phase flow [38, 123]. The shape of the fluid segments, the fluid wetting properties with the confining microchannel, the fluid properties, and flow conditions are all factors that contribute to the added resistance. For a single liquid droplet transported within a confining continuous phase the pressure drop across the droplet phase comes from two parts: the Laplace pressure jump at the curved interfaces, and the bulk fluid resistance due to viscosity [38, 62, 123]. The pressure drop across the continuous phase also adds to the total pressure drop in the channel. There are two pressure drop contributors from the continuous phase: the pressure drop in the liquid segments that separate droplets, also known as plugs L_{plugs}, and the encapsulation regions that surround droplets. Figure 6.1 illustrates the main sources of the pressure drop across a representative fluid segment between two droplets.

The total pressure drop for the two phase system illustrated in Figure 6.1 can be found from Equation 6.1 [38]:

$$\Delta P_{total} = \Delta P_{plugs} + \Delta P_{encap} + \Delta P_{drop,body} + \Delta P_{caps} \tag{6.1}$$

where ΔP_{total} is the total pressure drop within the microchannel, ΔP_{plugs} is the pressure drop that occurs in the continuous phase due to the viscosity of the phase, $\Delta P_{drop,body}$ is the pressure drop due to the viscosity of the dispersed phase, ΔP_{caps} the pressure drop due to the existence of the curved interface, and ΔP_{encap} is the pressure drop in gutter regions surrounding the droplet. It should be pointed out that the pressure drop across the lubrication regions are assumed to have no contribution since that region has a very high hydrodynamic resistance compared to the gutter regions [62]. For rectangular microchannels the main parts of Equation 6.1 will be separated next. For the carrier continuous phase the pressure drop is [62, 123]:

$$\Delta P_{plugs} = a\frac{\mu}{w_c h} L_{plugs} u_m \tag{6.2}$$

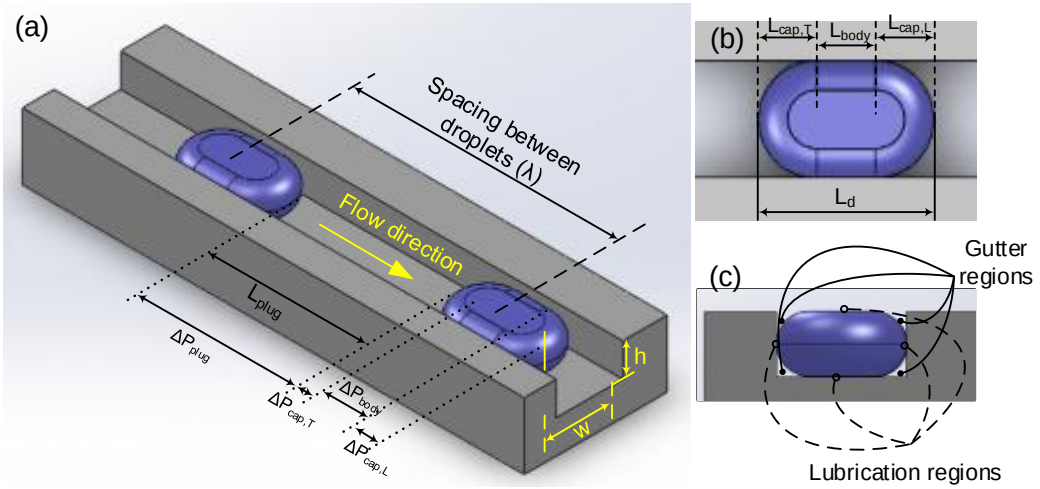

Figure 6.1: A 3D schematic illustration of a pair of droplets in a microchannel with the important geometrical factors of the droplet and the channel presented in the figure. The subscripts L and T for the droplet refers to the leading and trailing edges of the droplet (Courtesy of Michael Winer, with modifications.).

where ΔP_{plugs} is the pressure drop of the liquid plug, a is the channel shape factor, μ is the viscosity of the continuous phase, w_c channel width, h channel height, L_{plugs} is the length of the continuous phase plug, and u_m is the average velocity of the continuous phase.

The total pressure drop in the segmented droplet phase is a combination of two factors: viscous and Laplace pressure jump at the interface. For a single or a train of droplets the total pressure drop in the droplet phase can be estimated from [62, 123]:

$$\Delta P_{droplets} = \Delta P_{drop,body} + \Delta P_{caps} = b\frac{\mu_d}{w_c h} L_{d,total} u_d + n_d \cdot c_\lambda \frac{\gamma}{h} Ca_d^{2/3} \tag{6.3}$$

where b is a geometrical factor for the shape of the droplet, μ_d is the droplet viscosity, $L_{d,total}$ is the total length of all droplets inside the channel, u_d is the speed of a droplet, n_d is total number of droplets inside the channel, c_λ is a factor that accounts for the viscosity ratio, γ is the interfacial tension, and Ca_d is the Capillary number based on the dispersed phase average velocity. From Equations 6.2, 6.3 it is evident that the pressure drop due to the presence of liquid segments is a complex property since it involves several contributing factors. These equations capture the apparent physical conditions that are present for a droplet segment and estimate the pressure drop across it. However, the nature of segmentation in rectangular microchannels and the viscosity of the droplet create a challenge for such analytical or numerical analysis of estimating the pressure drop across a droplet as well as the flow of droplet/droplets. Furthermore, there might be other secondary flow contributors that affect the pressure drop of droplets, such as droplet entrainment due to the presence of a train of droplets [137]. For those reasons, experimental studies have been used for estimating the hydrodynamic properties during segmented flow conditions.

A brief summary of the literature that presented measurements of the pressure drop of liquid droplets was presented earlier in Section 2.4.2 and it indicated that information regarding the pressure drop for small droplets ($L_d \geqslant w_c$) was not available [6, 15, 72, 137]. This was the main motivator for examining the hydrodynamic properties of small droplets. The second motivator of the study was to examine the nature of change of droplet transport properties when the fluid conditions are

changed by adding surfactants or increasing their viscosity. This information is important for various applications of droplet microfluidics systems such as droplet splitting or droplet sorting [135]. Unlike other work reported in the literature, the current study used PC microchannels that were treated with DDA as a channel substrate material to eliminate swelling and pressure compliance effects associated with other commonly used microchannel materials.

6.1.1 Measurement Concept of the Hydrodynamic Resistance

If a laminar flow of a Newtonian fluid occurs in a channel with a uniform cross section the pressure drop is linearly related to flow rate [10, 12]. This relation is simply formulated as:

$$\Delta P = R_{hyd} \cdot Q \tag{6.4}$$

where ΔP is the pressure drop, Q is the flow rate, and R_{hyd} is the hydrodynamic resistance of the channel. Equation 6.4 is a well-known equation and commonly used as the analogue between electrical systems and fluid systems. The parameter for the proportionality in Equation 6.4 is the hydrodynamic resistance of the channel. The hydrodynamic resistance of a rectangular channel containing a Newtonian fluid with width larger than its height ($w_c > h$) was presented earlier in Equation 3.2.

In this work the measurement of the hydrodynamic resistance or excess pressure of one droplet is achieved by measuring the reduction in the flow rate during the presence of a train of droplets in a test region and compare it to the condition without droplets, or reference condition. The main rules for using this approach are to have identical droplets separated with uniform spacing. Also, the measurement of the flow rate (Q) must be performed on a channel segment with a known pressure drop (ΔP). These issues were considered when designing the microchannel network, as was presented in Section 3.1.2.2.

In a typical experiment the controlled parameters were: the applied pressures ($P_{applied}$) at the source junctions, the continuous phase physical properties, and

droplet phase physical properties (viscosity μ_d and interfacial tension γ). The measured parameters were: Q_{with_drops} the flow rate with droplets, Q_{Ref} the reference flow in the absence of droplets,($R_{hyd,Ref}$) is the hydrodynamic resistance in the absence of droplets, L_d the length of droplet, and λ the spacing between droplets. During each experimental run a train of droplets were introduced in the measurement area of the microchannel with a uniform size and stable spacing which will cause a change in the recorded flow rate. This change in flow rate is directly related to the hydrodynamic resistance of the droplets. From that change the total pressure drop due to the existence of droplets can be calculated from:

$$\Delta P_{total} = \Delta P_{plugs} + n_d \cdot \Delta P_{droplet} \tag{6.5}$$

where n_d is the total number of droplets inside the study area, and $\Delta P_{droplet}$ is the pressure drop of a single droplet. The pressure drop in the continuous phase (plug) can be found with an indirect approach by subtracting the total length of droplets that are present in the experiment from the total length of the channel measurement section. This calculation is formulated as:

$$L_{plug,total} = L_{channel} - n_d L_d \tag{6.6}$$

where $L_{plug,total}$ is the total plug length, $L_{channel}$ is the total length of the channel, n_d is the total number of droplets in the area of study during an experiment, and L_d is the droplet length. Equation 6.6 assumes that the length between a droplet leading and trailing interfaces (tip to tip) is representative of the total length of the plugs without considering the curved droplet shape effects. From Equation 6.6 the resistance of the channel that contains only the continuous phase can be calculated with:

$$R_{hyd,plugs} = \frac{L_{plug,total}}{L_{channel}} R_{hyd,ref} \tag{6.7}$$

Since the applied pressure and measured flow rate of an experimental set is for both the plugs and the droplets, the hydrodynamic resistance of droplets can be estimated from:

$$R_{hyd,drops} = \frac{P_{applied}}{Q_{with\_drops}} - R_{hyd,plugs} \tag{6.8}$$

where $R_{hyd,drops}$ is the hydrodynamic resistance for the train of droplets in a microchannel. The excess pressure is defined as the added pressure due to the presence of droplets [72]. It is calculated by finding the change of pressure due to the presence of droplets compared to the condition where droplets are absent for the same flow rate. In the current experimental approach it could be found by first estimating the pressure needed to give the plug region a flow rate that is similar to what was measured with drops. The expected pressure drop for the continuous phase to achieve the same flow rate for the same experiment with droplets is found from:

$$\Delta P_{plugs} = R_{hyd,plugs} \cdot Q_{with\_drop} \tag{6.9}$$

Hence, the excess pressure from the presence of droplets in the channel network can be found from:

$$\Delta P_{drop,total} = P_{applied} - \Delta P_{plugs} \tag{6.10}$$

where $\Delta P_{drop,total}$ is the excess pressure due to the presence of a train of droplets, $P_{applied}$ is the applied pressure at the junction that is needed to create flow in the two phase system, and P_{plugs} is the pressure drop across the continuous phase.

The properties of a single droplet can be found by dividing the results of Equations 6.10, and 6.8 by the number of droplets (n_d) that are present in the study section during an experiment. The number of droplets was found by dividing the total length of the channel test area, presented in Table 3.1, by the measured spacing between droplets during an experiment illustrated in Figure 6.1-(a) $\left(n_d = \frac{L_{channel}}{\lambda}\right)$.

6.1.2 Experimental Procedure for Droplet Resistance Measurement

Experiments started by priming the DDA treated PC channel network to assure proper wetting of the channel and to remove any residual liquids or bubbles that might be in the network from prior experiments and eliminate any hysteresis effect [52]. The priming was done by flushing the microchannel network with hexadecane through ports 1 and 3 (see Figure 6.2) while keeping ports 1 and 4 open

to atmosphere for at least 30 minutes. Afterward the dispersed phase tubing was connected to port 2 and pressure was applied until droplets were generated with a stable size and spacing. This step took at least 45 min. Meanwhile, the flow sensor tubing was flushed with hexadecane to remove any bubbles or other fluid segments that might be trapped in the tubing from earlier experiments.

The applied pressure P1 and P2 control the size of generated droplets. P3 serves two purposes: control the spacing between the pairs of droplets and to apply a known pressure at the desired location of the channel. At the start of each droplet generation condition (constant P1 and P2) droplets were generated at the T-junction located upstream and then transported to the dilution stream and test area. The spacing between droplets was increased between the train of droplets until the transport properties (L_d and λ) reached a steady condition. This was identified by the stable size and spacing between pairs of droplets. Then, a video was recorded at the area of interest (AOI) with the high speed camera (Phantom 210) with raw video format (*.cine* format) that allowed for recording large files (up to 2 Gb of video). This setting assured that the first pair of droplets that was recorded entering the area of study should exit the area of study during the recording of the video. The experimental conditions associated with captured videos (ie. applied pressures, and measured flow rate) were also recorded. Typical images taken at the different locations of the channel network during the process of droplet generation and transport are presented in Figure 6.2.

After recording a video at the first pressure set (P1, P2, and P3), the pressure at the dilution stream was reduced to decrease the spacing between the pairs of droplets. The flow was left to stabilize for at least 5 min. This was indicated by the stabilization of the flow rate measured by the flow sensor. The main benefit of this approach, incrementally decreasing the pressure at the dilution stream, was to reduce the feedback effects from the dilution stream pressure to the T-junction droplet generator. This is due to the fact that size and spacing of droplets generated at the T-junction are affected by the flow condition downstream [58, 59, 62]. By incrementally decreasing the pressure at the third junction the feedback effect will be dampened by the long resistance in the channel and the presence of droplets.

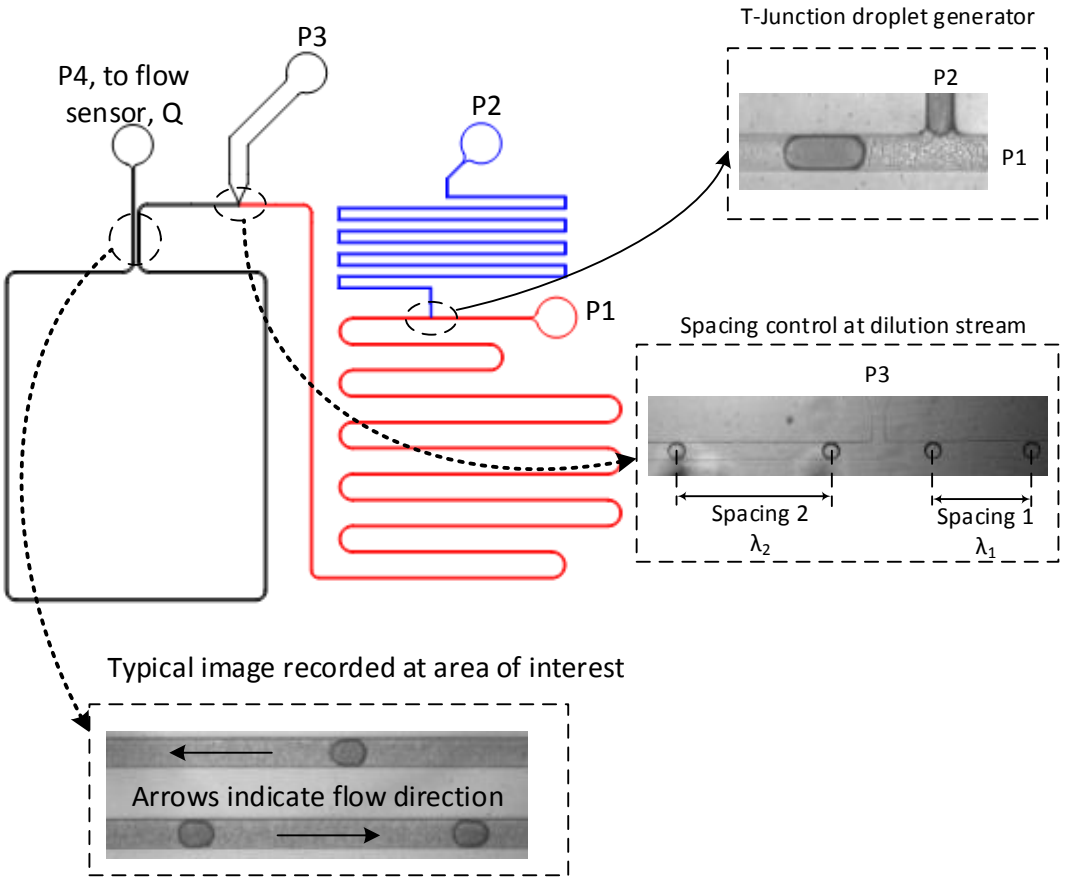

Figure 6.2: A schematic illustration of the channel network design used for studying the hydrodynamic properties of liquid droplets in microchannels along with images from recorded videos at different sections of the network.

Examples for the droplet size and spacing measured for different settings of the pressures are presented in Table 6.1.

From Table 6.1 it is clear that the variation in the pressures of the input ports affect the size of a single droplet and the spacing between pairs of droplets. The size of the droplets is controlled, mainly, by the input pressures at junctions 1 and 2 (P1 and P2). The spacing between droplets is controlled by the applied pressure at the dilution stream (P3). The experimental approach of starting experiments at a relative high pressure at the dilution stream and incrementally decreasing it showed that it has a minimal effect on the droplet size variation for a certain experimental set (constant P1 and P2).

The procedure mentioned above was repeated for each droplet generation pressure setting (P1, and P2). Video files and the experimental conditions were recorded for each pressure setting that correspond to different droplet spacing (λ) and speed (u_d). The final stage of an experiment was to find the base hydrodynamic resistance of the measurement channel section (black section in Figure 6.2). This was done by flushing out all droplets in the channel network and then removing the pressure ports P1 and P2 and closing them with a proper plug connector. Afterwards, pressure was applied from the dilution port P3 and the corresponding flow rate was measured. This was repeated with different pressures in order to find the P and Q relation for the measurement channel without droplets. Typical P and Q measurements for different experimental conditions with droplets compared to the reference condition (without droplets) are presented in Figure 6.3.

It is clear from Figure 6.3 the reference condition shows a linear relation between the applied pressure and measured flow rate. This relation was expected since the channel had a uniform cross section and contained one type of fluid. The slope of the reference line is the reference hydrodynamic resistance of the microchannel ($R_{hyd,ref}$). The goodness of fit for the linear regression coefficient for the P and Q relation of the reference condition gave a value of $R^2 \geq 0.98$. Furthermore, the slope of the line, that is the reference hydrodynamic resistance, was within 5% of the calculated hydrodynamic resistance of a straight microchannel calculated from Equation 3.1.

Another representation of the experimental outcomes presented in Figure 6.3 is

Table 6.1: Typical experimental conditions settings during the droplet resistance measurements in PC microchannels. Applied pressures were at the inlet junctions of the microchannel network 6.2. The measured droplet length L_d is the average droplet length for all measured droplets at each experimental condition. The spacing is measured between droplet to droplet centroids. The uncertainty included in this table for the droplet length and spacing was the standard deviation of the actual measurements in μm.

Applied pressures at junctions ($mbar$)			Droplet Length	Spacing
P1	P2	P3	L_d (μm)	λ (μm)
200	200	100	128.7 ± 2.83	18,980.0 ± 0.27
		90	131.5 ± 0.36	19,687.3 ± 0.79
		85	130.9 ± 0.41	15,891.9 ± 0.72
		78	130.1 ± 0.81	8,995.3 ± 0.276
		74	131.3 ± 0.93	9,421.12 ± 0.34
		70	129.0 ± 0.66	7,980.8 ± 0.72
200	210	120	217.6 ± 4.45	27,482.5 ± 1.43
		100	211.6 ± 1.52	14,715.7 ± 0.56
		90	204.2 ± 5.27	13,814.4 ± 0.73
		87.5	210.7 ± 1.38	12,232.6 ± 0.72
		80	214.2 ± 1.46	9,059.2 ± 0.43
		77.5	212.0 ± 0.94	8,821.1 ± 0.45
		72.5	211.1 ± 2.65	6,781.1 ± 0.61
800	790	240	130.2 ± 0.78	2,012.9 ± 0.56
		230	124.8 ± 0.51	1,906.0 ± 0.42
		220	125.6 ± 1.25	1,883.3 ± 4.28
		210	126.4 ± 0.83	1,446.5 ± 0.40
		200	125.8 ± 1.85	1,267.2 ± 0.40
		190	128.8 ± 2.22	1,196.8 ± 2.78

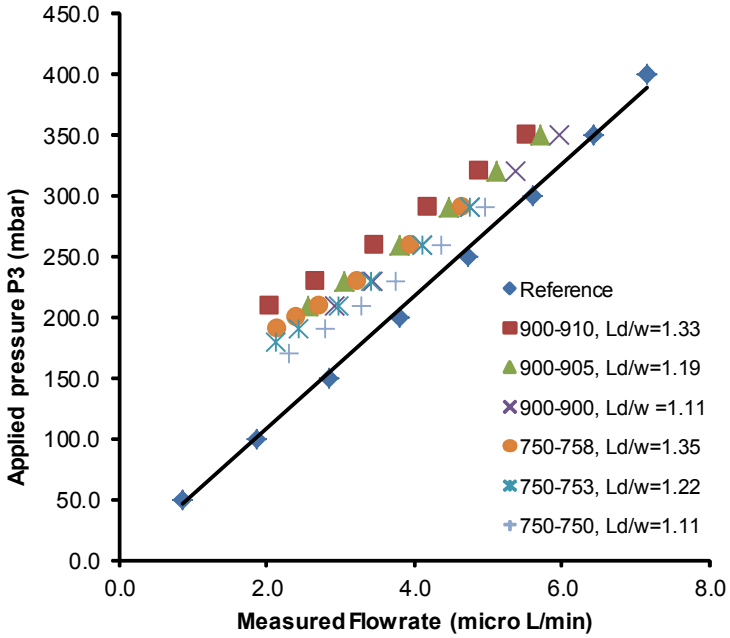

Figure 6.3: The results of the change in measured flow rate against applied pressure at the third junction P3 (at dilution stream) for different experimental conditions. The experiments are either with or without droplets for the fluid combination of hexadecane with 1% Span 80 as the continuous phase and water as the dispersed phase. The reference condition is for the condition without droplets and was used for the calibration. The other conditions indicate the applied pressures at the first and second junctions P1 and P2 according to this format: *(symbol P1-P2, Ld/w)*.

shown in Figure 6.4 where the number of droplets in the test section are plotted with respect to the measured flow rate.

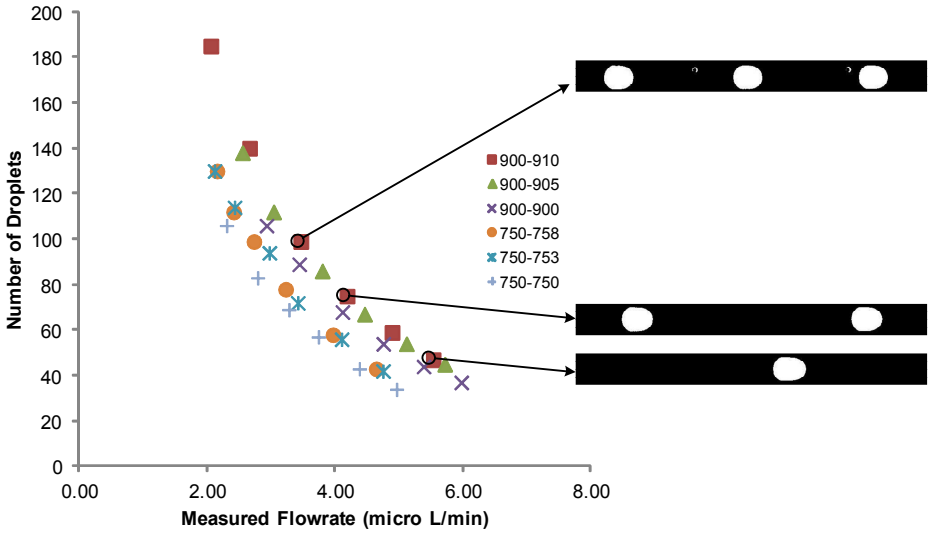

Figure 6.4: The number of droplets in the test area versus the measured flow rate for different experimental settings of hexadecane with 1% Span 80 and water. The experimental conditions for the droplet generation at the first and second inlets (P1 and P3) are indicated in the figure and correspond to the experiments presented in Figure 6.3. Snapshot images from the recorded videos for one experiment with different droplet spacing are shown in the figure.

6.1.3 Video Analysis

Analysis of the recorded video files were done with several steps. First the files were converted from (.cine) format to multi-frame tagged image format (.tif) with an open-source software ImageJ [151]. Image filters were applied to clearly identify the droplets from the video. Afterwards the images were converted to binary images. The binary files were then analyzed with an in house written Matlab program (Mathworks) [152]. The two important parameters that must be included in the Matlab program were: magnification of the microscope objective and frame rate of

the recorded video. The outcome of the Matlab program were: speed of droplet (u_d), spacing between droplets (λ), area of droplet (A_d), length of droplet (L_d), width of droplet (w_d), and frequency of droplets (f). The standard deviation was calculated for each parameter that was found in the program. The analysis was performed for the two channel streams, entering and leaving the area of study seen clearly in Figure 6.2. This step assured that there was no external disturbance in the flow during an experiment, such as presence of particles. The flowchart of the procedures for conditioning the recorded video files and performing the analysis with typical images are presented in Figure 6.5.

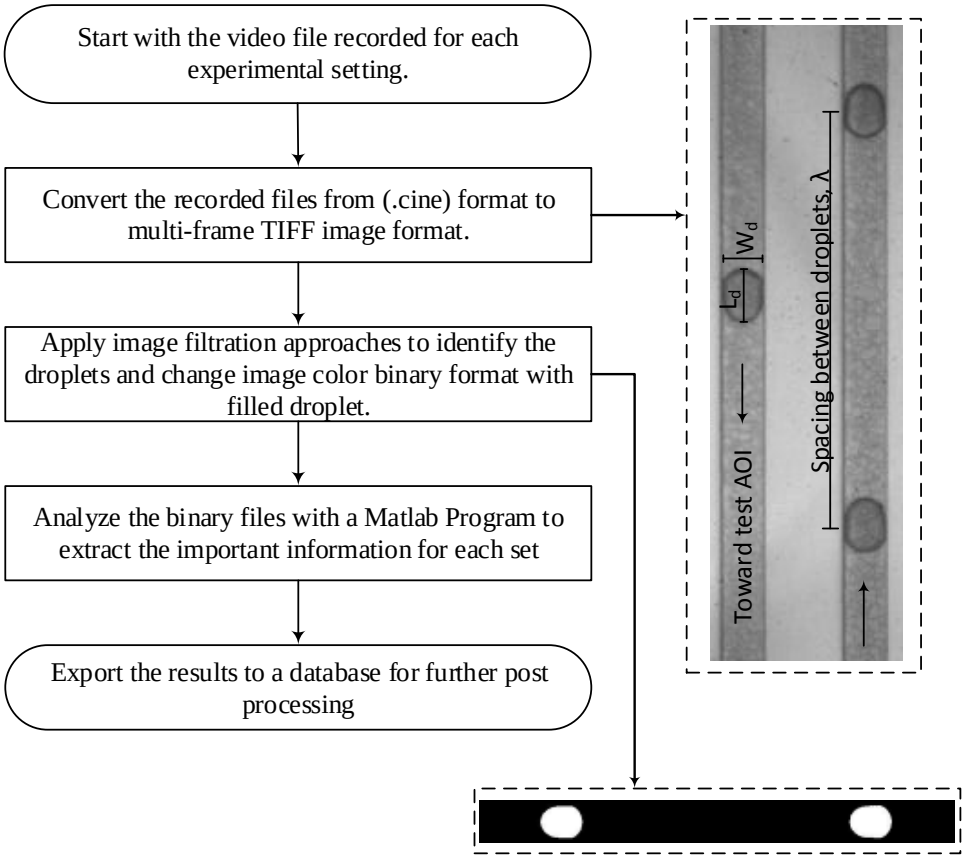

Figure 6.5: A flowchart of the procedure used to analyze the video files that were recorded during the droplet transport studies.

The output from the Matlab program was used with the experiment parameters (i.e. applied pressures P, measured flow rate Q, and reference hydrodynamic resistance $R_{hyd,Ref}$) to find the transport properties of droplets (i.e. excess pressure, the hydrodynamic resistance of the droplets). The results were then filtered to eliminate experimental conditions with large uncertainties or non-realistic values. The filtering conditions that were applied to the final results were:

- $Q_{measured} > 0.8\ \mu l/min.$
- Droplet slip factor ($\beta = \frac{u_d}{u_t}$) > 0.8.
- $n_d > 5$.
- $\Delta P_{drop} > 0$.
- Measured $R_{hyd,Ref}$ within 10% of calculated R_{hyd} for a straight channel found from Equation 3.2.

6.1.4 Table of Experimental Variables

In this work the effects of viscosity ratio and the presence of surfactant in either the dispersed or continuous phase on the hydrodynamic properties of droplets were examined. These factors were studied by changing the liquid/liquid combinations at different experimental sets. The different liquid/liquid combinations studied were:

Combination 1: hexadecane as continuous phase and water, and 10% (V/V) blue food dye as the dispersed phase.

Combination 2: hexadecane as continuous phase and water, 10% (V/V) blue food dye, and 0.2% Tween 20 (w/w) as the dispersed phase.

Combination 3: hexadecane with 1% (w/w) Span 80 as continuous phase and water, and 10% (V/V) blue food dye as the dispersed phase.

Combination 4: hexadecane as continuous phase and water, 37.2 % (w/w) glycerol, and 10% (V/V) blue food dye as the dispersed phase.

Combination 5: hexadecane as continuous phase and water, 37.2 % (w/w) glycerol, 10% (V/V) blue food dye, and 2% Tween 20 (w/w) as the dispersed phase.

Combination 6: hexadecane as continuous phase and water, 37.2 % (w/w) glycerol, 10% (V/V) blue food dye, and 0.0004% Tween 20 as the dispersed phase.

The hydrodynamic results for a certain fluid combination were compared to another fluid combination to examine the effects of the various fluid parameters. Various comparison conditions for the different combinations are presented in Table 6.2.

Table 6.2: The various comparisons that could be performed for the different fluid combinations tested in this work. This table was developed during the design of experiments stage in the early stages of the project. NA is given for comparisons that will not lead to informative direct relations between changed variables.

	Combination 1	Combination 2	Combination 3	Combination 4	Combination 5	Combination 6
Combination 1		Surfactant in dispersed phase above CMC	Surfactant in continuous phase above CMC	Viscosity	NA	NA
Combination 2			Phase that contains surfactant	NA	Viscosity effect in presence of surfactant	NA
Combination 3				NA	NA	NA
Combination 4					Surfactant in dispersed phase above CMC	Surfactant in dispersed phase below CMC
Combination 5						Surfactant concentration
Combination 6						

6.2 Experimental Results

In order to accept the outcomes of the current experimental measurements of the hydrodynamic properties of droplet transport in rectangular microchannels it is important to verify the validity of the measurement approach. This can be achieved by examining measurements of certain flow variables and compare their results to expected flow trends. One measured variable that gave confidence in the experimental approach was the P and Q relation of the reference condition. This relation showed a linear relation with an R^2 close to 1, as shown in Figure 6.3. Moreover, the estimated value of the hydrodynamic resistance ($R_{hyd,ref}$) from the reference line was within 5% of the theoretically calculated hydrodynamic resistance from Equation 3.2 for most experiments.

Other droplets flow parameters also could be used to examine the soundness of the experimental approach by observing changes in a property with the flow condition and compare them to an expected behavior. A property that can be used to validate the experimental approach is the hydrodynamic resistance of droplets. It is known that the hydrodynamic resistance is affected by the geometrical properties of liquid droplets. With the increase of the droplet length the hydrodynamic resistance should increase. Typical outcomes of the change of the hydrodynamic resistance of liquid droplets is with length of droplet (L_d) for two examined fluid combinations are presented in Figure 6.6 .

From Figure 6.6 it is clear that the hydrodynamic resistance of droplets will change with the length of the droplet for the two fluid combinations that were shown. An increase of $R_{hyd,drop}$ was observed with the increase of L_d for all tested fluid combinations. It should be noted that the relation between the length of droplet and hydrodynamic resistance was not linear and could not be fitted to an equation from the data presented. The reason is that hydrodynamic resistance of droplets is affected by other parameters that are not included in the plot, such as Ca, speed of droplet, and the confinement condition. To illustrate these complex relations the data points in Figure 6.6 were given a contour color according to the droplet velocity. The results discussed above indicate that the experimental approach agrees with the expected

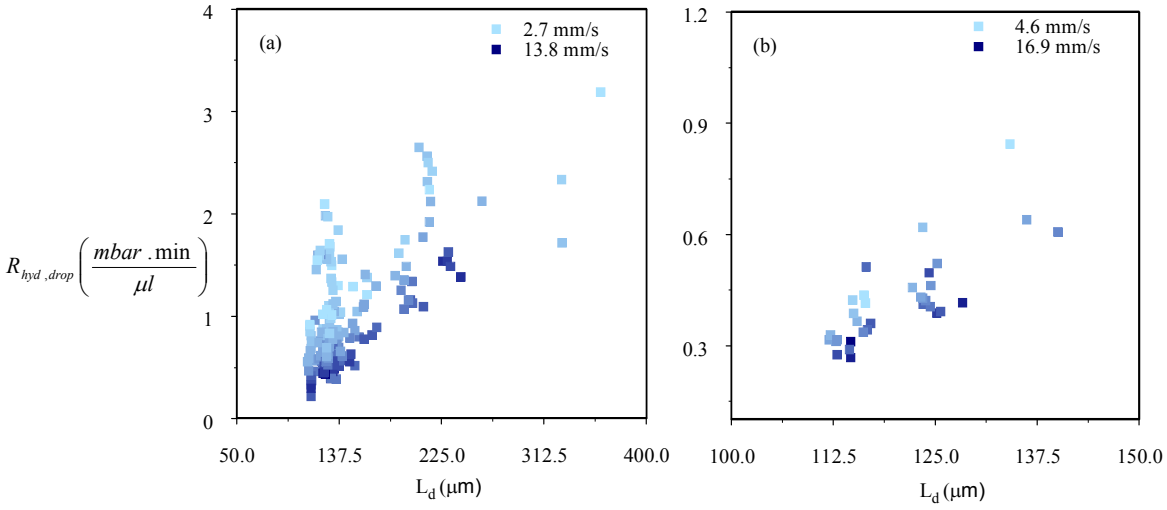

Figure 6.6: The relationship between the measured droplet hydrodynamic resistance ($R_{hyd,drop}$) with the length of droplet (L_d) for experiments: hexadecane with water (**Combination 1**) and hexadecane water-glycerol mixture (**Combination 4**). The figures are as follows: (a) $R_{hyd,drop}$ versus L_d for hexadecane/water, and (b) $R_{hyd,drop}$ versus L_d for hexadecane/water-glycerol. The data points were given a contour color according to the measured velocity of the droplets. The maximum and minimum velocities are presented in the upper corner of the plots.

flow properties. Thus, there is confidence in the results that will be discussed later.

One flow property that is commonly used to describe droplet hydrodynamic properties in microchannels is the measured excess pressure of droplets (ΔP_{drop}) [6, 62, 72]. This property is another form of the flow resistance and it is easier to comprehend when explaining the hydrodynamics of droplets. This property was calculated by dividing the outcome of Equation 6.10 with the n_d. The relation between the droplet length and droplet pressure drop is plotted in Figure 6.7.

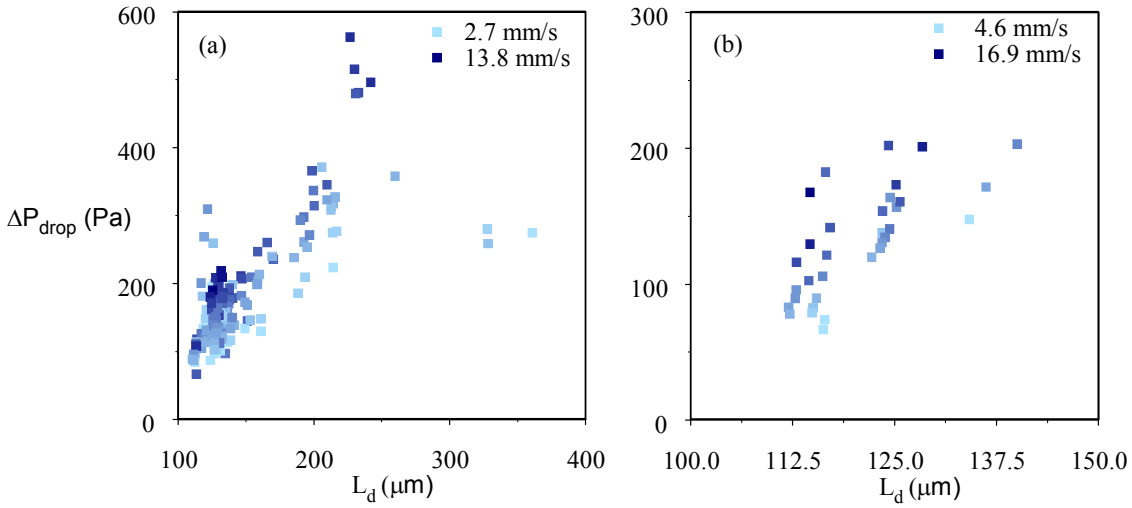

Figure 6.7: The pressure drop per droplet (ΔP_{drop}) versus the length of droplet (L_d) for hexadecane/water (**Combination 1**) and hexadecane/water-glycerol mixture (**Combination 4**). The figures are as follows: (a) ΔP_{drop} vs L_d for hexadecane/water, and (b) ΔP_{drop} vs L_d for hexadecane/water-glycerol. The data points were given a contour color according to the measured velocity of the droplets. The maximum and minimum velocities are presented in the upper corner of the plots.

As it was expected the pressure drop, or excess pressure, for droplets increased with the length of the droplet, observed clearly in Figure 6.7. This finding indicates that the required pressure to push the droplet in the microchannel increases with length. The data points in Figure 6.7 were also given a contour color according to

their measured droplet velocity (u_d) where the upper and lower limits are indicated in each figure. This contour coloring scheme was included to illustrate that other flow parameters have an effect on the measured droplet pressure.

6.2.1 Capillary Number (Ca) and ΔP_{drop}

It was previously mentioned that the excess pressure across a droplet is a function of the length of droplet, the interface pressure jump at the leading and trailing edges, and the pressure drop in the gutter regions of the continuous phase. From these three contributors the variable that is directly influenced by the Ca is the Laplace pressure jump at the curved interface. The flow in the gutter regions is also affected by Ca since the thickness of the gutter regions is a function of Ca [4, 42, 153]. However, since the droplet size is much larger than that of the gutter regions it is expected that the effect of Ca is more prominent on the droplet phase.

For flowing gas/liquid systems the pressure drop across a curved interface is estimated from the Bretherton equation (Equation 2.12) [4]. Bretherton [4] found that the excess pressure of bubbles were a function of Ca. His findings were accepted by researchers and have been used to estimate the pressure drop of bubbles [62]. Furthermore, in liquid/liquid systems the Bretherton estimation of excess pressure had been used and well accepted to estimate the pressure jump at curved liquid/liquid interfaces, especially for flow in capillaries [38, 52, 123].

From the current experimental work the change of pressure drop across a droplet with Ca was examined for all tested fluid combinations. The results for combination 1 (hexadecane and water with 10 % food dye) are presented in Figure 6.8.

It is clear from Figure 6.8 that pressure drop will increase with Ca. This increase in the pressure drop is affected by the length of droplet where for longer droplets the nature of change with Ca is higher with a different trend. This trend was identified since the droplet lengths were given a contour color based on their length in Figure 6.8.

This relation between the droplets pressure drop and Ca for small droplets in rectangular microchannels was proven in the current experiments and contradictory

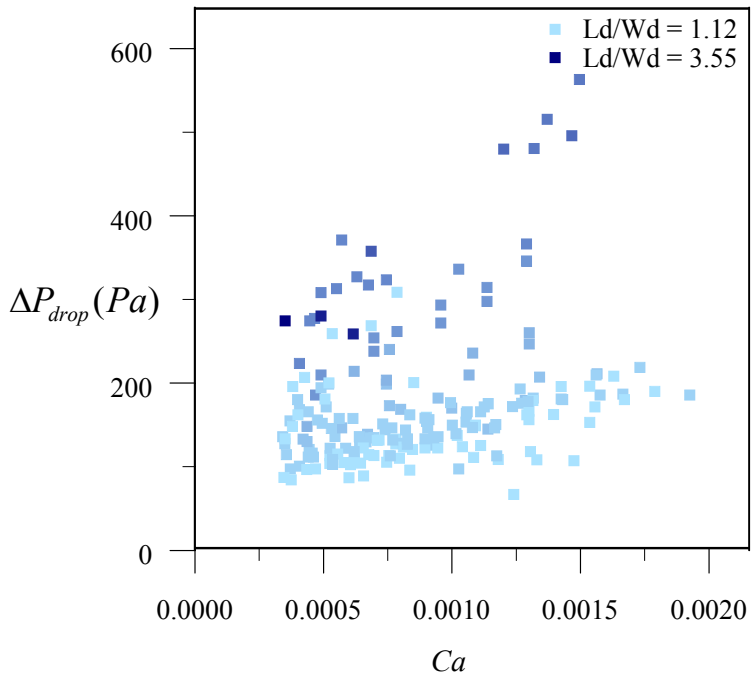

Figure 6.8: The measured pressure drop across a droplet versus Ca for water-dye experiments (**Combination 1**). The data points were given a contour color according to the measured droplet length L_d.

to other published work. From the literature Vanapalli *et al.* [6] indicated that the pressure drop of small droplets was not a function of Ca for the sizes that they measured $\left(1.5 \leq \frac{L_d}{w_c} \leq 4.9\right)$. The results presented in Figure 6.8 contradict what Vanapalli *et al.* [6] reported. However, it should be pointed out that most droplet sizes that Vanapalli [6] presented did not match the majority of droplet sizes that were measured in the current work $\left(1.05 \leq \frac{L_d}{w_c} \leq 3.5\right)$. Even for the droplets lengths that matched Vanapalli *et al.* [6] the trend observed in the current work indicated that there is a relation with Ca. The reasons for the discrepancies with Vanapalli *et al.* [6] are unknown. However, the approach that Vanapalli *et al.* [6] used to measure the pressure drop and the channel material is different from the current work and may cause these differences.

6.2.2 Viscosity and ΔP_{drop}

One contributing factor to the droplet resistance is the viscosity of the dispersed phase. It has been reported that viscosity ratios below 1 will not have an effect on the droplet resistance [137]. In the current work the viscosity ratio was altered by adding glycerol to the dispersed phase (see Table 3.3). The two viscosity ratios that were examined were 1:3.4 and 1:1 (water to hexadecane). Furthermore, due to the different fluid combinations that were studied in this work (Table 6.2) there are two viscosity conditions that were examined: without surfactants and with surfactants. Figure 6.9 presents the results of pressure drop per drop versus the Ca for viscosity ratio without surfactant.

It is clear from Figure 6.9 that the excess pressure of the high viscosity droplets was very close to the condition of the less viscous droplets for the fluids combinations without surfactant. The slightly lower pressure drop for viscous droplets was within the uncertainty of the measurement approach (see Appendix C.3). This result is consistent with what is reported in the literature for droplets with viscosity ratios below 1 [137].

The other examined viscosity ratio comparison was the effect of viscosity in the presence of surfactant above the CMC concentration. The results of fluids **Com-**

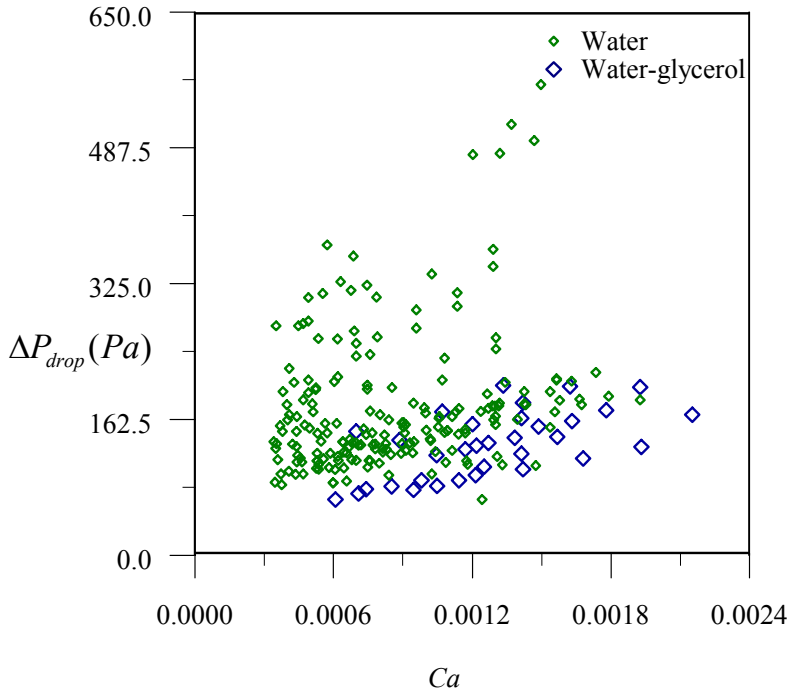

Figure 6.9: The droplets pressure drop against Ca for viscosity contrast conditions of fluid combinations without surfactants. The small green squares are for water droplets (**Combination 1**), and large blue squares are for water-glycerol mixture (**Combination 4**).

bination 2 were compared to fluids **Combination 5** to examine this effect. The comparison is plotted in Figure 6.10.

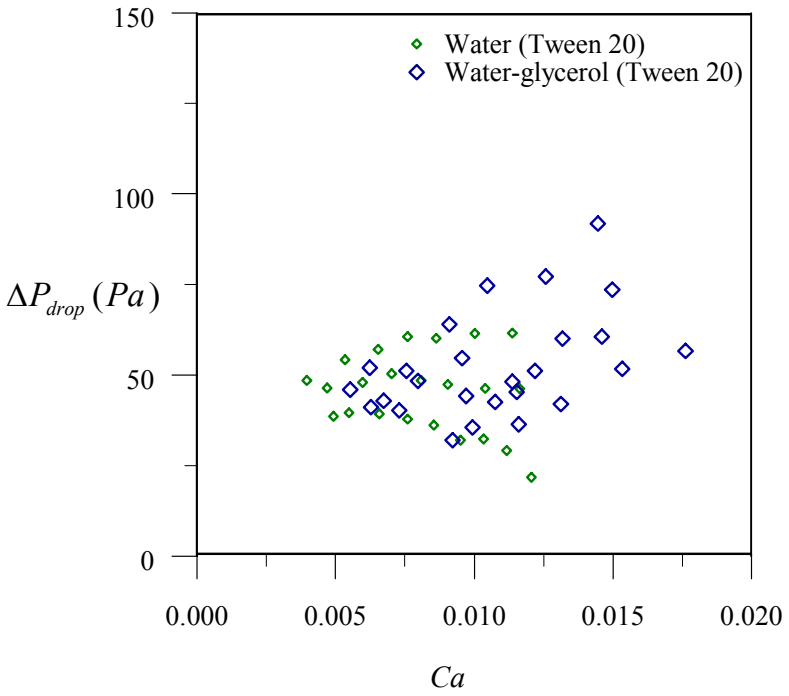

Figure 6.10: The droplet pressure drop against Ca for viscosity ratio condition for fluid combinations with surfactant above the CMC concentration. The small green squares are for water droplets (**Combination 2**), and large blue squares are of water-glycerol mixture (**Combination 5**).

From Figure 6.10 it is clear that the trends for the pressure drop of droplets in the presence of surfactants in the dispersed phase are similar to what were observed in the absence of surfactants. The measured pressure of droplets had close values for the viscosity ratio that was examined.

The results shown in Figures 6.9, and 6.10 indicates that the viscosity ratio of 1 and below did not have an effect on the droplets pressure drop for the droplet sizes that were examined. This indicated that the pressure drop is dominated by the confinement condition of the droplets inside the channel rather than the viscosity

contribution of the droplets liquid phase.

6.2.3 Surfactants and ΔP_{drop}

In this work the examination of the presence of surfactants on the hydrodynamic properties of droplets was performed for two general conditions: the phase that contains the surfactant, and the concentration of the surfactant. Examining the effect of the phase that contains the surfactant was done to water based solutions without glycerol to avoid the contribution of viscosity ratio, if it existed. The two fluid combinations that were examined were: water with 0.2% Tween 20 as the dispersed phase and pure hexadecane as the continuous phase (**Combination 2**), and water as the dispersed phase and hexadecane with 1% Span 80 as the continuous phase (**Combination 3**). Figure 6.11 presents the results for the effect of the surfactant phase on the measured pressure drop of droplets along with the condition without surfactants for comparison.

From Figure 6.11 it is clear that the phase that contains the surfactant has an effect on the pressure drop of the droplet. The condition that showed the lowest pressure drop across the interface was when the surfactant is in the continuous phase (gray squares). The condition where the surfactant is present in the dispersed phase had a pressure drop higher than that of the surfactant in the continuous phase for the short region where the Ca were matched. This finding indicates that the phase containing the surfactant might have an effect on the pressure drop across the droplet. Another explanation for these results is that the surface coverage on the liquid/liquid interface is affected by both the type and phase that carries the surfactant. This difference is due to the nature of the surfactant transport between the formed micelles and the interface under convective motion [70, 77]. This explanation is supported by the fact that Span 80 is a smaller molecule than the Tween 20. Moreover, the reduction in the interfacial tension when using Span 80 was higher than Tween 20 for concentrations above CMC (see Table 3.3).

The other examination of the effect of surfactant on the pressure drop was done by examining the effect of having a surfactant above and below the CMC concentration.

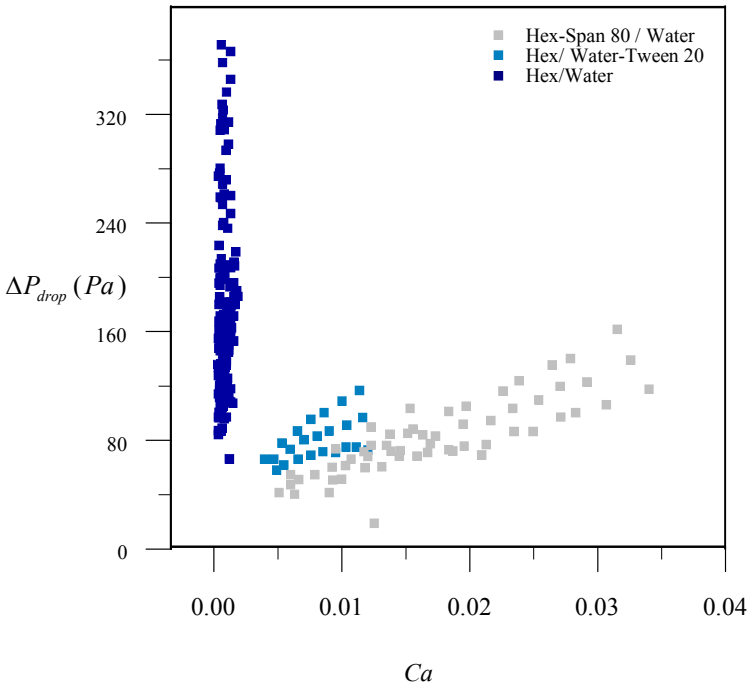

Figure 6.11: The effect of the type of surfactant and the phase that carries it on the pressure drop across a droplet. The dark blue squares are for the condition without surfactant (**Combination 1**), light blue is for the condition of surfactant in the dispersed phase (**Combination 2**), and gray squares are for the condition with the surfactant in the continuous phase (**Combination 3**).

These experiments were carried with water-glycerol mixtures and hexadecane. The surfactant that was used was Tween 20 since it is commonly used in microfluidics systems [62, 71]. Figure 6.12 presents the results for the pressure drop in the presence of different concentration of surfactants.

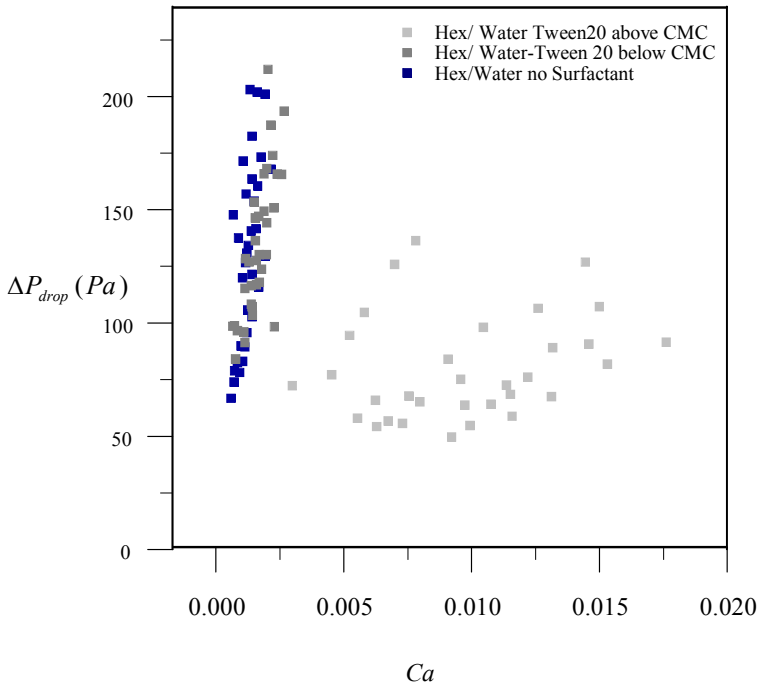

Figure 6.12: The pressure drop of droplets versus Ca for different concentrations of surfactant in the dispersed phase. The dark blue squares are for the condition without surfactant (**Combination 4**), dark gray is for the condition with a surfactant in the dispersed phase below CMC (**Combination 6**), and light gray squares are for the condition with a surfactant in the dispersed phase above CMC (**Combination 5**).

From Figure 6.12 it is noticed that the concentration of surfactant above CMC had an effect on the droplet pressure drop compared to the conditions of below CMC and no surfactant. The condition above CMC generally had lower pressure drop compared to the other conditions. For the condition where the surfactant was below CMC concentration the presence of the surfactant did not have an effect on

the pressure drop. This was observed since the measured droplet pressure drop for that condition was close to the values of the condition without a surfactant. These results are interesting since it was expected that for the condition with a surfactant concentration below the CMC the pressure drop should be lower than that of the condition without a surfactant. This finding indicates that for confined droplets of fluids with surfactant below the CMC concentration the pressure drop does not change from the condition of the absence of surfactants

6.2.4 Droplet Slip Factor

An interesting property for segmented liquid flows is the speed of the segments compared to the average velocity inside the capillary or channel. This property is called the slip factor and is giving the Greek letter β by researchers in the Microfluidics community. The slip factor is calculated by:

$$\beta = \frac{u_d}{u_t} \tag{6.11}$$

where u_d is the velocity of the droplet, and u_t is the average velocity of the flow. In the literature it had been proven, and accepted, that the slip factor of fluid segments in circular capillaries is higher than 1, meaning that the droplet speeds up more than the average velocity of the flow in the capillary. This condition of droplet speed can be explained by taking a closer look at the transport of segments in capillaries. Physically, the fluid segment is separated from the wall by a thin film of the continuous phase. Thus, the bulk area of the droplet is subjected to the two dimensional velocity profile of the continuous phase located mainly in the middle of the capillary. For circular capillaries the velocity profile is high at the middle and decreases closer to the walls reaching a minimum of zero due to the no-slip condition. This condition makes segments move faster than the carrier phase. Due to slipping of the segment faster than the carrier phase the leaky piston analogy was given to segmented flow in capillaries [38, 4].

The transport of liquid droplets in microchannels shares some similarities with segmented fluid flow in capillaries, as was discussed earlier in Chapter 2. The con-

dition of fluid encapsulation, the lubrication regions, and the shape of leading and trailing edges are some of the likenesses of flows in microchannels compared to flow in capillaries. For those reasons researchers try to find resemblances between flow in microchannels with flow in capillaries including the droplet slip (β). From the literature of segmented flow in microchannels the droplet slip was reported to be higher than unity ($\beta > 1$) similar to the droplet slip in capillaries [6, 38, 72]. However, it is important to mention that values of β varied in the published literature. For example Vanapalli *et al.* [6] found that $\beta = 1.6$ for water droplets in mineral oil. The channel material that was used by Vanapallli was PDMS. Other researchers also reported that the slip factor for droplets is above 1 [28, 54, 38, 72].

In the current work the droplet slip β was calculated by finding the droplet speed from the recorded video file at the area of interest and dividing it by the calculated average velocity of the continuous phase from the measured flow rate. Typical results for the droplet slip for the hexadecane/water experiment are presented in Figure 6.13.

From Figure 6.13 it is clear that the droplet slip is below 1 in most cases for rectangular microchannels. The flow condition that showed higher slip factor β was bounded by a maximum $Ca < 7 \times 10^{-3}$. Other tested fluid combinations showed a slip factor below 1. Having a slip factor below 1 indicates that the flow in the gutter regions is faster than of the speed of droplet leading to the continuous phase speeding up in front of the droplet.

The current findings for the droplet slip factor in rectangular microchannels contradict with what is commonly presented in the literature about droplet migration in rectangular microchannels. However, it is important to mention that the experimental conditions differ between this work and other work presented in the literature. For instance, most of the work that reported droplet slip above 1 uses PDMS as the channel substrate material. As it is well known and accepted in the literature PDMS swells with most organic solvents [6, 7, 72]. This swelling of PDMS has an impact on the final shape and cross sectional area of the microchannel and the nature of confinement of liquid droplets. The change of the cross section of a microchannel will have consequences on the bulk flow conditions, the resistance in the microchannel and the nature of the flow in the gutter regions.

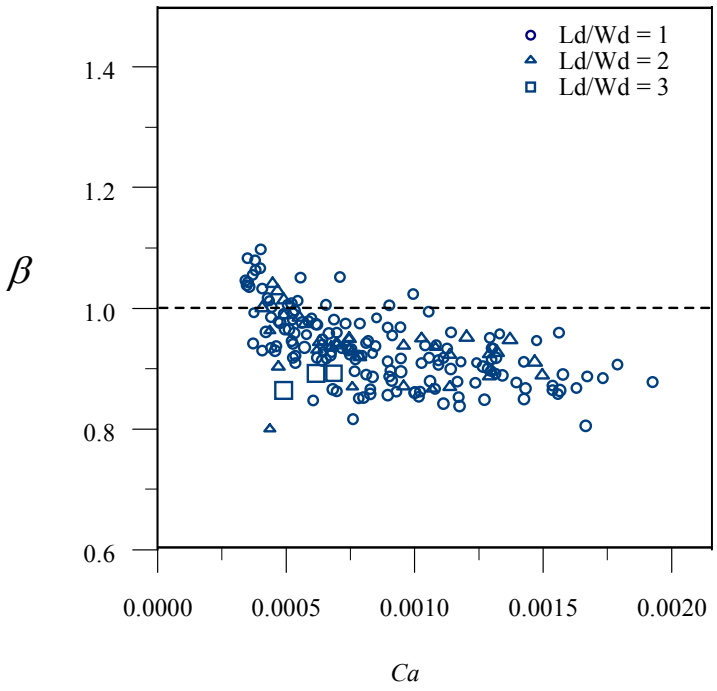

Figure 6.13: The droplet slip factor (β) against Ca for the experiments of water with hexadecane without surfactants. The data points were categorized by the ranges of droplet non-dimensional length.

But to what degree does the swelling of a channel affect its geometry in PDMS microchannels? This is a difficult question to answer since there isn't an easy way to examine what is actually happening in the microchannel when it is swollen. From the literature Dangla *et al.* [7] examined the swelling of PDMS by optically recording changes in patterns on the glass substrate of a PDMS microchannel when it swelled and compared them to the non-swollen condition. Figure 6.14 presents a schematic of their approach with a profile of a representative pattern line during the swelling process. They reported that the PDMS swelling depends on the type of solvent used. Also, PDMS swelling could be severe to a degree that it affects the shape of droplets as they are transported in a swollen microchannel. It should be noted that in their work Dangla *et al.* [7] have used extreme geometrical conditions (very low aspect ratio $\frac{h}{w_c}$) of a microchannel geometry where the channel was very wide compared to its height (see Figure 6.14).

In the current work, an attempt to examine the swelling of a PDMS microchannel with a thin slice approach bonded to a glass slide was performed. Details about this attempt and the results are presented in Appendix B. The final conclusion was that for the aspect ratios that were examined the swelling of PDMS could reach up to 8% of the channel dimension. The effect of the swelling on single phase flow was also numerically examined in Section B.2 by taking the results from swelling experiments. The numerical simulation results presented in Section B.2 indicated that the swelling of channels will have an effect on the velocity profile in a single phase microchannel and magnitude of the maximum velocity. By extending the finding of the simulation results to the transport of droplets it is believed that swelling will also impact the droplet speed and hence droplet slip. Thus, experimental results that report droplet slip above 1 for experiments performed in channels that swell must be used with caution.

The above arguments were presented to point out the errors that could be present when evaluating the slip of droplets reported in the literature. The current results of droplet slip factor below 1 agreed with some of the presented work in the literature. This condition had been reported in the literature, in fewer occasions, for gas segments [62, 154] or liquid droplets [155]. From numerical simulations Wong *et al.* [154]

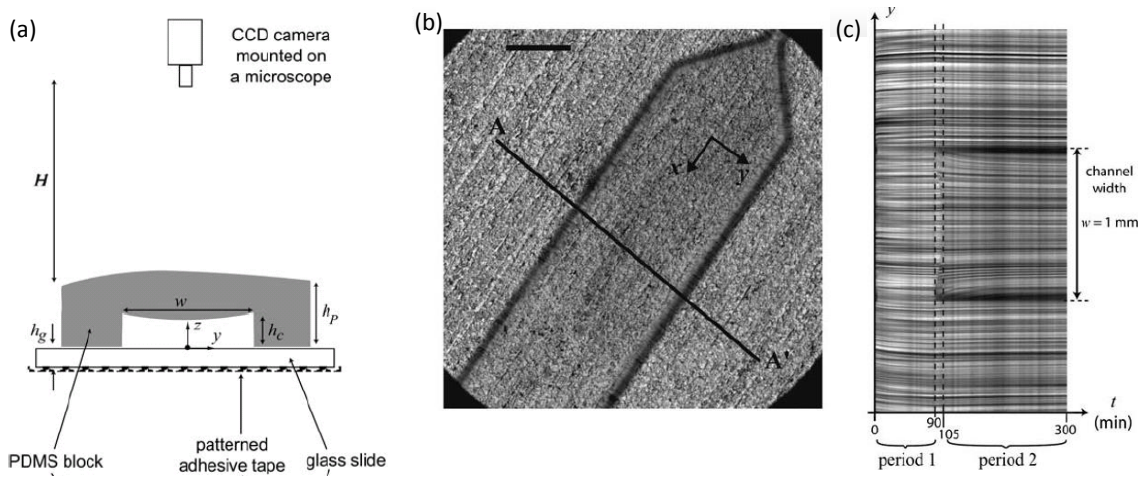

Figure 6.14: Images of the approach used by Dangla *et al.* [7] to examine the swelling of PDMS when exposed to solvents. Figure (a) A schematic of the approach used, (b) A top view image recorded by the camera for the patterns, and (c) A profile for the change in image patterns along a line after swelling. Images were acquired from Dangla *et al.* [7]. Included with permission (Copyright, Royal Society of Chemistry).

anticipated that the continuous phase will speed up across the droplet at very low *Ca*. Experimentally, Fuerstman *et al.* [62] found that the bubble slip in rectangular microchannels under certain conditions was below 1. The conditions that they observed were when using surfactants in their studies. For liquid/liquid systems in rectangular PC microchannels Jakiela *et al.* [155] reported that the droplet slip can be less than for large droplets. Also, the high viscosity ratio between the droplet phase and the continuous phase had an effect on the slip speed of droplets.

6.2.5 Effect of Droplets Spacing

One parameter that may have an effect on the hydrodynamic resistance for a train of droplets in a microchannel is the spacing between droplets (λ). Under certain conditions a droplet could be influenced by the relative fluid motion between two consecutive droplets leading to an apparent decrease in the hydrodynamic resistance of the droplet. This phenomenon is also referred to as entrainment [156]. An example of this phenomenon was presented by Labort *et al.* [137] where they found that at a certain distance, ($6\ mm$) in their experiments, there exist a collaborative effect from pairs of droplets leading to a decrease in the measured droplet resistance compared to other conditions. However, it was difficult for Labort *et al.* [137] to isolate the entrainment contribution to the droplet resistance since other parameters that had an impact on the droplets resistance were present due to their experimental approach.

The microchannel network design and experimental approach that were used in the current study allowed for examining the effect of droplet spacing, up to a certain extent. The experimental procedure involved changing the sets of pressures at the microchannel network ports (P1, P2 and, P3). The changes were done to control the droplet sizes, spacing, and speed (see Table 6.1). Thus, potentially the effect of spacing on the pressure drop could be found.

In order to sense the effect of droplet spacing (λ) it should have a non-dimensional form by a geometrical length. The length of droplet L_d, the height of channel h, or the width of channel w_c are geometrical properties that could be used to have a dimensionless droplet spacing number. In the current work, the channel width was

chosen as a parameter to non-dimensionalize the spacing. The effects of droplet spacing on the measured pressure drop for **Combination 1** of fluids are presented in Figure 6.15.

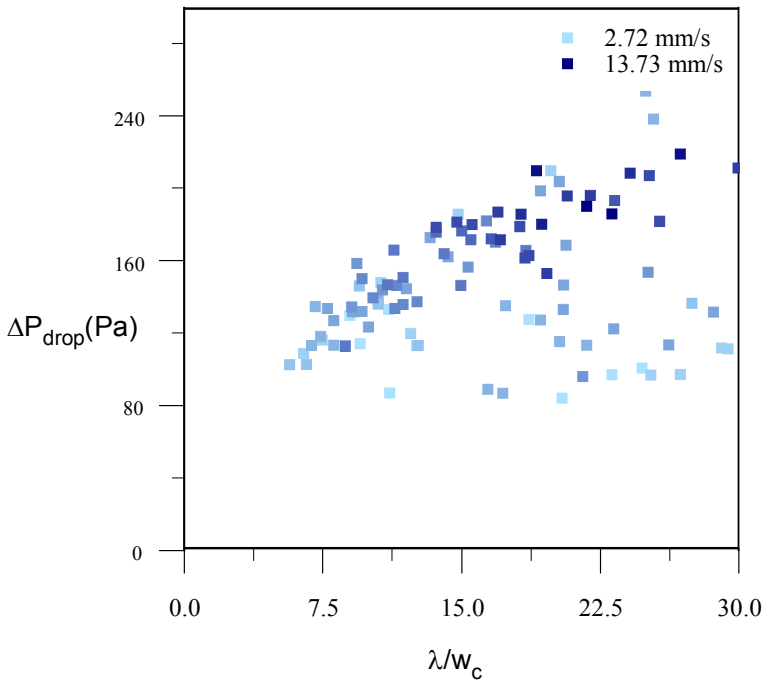

Figure 6.15: The effect of the non-dimensional droplet spacing $\frac{\lambda}{w_c}$ on the measured pressure drop in a rectangular microchannel. The measured pressure drops were given a contour color based on the droplet velocity. The legend shows the two extreme velocity conditions.

The results plotted in Figure 6.15 were limited to a spacing ratio of 30 ($\lambda/w_c \leq 30$). This was done since it was expected that at higher spacing to width ratios the effect of the entertainment will be reduced. From a first look of the results of Figure 6.15 the effect of spacing on the pressure drop is not clear. This is due to the fact that there are other contributors to the pressure drop that could not be isolated.

Several attempts were done to filter the data according to the droplet length L_d,

Ca, and droplet speed u_d since these parameters had an effect on droplet pressure drop (ΔP_{drop}). Most attempts for filtering the spacing data resulted in reducing the number of data points and not providing substantial information to support the hypothesis that entertainment had an effect on ΔP_{drop}. However, an approach that could be done to modify the results is to combine variables and compare them with ΔP_{drop}. Several attempts to combine parameters with (λ/w_c) were performed and the variable that showed interesting patterns was Ca with non-dimensional spacing. The new combined non-dimensional number was the result of multiplying (λ/w_c) with Ca giving a value of $\left(\frac{\lambda}{w_c} \cdot Ca\right)$. The pressure drop ΔP_{drop} of droplets presented in Figure 6.15 with the new non-dimensional number is presented in Figure 6.16.

A close look at Figures 6.16 indicate that there might be a relation between the measured pressure drop of a droplet and the non-dimensional group of $\left(\frac{\lambda}{w_c} \cdot Ca\right)$. The relation is identified since the droplet pressure drop obeys a certain pattern with the velocity along the abscissa of Figure 6.16. If the abscissa was below 5×10^{-5} the measured pressure drop of droplets (ΔP_{drop}) does not correlate with the droplet velocity. By contrast, for values higher than 5×10^{-5} on the x-axis the measured pressure drop correlates well with the velocity of the droplet. This was clear since it was noticed at certain locations of $\frac{\lambda}{w_c} \cdot Ca$ and as velocity increases (indicated by the contour contrast of the points) ΔP_{drop} increases.

Although the current experimental results did not isolate the effect of spacing between pairs of droplets (λ) on the hydrodynamic properties of droplets, it showed that it might be present under certain conditions. Unfortunately, due to the pressure control system limitations (maximum pressure 1 bar) and channel design aspects (total length of test section) an extensive study of experimental conditions could not been done to find and isolate the effect of droplet spacing in the absence of other contributing factors (Ca, u_d, and L_d). This phenomenon is open for future research.

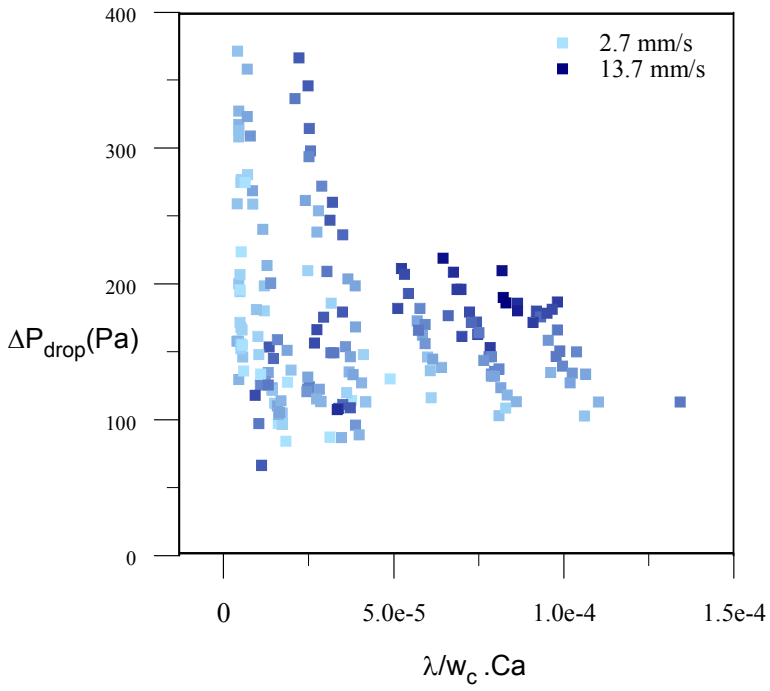

Figure 6.16: The effect of the non-dimensional droplet spacing and Ca ($\frac{\lambda}{w_c} \cdot Ca$) on the measured droplet pressure drop (ΔP_{drop}). The measured pressure drop were given a contour color based on the droplet velocity. The legend indicates the two extreme velocities of droplets.

6.3 Discussion

First it is important to mention that early stages of this project were performed with PDMS microchannels with a similar design to the one used in the current work. However, the experimental results found from measuring the hydrodynamic properties of droplets in PDMS microchannels were inconsistent and gave unrealistic values, such as negative ΔP for droplets. The conducted experimental attempts with PDMS microchannels and their observations were not reported in the current thesis, but they must be acknowledged.

The current experimental work for examining the hydrodynamic resistance of droplets in microchannels utilized an indirect approach to find changes in flow properties during the presence of identical droplets. The channel material, the methodology, and the measurement apparatus are factors that can give confidence in the experimental results. A parameter that gave confidence in the channel material was the reference hydrodynamic resistance ($R_{hyd,Ref}$) that was calculated from the applied pressure (P) and measured flow rate (Q) relation for the test section in the absence of droplets. The P and Q relation showed a linear trend, as was discussed earlier (see Figure 6.3). This finding proved that the chosen channel material and experimental systems used were reliable. It is important to mention that published experimental work with PDMS did not show the linear relation between P and Q for single phase flow [25, 72]. This leads to the conclusion that PC is superior to PDMS for hydrodynamic studies in long channels. Adding to that, the measured value of $R_{hyd,ref}$ was within 5% of the calculated value of the test channel with Equation 3.2.

After assuring that the microchannel material, network, and measurement approach were suited to droplet hydrodynamic studies investigations were carried for different fluid combinations and various flow conditions. The experimental results indicate that the measured pressure drop ΔP_{drop} of the droplet was a function of the length of the droplet L_d and Ca for the droplet sizes that were measured. Also, the viscosity ratio of 1 and below did not have an impact on the pressure drop of droplets.

Among the interesting investigations of the current work was the examination of

the effect of surfactant on the droplets pressure drop. It is known that the presence of surfactants lowers the interfacial properties between the droplet and the continuous phase. One expected outcome was that the pressure drop from the curved interface will be reduced. This was proven to be correct for the condition of having surfactants above the CMC concentration. For the other condition of examining the surfactant below the CMC concentration the presence of surfactant did not have an effect on the droplet pressure drop. It was expected that for that condition, below CMC surfactant concentration, that Marangoni stress is present on the liquid/liquid interface. Furthermore, it has been reported that in some situations Marangoni stress may affect segment pressure drop [70, 77, 157]. However, the current findings indicate that is not the case for confined droplet flow in microchannels for the surfactants and fluids that were examined.

Also it was anticipated that the presence of surfactant above the CMC will lead to an increase in viscosity effect of the droplet pressure drop. For this hypothesis to be correct, the condition where the glycerol was added should have had the higher pressure drop than the condition without glycerol. However, the results from Figure 6.10 indicate that for the conditions with surfactant concentration above CMC the viscosity ratio does not influence the droplet pressure drop. From the above discussions it is believed that the pressure drop of small confined droplets in microchannels is a function of the pressure drop at the curved interface and the confinement condition. The viscosity of the droplet phase did not show any impact for the droplet sizes that were examined.

It is important to emphasize that when using surfactants the hydrodynamic properties of long droplets could not be measured. This was due to two factors: droplet generation aspects and the dilution stream splitting of droplets. For droplet generation in a T-junction the use of surfactants lowers the interfacial tension which makes it harder to generate long droplets in a stable manner. Furthermore, the lower interfacial tension lead to less surface tension that causes droplet splitting at the dilution stream. For the channel network design and fluid combinations with surfactants the maximum droplet lengths L_d generated and studied are presented in Table 6.3.

The results of the maximum droplet size that was generated presented in Table 6.3

Table 6.3: The maximum droplet length that was generated and studied in the current work for the fluid combinations that contained surfactants.

Fluid Combination	Maximum droplet length $L_{d,max}$ (μm)
Combination 2	144.9
Combination 3	147.8
Combination 5	154.2
Combination 6	145.1

showed that it was hard to generate droplets with length ($L_d > 160\mu m$) and measure their hydrodynamic properties for fluids that contain surfactants. Although the results did not cover all dimensional aspects of the droplet lengths, the results that were shown confirmed that the droplet pressure drop (ΔP_{drop}) was a function of Ca and L_d.

An interesting finding from the current experimental work was that droplet slip (β) was lower than 1 for most of the experimental conditions that were examined. By knowing that the pressure drop is composed of pressure drop in the dispersed phase and the pressure drop in the gutter region it is hypothesized that the pressure drop at the gutter region is lower than that of the dispersed phase. This will lead to faster flow in the gutter compared to the droplet transport speed. If the condition of the gutter regions are changed, for example longer droplets or using a more viscous continuous phase compared to the droplet phase, the flow in the gutter region relative to the droplet speed may change. Hence, there might be a region at which the droplets slip changes according to the gutter region properties.

It should be emphasized that although all measurements state that the properties are for the droplet (i.e. ΔP_{drop}) it also includes the confinement properties of the gutter regions. The system of the droplet and encapsulating fluid (gutter and lubrication) all contribute to the pressure drop of the droplet. Deciphering the two components, droplet phase and continuous phase, is hard to perform since information about the flow in the gutter regions are unknown, as was discussed in Section 2.4.

To find the pressure drop at the gutter regions one must know the shape, length, the fluid/fluid flow condition, and the flow rate.

6.4 Conclusion

In this work a microchannel network fabricated from PC was used to examine droplet hydrodynamic properties during their transport in a rectangular microchannel. The network was designed to assure stable generation of identical droplets that were uniformly spaced. Changes in the bulk flow conditions at certain pressure settings for an equally spaced train of droplets were used to estimate the hydrodynamic properties of the liquid droplets. Experimental results indicate that the measured droplet pressure drop was a function of Ca and L_d. Furthermore, the presence of surfactants above CMC affected the measured pressure drop of droplets causing a reduction in their values.

Experimental results also indicated that for the studied droplet sizes the speed of the droplet was slower than that of the continuous phase ($\beta < 1$). This indicates that the flow in the gutter regions is faster than the speed of droplets in the microchannel. This finding sheds light on the nature of droplet transport in rectangular microchannels and challenges the misconceived phenomena of droplet slip. Researchers must take into consideration the change of confinement condition present in PDMS microchannels and their effect on the hydrodynamic properties of droplets.

Chapter 7

Final Conclusions and Future Work

In this chapter a summary of the major findings for each project will be briefly discussed. Emphasis will be given to unique results that were found and their implications. Also, the potential future work that could be done and the areas of interest that may require further investigation.

7.1 Main Findings From the Projects

Throughout the experimental investigations that were carried out for droplet generation in T-junction microchannels and droplet transport in rectangular microchannels interesting results were observed. The complexity of the flow patterns at different planes and the changes of droplet transport properties were found at various flow and fluid conditions. The main findings for each project will be visited next.

7.1.1 Major Findings in the μPIV Study

The current μPIV study examined droplet generation in a T-junction for three droplet generation regimes: squeezing, transition, and dripping. This work was the

first to present results of the dripping regime for droplet generation in a T-junction microchannel. This accomplishment was achieved by developing a droplet detection system that was used as an external triggering system for the μPIV system.

This work also compared the effect of absence or presence of a surfactant above CMC on the droplet generation process from a velocity field point of view. The studies focused on the changes of the velocity fields across the height of the microchannel for two stages of droplet generation: the filling stage and the start of pinch off. The major findings of the work can be listed as follows:

- An optical detection based triggering system was developed and integrated with the μPIV system. This optical detection system was fast and allowed the μPIV system to acquire images of different identical droplets at the same stage with an estimated precision of 1 μm.
- Droplet generation in the squeezing and transition regimes share many similarities in the start of pinch-off.
- Droplet pinch-off in the squeezing and transition regimes start for the liquid thread close to the top and bottom walls and propagate toward the middle region of the thread. At these regimes the pinch-off occurs at the T-junction
- The filling stage in the dripping regime showed similar velocity patterns to the transition regimes. However, pinch-off differed from the transition regime.
- Segment pinch-off in the dripping regime occurs downstream of the T-junction. The pinch-off of segments in the dripping regime starts with the thinning of the thread from the top and bottom walls.
- The presence of a surfactant in the droplet phase above the critical micelle concentration (CMC) did not have an effect on the velocity nor velocity gradient patterns when the capillary number Ca was matched with the fluid condition without a surfactant in the droplet generation process.
- The plane where most of the hydrodynamic changes occur is the mid-plane between the channel walls.

- Velocity gradients occur at the middle plane of the channel at the edge of the liquid/liquid interface and change their location dynamically throughout the droplet generation stages.

7.1.2 Major Findings Regarding the Droplet Resistance Project

The hydrodynamics of the droplet transport project in straight rectangular microchannels was performed with a focus on the flow properties of small droplets. This project involved the design of a microchannel network that allowed for accurate monitoring of droplet properties, optimization of a surface treatment protocol, and the use of an experimental measurement approach with high precision and control. Hydrodynamic properties such as droplet excess pressure, and droplet speed were examined against viscosity ratio and interfacial tension variations. The major findings of this project were as follows:

- A channel network design was proposed to study droplet hydrodynamic properties. The measurements of droplet properties were non-intrusive and did not affect the droplet generation size or spacing for the droplet sizes that were studied.

- The applicability for using polycarbonate (PC) as channel substrate material for hydrodynamic studies was investigated and proved to be suitable. PC microchannels are better than soft microchannels, such as PDMS, since they do not swell or deform with pressure.

- Specific guidelines were found for treating PC micro channels with DDA for complex channel networks. These guidelines will help researchers who use PC as a channel substrate material and want to alter channel properties to a hydrophobic condition for stable droplet generation.

- The droplet resistance for small droplets $1 \leq \frac{L_d}{W_d} \leq 1.5$ was a function of Ca and length of droplet L_d. This scale of droplet size was not measured before in the literature in rectangular microchannels.

- The approach that was developed from the design of the microchannel network and experimental system was better than what had been used in the literature since it avoided many error sources such as pressure compliance and swelling of the channel.

- The effects of adding surfactants above and below the CMC concentration were investigated and it was found that the presence of surfactants will affect the excess pressure. The main cause of the change in excess pressure was the reduction in the Laplace pressure jump of the leading and trailing edges of the droplets.

- The effect of viscosity ratio $\left(\frac{\mu_d}{\mu_c}\right)$ below 1 on the excess pressure of droplets was examined and it was found that viscosity ratio will not have an impact on the droplet excess pressure.

- The droplet slip $\left(\beta = \frac{u_d}{u_t} \leq 1\right)$ was found to be less than 1 ($\beta < 1$) for most droplet transport regimes. This finding is contradictory to what was reported in the literature for liquid droplet transport in rectangular microchannels. Reasons for the discrepancy between the literature and these results were discussed.

7.2 Outlook for Future Work

No research is ever complete. A research project tries to answer questions to the best of the ability of the researcher and/or the limitations of the assessment approach. The work that had been done and discussed throughout this thesis tried to probe and explain physical phenomena of monodisperse segmented liquid/liquid flow in rectangular microchannels from generation to transport. The results that were presented showed interesting hydrodynamic aspects of segmented liquid flow. The current work answered some questions and showed the potential of future research. There are several interesting phenomena that are worth examining as an extension of the current work. An attempt to list some potential extensions for each major direction will be briefly discussed.

7.2.1 μPIV Study of Droplet Generation

The experimental μPIV work examined droplet generation in a T-junction for three different droplet generation regimes squeezing, transition, and dripping and showed some interesting results. The findings of velocity and velocity gradients were limited to one phase for certain fluid conditions. There are several topics that could be researched as extensions to the current work, including:

Examining droplet generation with surfactant below CMC: The two concentrations of surfactants that were examined were above CMC and no surfactants. These were extreme surfactant concentrations and it is expected that the surfactant molecules will always cover the surface of the droplet interface. It is interesting to examine the effect of the presence of surfactants with a concentration below CMC on the droplet generation process. One implication of such condition is that Marangoni stresses may appear and may have an influence on the velocity or vorticity fields at the liquid/liquid interface.

Examination of the continuous phase: This can be done by introducing fluorescent particles in the carrier continuous phase. Unfortunately, this is not a simple task since there is no commercially available particles that could be introduced to silicone oils. The other option is to use water based solutions as the continuous phase and oils as the dispersed phase. However, this approach needs special surface treatments to alter the surface property of PDMS, or any other material, to a stable hydrophilic condition that allows for stable oil droplet generation.

Simultaneous two phase flow study: This could be done by having two distinct light sources that excite two different fluorescent particles at two different wavelengths. The challenges that are foreseen for this type of extension include, and not limited to:

- Having a pulsed light source that works in the visible light wavelengths that has a very high repetition aside from green wavelength (ie blue wavelength *480 nm*).

- Introducing fluorescent particles to the oil phase with proper dispersion.
- Image recording with multiple cameras and their alignment.

If the challenges that are mentioned above are solved simultaneous two phase μPIV can be achieved for fast flows.

7.2.2 Droplet Hydrodynamic Resistance

The project that examined the droplet hydrodynamic properties of small confined droplets presented interesting results about droplet transport relative to the carrier continuous phase. The effect of droplet length and Ca were dominant for the ranges of droplet sizes and fluid conditions that were examined. Extensions of the project include:

Studying larger droplet sizes: In order to perform this study a new channel design must be used that allows for large monodisperse droplet generation. Also, the pressure control system should be changed to allow for higher pressures that will allow for more control on droplets, speed and spacing.

Testing other fluid combinations: The fluid combination that was studied was Hexadecane as the continuous phase and water based solutions as the dispersed phase. This fluid combination is limited with a minimum viscosity ratio of 0.29. To study a lower viscosity ratio the continuous phase should be changed to one with a higher viscosity. However, to achieve that the channel surface property must be altered to achieve proper wetting of the chosen continuous phase.

Study of the lubrication regions surrounding droplets: The nature of encapsulation of a liquid segment and the shape and the size of the lubrication regions that surround it are interesting physical properties of the confinement that directly impact droplet transport. The nature of change of these properties under different flow and fluid conditions are still unknown. However, in order to study these properties special experimental techniques and experimental approaches should be designed with the purpose of studying these properties.

Numerical simulations: One potential extension of the droplet transport project would be performing three dimensional simulations of single droplet transport. The models must be three dimensional to emulate the actual confinement conditions of droplets and accurately describe the lubrication regions that confine a droplet. The current findings from experimental work should be used as guidelines and validation tools for the numerical simulations that may be done in the future.

7.2.3 Microchannel Materials and Surface Treatments

During the early work on the hydrodynamic transport properties of liquid droplets the limitations of PDMS as a channel substrate material had been encountered many times. For fluid flow studies in microchannels PDMS is suited for experimental investigations with fluids that do not swell the channel or for studies that focus on a local process. The issues faced while using PDMS led to the switch to polycarbonate (PC) to perform the hydrodynamic studies of trains of droplets. The change of material showed that the area of surface treatment of PC was an interesting topic that is not fully understood for microscale structures.

PC is not the only thermoplastic that could be used for droplet generation applications. There are many types of thermoplastics [16] and large numbers of fluid combinations that could be used for droplet applications. Thus, the investigation of the nature of active surface grafting or other approaches for surface treatment of microchannels is a valid extension. Furthermore, examining other types of thermoplastics for droplet systems is another possible extension.

Appendix A

Optical Trigger Approach for the μPIV System

This appendix will discuss the general requirements and approach used for the external triggering system for the μPIV experiments for droplet studies. The details about the optical based detection approaches that were attempted will be presented [1]. The final assembly that was used and the aspects of phase locking will be briefly discussed.

A.1 External Triggering System

Quantitative optical based measurement techniques with imaging sensors need a sufficient number of images for studying flow properties. With imaging approaches of droplets in flows at least one image is needed for estimating the droplet size, two successive images are needed for estimating the velocity. But for μPIV, or PIV in general, experiments with dual frame CCD cameras can only capture two successive

[1] The proof of concept of the trigger assembly was done by Michael Winer on a co-ap project with an Argon laser and APD detector. His work reached the stage of sensing individual droplets. The final version of the trigger setup used in the current work was modified by from the system that Michael Winer did where the light source, the detector, and triggering signal was changed.

images for one droplet while it is at the area of study. This condition is a challenge for μPIV studies of droplets generation since only one vector plot could be found for a droplet at a certain location. Even the use of high speed CMOS cameras may not solve the issue of capturing many images of a droplet since the sensitivity of CMOS cameras is less than that of CCD cameras [146]. Add to that CMOS camera need a very high exposure or light power as the acquisition speed increases. This was shown by experimental studies that were reported in the literature where the highest reported Ca that was studied with a high speed camera was still in the low speed squeezing regime [118, 144].

In the introductory chapters it was stated that one of the advantages of droplet generation in microchannels is the high frequency of generation that could reach up to kHz with monodisperse droplet size under certain condition [33, 47, 28, 64]. This means that different droplets generated under the same condition (stable pressure and flow rates) are identical. Hence, the results from studying multiple identical droplets can be averaged as long as they droplets are at the same location.

Presence of a droplet at a certain location of a microchannel can be sensed with different approaches such as: capacitance sensor [85], microwave sensor [86], light based detection [147]. Capacitive and microwave sensor work on the basis of detecting differences in the physical properties of droplets compared to the carrier continuous phase, such as the dialectic constant of the fluid. Light based detection is based on simply sending light from a source at a region of interest where the droplet should pass and a detector that senses its presence. Light based detection approaches are broad in their type of instrumentation and method of detection. For example experimental setups can use bright light, lasers, light emitting diodes (LED), and mercury arc lams. Detectors include: CCD or CMOS cameras, photodiodes, avalanche photodiodes, and photomultiplier tubes.

In this work an optical based detection was chosen since other approaches, such as capacitive and microwave sensors, involve a deposition of metallic material on the substrate of the microchannel. This type of deposition creates an obstruction to the light path for of the μPIV laser. For that reason optical based detection was chosen for assembling the triggering circuit.

With light based detection there were some conditions that must be satisfied for the triggering circuit to achieve. These conditions are listed as follows:

1. The light source of the trigger assembly must not be detected by the camera used in the μPIV systems.
2. The light source must not be work in the Nd:YAG laser wavelength ($532nm$) since it shouldn't excite the particles that are used μPIV [2].
3. The signal transformation from the detection to triggering the μPIV system must be fast.

Based on the conditions that were listed above the general components of the triggering circuit were chosen. For example detection with a camera was not an option since the time for recording images, analyzing them and sending a signal to the μPIV system is very long and the sensed droplet will not be in the area of interest. Hence, the principle of measurement that was chosen in this work was to guide light from a light source to the area of interest (AOI) and use light detector that outputs a voltage. Focus on the AOI was done with fiber optic that were guided to the area of interest via waveguides, as clearly shown in Figure 3.1. Single-mode and multi-mode fibers were tested at different combinations and the most reliable approach was using a single-mode fiber with the light source and multi-mode fiber for detector. The reason for that assembly to be consistent is the single mode fiber has a lower numerical aperture which helps focuses the light, while the multimode fiber collects more light from the area of interest and thus, it is better for droplet detection. In all experiments the jacket of the fibers was removed with a fiber stripper which leaves the cladding of the fiber containing the core. The final diameter of the cladding after stripping is 125 μm. There were two versions of the trigger system that were tested. Brief explanations about the two systems will be presented next.

[2]The principle of operation of the C8484-05CP CCD camera is that shutter time of the first frame is controllable while the second frame the shutter is fully open for a time of $\approx 83ms$. Hence, with a continuous light source working at the green wavelength the second frame will record the motion of particles as streaks instead of a single particles after δt

A.1.1 μPIV Trigger Setup and Approach 1

This triggering approach is based on sensing fluorescence light that is detected from an excited fluorophore at a certain wavelength. The light source that was used was a Helium Neon laser (HeNe) which sends a light at a wavelength of $633nm$. This wavelength is used to excite a fluorophore (Alexa Fluor 633 dye, Life Technologies) that was mixed with the dispersed phase. The light emitted from the fluorophore was then guided and filtered by a band bass filter 645-695 nm (Chroma Technology Corp.). Hence, only the signal emitted from the fluorophore in the droplet phase was sensed by the sensor. This approach had been used in the literature to examine the concentration of a dye in a droplet [147].

The first attempts with this version of the trigger used an avalanche photodiode (APD Hamamatsu) as the light sensor. However, the light sensitivity of the APD with this type of apparatus was not operational with the μPIV system since the power of the HeNe laser was set up to a very high level that introduced non uniform exposure between the two images. This was noticed where the second image had larger background intensity. This condition was not suitable for μPIV since the non-uniform exposure between the two successive images could be an error source [1].

To circumvent shortcomings of the APD sensitivity issues a more sensitive detector should be used. The second attempt was to use a very sensitive photomultiplier tube (PMT- H9656-02 Hamamatsu) instead of the APD. The PMT operated better than the APD since it was more sensitive. However, even with lower light that was sent by the laser there was non-uniform exposure between the two images. The reason for still using a high power was that camera could detect it. A typical signal recorded from with using the PMT is shown in Figure A.1-(b) where it shows a pulse like signal with a certain width. The width of the observed signal represents the residence time of the detected droplet between the fibers.

A.1.2 μPIV Trigger Setup and Approach 2

This approach is based on the premise that the refractive index of liquids slightly change at different wavelengths. Even if the dispersed phase and the continuous

phase had the same refractive index at visible light the refractive index might slightly change when it is excited at a different wavelength such as infra-red. Under this principle when a droplet passes through the path of the excited light it will cause a slight light deflection. If the deflection could be sensed than the presence of a droplet is confirmed.

This approach worked when an infra-red IR diode laser emitting light at *780 nm* with a power of *500 mW*. The sensor that was used was the PMT since it showed better sensitivity compared to the APD.

A typical outcome from this triggering approach is presented in Figure A.1-(c) where the spikes present the leading and trailing edge of the droplet. Two consecutive spikes represent one droplet.

The results shown in Figure A.1 illustrate the difference in the outcome between the two triggering approaches. In the first approach the light detected by the sensor shows a high value when a droplet passes. This is an indicator of sensing the emitted light from the flourphore. One the other hand the second triggering approach shows two peaks which correlated to the leading and trailing edges of the droplet when it migrate through the light path of the IR laser. Since there is a slight refractive index miss match at the IR wavelength light will be deflected when a droplet leading or trailing edge passes through the regions of interest.

One important parameter of the trigger system is the success of phase locking of multiple droplets. This parameter could be examined by comparing a number of phase locked droplets and measure the deflection between different the different droplets. It was difficult to estimate this parameter since the droplets did not provide a uniform fluorescent signal since the dispersed phase was doped with a certain concentration of particles. A rough estimate of the expected deflection between phase locked droplet is around 1 μm for different droplets.

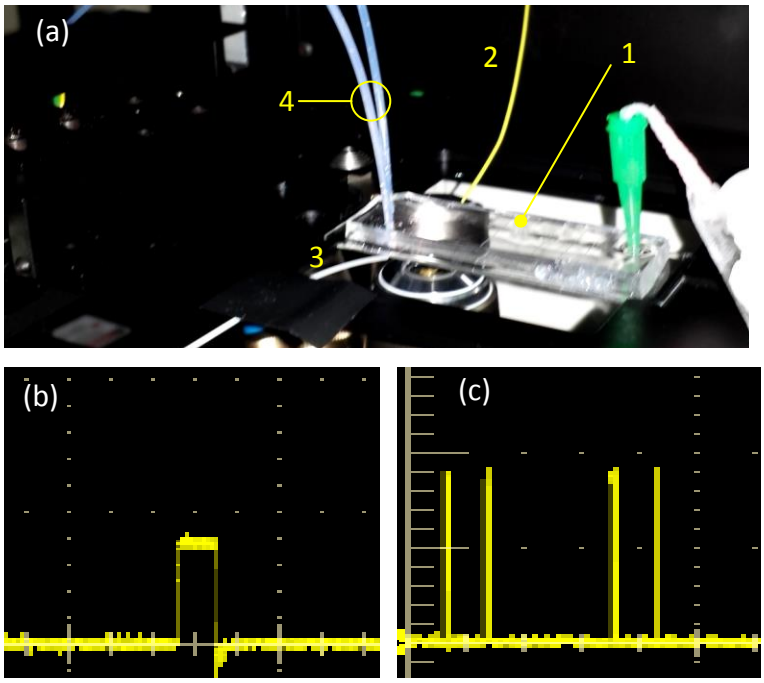

Figure A.1: An image of the PDMS microchannel connected to the tubing and fiber optics and the signals observed from the two trigger approaches that were tested. Figure (a) is for the PDMS microchannels along with the main components which are: 1- PDMS microchannel, 2- Single-mode fiber from light source, 3-Multi-mode fiber to the detection circuit, and 4- Teflon tubing from the syringe pump supplying fluids. Figure (b) Signal recorded from first approach with $HeNe$ laser and light filter $(645-695nm)$, and (c) Signal recorded from the $780nm$ IR diode laser without a light filter.

A.2 Delay Circuit

An important part of the trigger circuit is the delay generator. This was used to impose a delay on signals sent to the μPIV system which allowed for acquiring images of droplets at different phases. Also, in other experiments the delay was long so that droplet that was imaged is the second droplet after of the detected. The delay circuit was an in-house built circuit which can impose delays ranging from 40 μs to 3 ms that were sufficient for most experiments that require imposing a delay. However, one undesired outcome from the delay circuit is that it may cause a signal jitter of around 20 μs. This jitter did not affect most experiments except the experiments in the dripping regime that require high velocities.

Appendix B

PDMS Microchannel Swelling

B.1 PDMS Swelling Observation

It is known that PDMS swells when it is exposed to some oils and solvents. But to what degree will this swelling occur in rectangular microchannels that are commonly used for microfluidics applications? Simple experiments were performed to examine the swelling of PDMS when exposed to some solvents[1]. The experiments were performed on small sections of PDMS bonded to a glass slide coated with liquid PDMS as illustrated in Figure B.1. The approach was inspired by the microtome technique that is used to examine the small sections. Having PDMS microchannel section bonded with all sides to a glass slide approximately emulates the condition of a real microchannel. The most important parameter for this examination is that the slices of the PDMS channel must be as thin as possible. The slices were cut manually and bonded to the substrate.

The solutions that were used to examine the swelling were: silicone oil and hexadecane. These solutions were dispensed on the by a hypodermic needle attached to a plastic syringe that allowed for dispensing the fluid exactly on the microchannel section. After introducing the solutions the channel started swelling and it took up

[1]This work was done as a part of co-op project that was done by a co-ap student on examining the effect of swelling of PDMS on velocity patterns in PDMS microchannels.

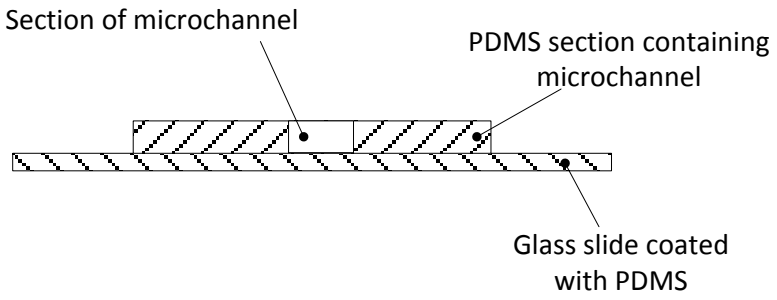

Figure B.1: Schematics of the samples used for examining the PDMS swelling when exposed to some solvents.

to 50 min before it fully swelled. Figure B.2 presents images of the cross sections of microchannels before and after exposure to the swelling solvent. Typical reduction of the cross sections of the microchannel after swelling are listed in Table B.1.

Table B.1: Measurements of changes in the dimensions of the microchannel during the swelling process for a channel section similar to what is presented in Figure B.2.

Time (min)	Channel width	Channel height		
	w μm	h_{left} μm	h_{middle} μm	h_{right} μm
0	200.4	38.5	46.6	38.9
1	200.1	36.9	13.3	37.2
2	2014.3	35.3	16	32.8
After Removal	212.45	27.4	37.8	41.4

From the results presented in Figure B.2 and Table B.1 it is obvious that the swelling of PDMS is a complex phenomenon that has implications on the shape of the channel shape its hydrodynamic resistance. The corner regions of the microchannel suffered the most with them becoming smaller with sharper angles. This reduction in the shape of the corner will affect its resistance. Moreover, this change in the shape of the cross section may have an affect on the transport of liquid droplet in

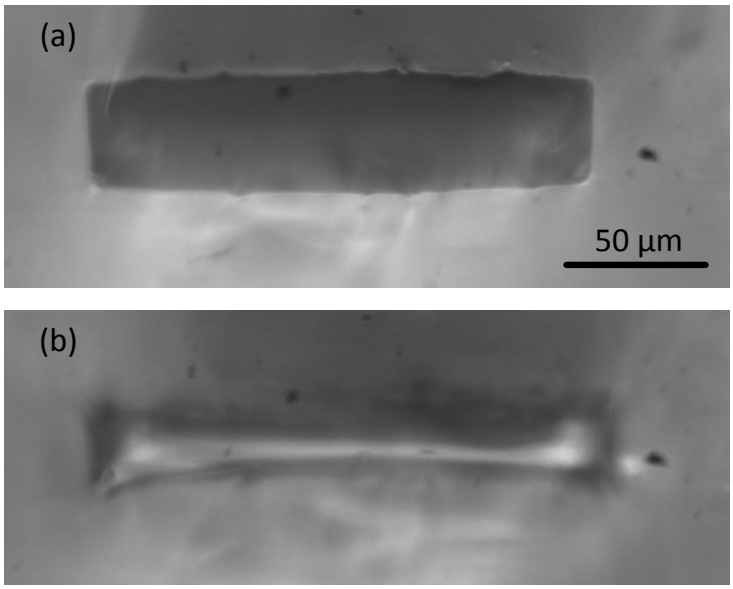

Figure B.2: Images recorded of a microchannel cross section before and after swelling. Figure (a) Channel before exposure solvent, and (b) Channel after exposure to a solvent.

rectangular microchannels. With both the increase in the resistance of the corners sections and the filling of the microchannel with the droplet phase the flow is closer to flows in capillaries than that of rectangular microchannels.

B.2 Simulation of Flow in Swelled Channel

To illustrate influence of swelling on the general velocity profile and maximum velocity a 3D numerical simulation was done with COMSOL multiphysics V4.2 (COMSOL Inc.). The simulations were carried out for a segment of a microchannel representing half of a channel with height 25 μm and width 100 μm. There were two conditions that were examined: normal condition and swelled condition. For the swelled condition the swelling was given to be 5% and was reflected on all the channel walls.

The segment thickness in the simulation was 5 μm. The three walls of the channels were given a non-slip condition while the bottom wall was given a symmetry boundary conditions. The laminar flow physics model was used in the simulation. A free tetrahedral meshing approach was also used. Table B.2 summarizes the parameters used and the outcomes from the COMSOL simulations of flow in the channel conditions. Also, figures of the velocity profiles for the simulated conditions are presented in Figure B.3.

It is clear from the simulation results presented in Table B.2 and the velocity profile shown in Figure B.3 the swelling of 5% in the dimensions had an affect on the shape of the velocity patterns and the maximum velocity in a single phase flow. If another fluid segment is present in the either the swelled on the non swelled channel, the transport of the droplet in the swelled channel is expected be faster. This due to the fact that the resistance in the gutter regions are larger than that of the non swelled condition. Hence, any result for slip factor for experiments performed in channel material that swells must be taken with caution.

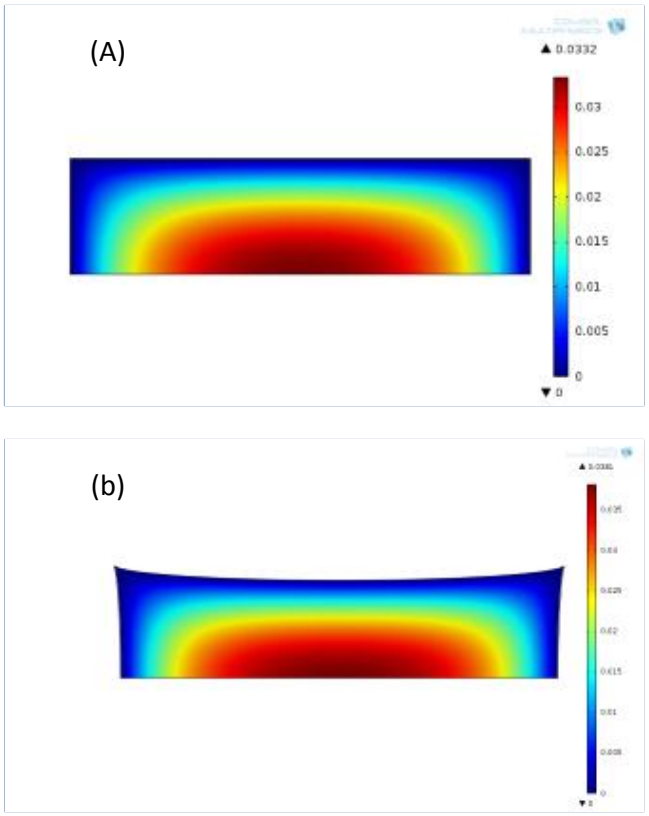

Figure B.3: Singe phase simulation results for the upper portion of a normal channel and swollen channel. Both cases were simulated with an average flow rate of $4.167 \times 10^{-11} m^3/s$ which equivalent to a volume flow rate of $5\mu l/min$ through the whole channel.

Table B.2: The simulation parameters for the effect of swelling in a microchannel segment and results from COMSOL.

Simulation Parameters		
Parameter	Normal Channel	Swelled channel
Flow rate (m^3/s)	4.467e-11	
Number of mesh elements	23,174	20,297
Number of degrees of freedom	144,545	96,889
Density (kg/m^3)	1000	
Dynamic viscosity ($Pa.s$)	1e-3	
Simulation Results		
Maximum Velocity m/s	33.3e-3	38.1e-3
ΔP (Pa)	0.5	0.8

Appendix C

Uncertainty Analysis

This Appendix will present the assessment of the uncertainties associated with the experimental measurements approaches of this work. The first part of this Appendix gives a brief description about the types of uncertainties associated with experimental measurement approaches. The second part presents the experimental uncertainties for the μPIV and the hydrodynamic transport of droplet in microchannels.

C.1 Brief Introduction about Uncertainty

An inherent property with any type of measurement is the uncertainty associated with the measurement. Each measurement device or approach has uncertainties either caused by the sensitivity of the device or how the measurement is acquired. Usually both the accuracy of measurement device along with the method of measurement contributes to the total uncertainty of the measurement. Generally there are two types of uncertainties: bias and random uncertainties [158]. A description of both types will be presented next.

C.1.1 Bias Uncertainty

These types of uncertainties are associated with the measurement device and its sensitivity. Majority of bias uncertainties are associated with the resolution of the device use for a measurement. Other contributors to bias error include: calibration, repetitive and consistent human error, and a defective measurement device. Typically, most measurement devices assign the value of bias uncertainty [158].

C.1.2 Random Uncertainty

Random uncertainty is the uncertainty that arise from the randomness sources that surrounding or is associated with the measurement device, and/or approach. It is also referred to as precision uncertainty. Due to the randomness nature of this type of uncertainty the values will spread approximately with a Gaussian distribution with a mean having the most probable value of the measurement. Sources of the random errors include: disturbance that affect the system, variation in the experimental conditions, and human errors.

Random uncertainty can be reduced by taking a large number of samples and averaging the values. In the case of a limited number of measurements the precision uncertainty is found with [158]:

$$P_x \approx t_{\alpha/2,\gamma} \frac{S_x}{\sqrt{n}} \tag{C.1}$$

where P_x is the precision, or random, uncertainty of the measurement, S_x is the standard deviation of the sample, t is value from the t-distribution curve associated with the number of measurements and the chosen confidence level, n is the number of samples, α is a parameter of the desired confidence level ($\alpha = \frac{1-c}{2}$), and γ is a number related to the number of samples $\gamma = n - 1$.

C.1.3 Total Uncertainty

If there is a variable y that depends on several independent measured variables $(x_1, x_2, ..., x_n)$ each with its own uncertainty, then the uncertainty in estimating y will also be a function of the uncertainties of the independent variables. Let P_y be the random uncertainty of the variable y. This uncertainty will propagate from the independent variables according to [158]:

$$P_y = \sqrt{\left(\frac{\partial y}{\partial x_1} \cdot P_1\right)^2 + \left(\frac{\partial y}{\partial x_2} \cdot P_2\right)^2 + ... + \left(\frac{\partial y}{\partial x_n} \cdot P_n\right)^2} \tag{C.2}$$

where P_1 is the random uncertainty of the independent variable x_1, P_2 is the random uncertainty of the independent variable x_2, and P_n is the random uncertainty of the independent variable x_n.

Equation C.2 can be applied to the bias uncertainty (B_y). After assessing the total bias uncertainty and the total random uncertainty for variable y the total uncertainty is calculated from:

$$U_y = \sqrt{(B_y)^2 + (P_y)^2} \tag{C.3}$$

where U_y is the total uncertainty of variable y, B_y is the bias uncertainty of y, and P_y is the random (precision) uncertainty for variable y.

C.2 μPIV Uncertainty

In Chapter 4 quantitative experimental studies of the flow patterns in the dispersed phase during the droplet generation process were performed. The studies utilized a technique called μPIV which is based simply on tracking the motion of fluorescent particles in the flow field and capture the images at known time intervals. The principle of the μPIV was previously presented in Section 2.3.2. It is important to give an estimation for the uncertainty of the measurements that were performed with the μPIV system.

There are several types of uncertainties associated with μPIV experiments. The two main sources of uncertainties are:

- Particle sources.
- Optical sources.
- Image recording and sensor.

Particle Tracking Issues

Since most of the velocity studies are done in microscaled geometries the issue of the particles tracking the flow an important. Chosen particles should not react with flow or channel material or interact with the channel material. Particles should be spherical and must follow the flow, ideally, without any delay. However, an inherent property for spherical particles is the delay time that is needed for the particles to track the flow. This property is referred to as the response time. According to Milling the [103, 1] the response time for particles can be calculated from:

$$\tau_{resp} = \frac{\rho_f d_p^2}{18\mu_f} \tag{C.4}$$

where τ_{resp} is the time lag before the particle reaches the speed of the flow, d_p is the particle diameter, ρ_f is the fluid density, and μ_f is the fluid dynamic viscosity. From equation C.4, the time response of a particle, when it could virtually follow the flow, is mainly affected by the particle diameter. From the literature, Melling [103] provided a study on particle tracking properties of particles used in laser-based measurement techniques. In his work, Melling [103] gave general overview of particle requirements and some choices of particles for different studies.

The general rules that apply for particle choices in PIV also apply in $\mu - PIV$. However, due to scaling, particle dimensions are in the range of the light source wavelengths. Thus, the light intensity properties that are expected by imaging particles

are small and will be distorted. This light issue is solved with fluorescent imaging where particles absorb light at a certain wavelength and emit light at a higher wavelength which is recorded by the sensor.

Geometrical aspects of both the seeding particles and the critical dimension of the channel are important factors that must be considered prior to performing experiments. The particle diameter must not affect or clog the microchannel. Also, the particle motion in microchannels should not affect the flow field properties. A general rule that is used to choose particles for flow tracking experiments is that the particle diameter must be two orders of magnitude lower than the hydraulic diameter of the microchannel [1, 2]

The flow tracking properties of a particle are commonly assumed to be ideal where the particle follows the flow field due to the high viscous forces in microscale and the small diameter of the particle, as discussed earlier. This assumption is partially true since there exist other forces which are high in the microscale that will affect the particle motion. Forces, such as electrokinetic and surface forces have an impact on the particles motion. As an example, in $\mu - PIV$ studies of electroosmotic flow, where the fluorescent particles are charged [1], the particles will be influenced by two forces: drag force from the fluid motion and electrokinetic force from the electric field, each with a direction according the properties of the channel material and the particles [2].

Although the motion of particles is assumed to be influenced by external forces, there is an important physical phenomenon associated with miniaturizing of particles which contributes to the particle motion. This phenomenon is Brownian motion which will cause a random diffusive motion of particles. This motion is affected by the physical properties of the solution and the particle diameter. An estimation of the Brownian motion for small particles is done with the Einstein equation [2].

$$D = \frac{KT_a}{3\pi\mu_f d_p} \tag{C.5}$$

[1] Most fluorescent particles have a negative surface charge [93].

[2] For a negativity charged microchannel and particles, the speed of found in $\mu - PIV$ experiments is the subtraction of both flow sources viscous drag and electrophoretic motion of the particle [1].

where D is the diffusivity of the particles due to Brownian motion, K is Boltzmann constant, T_a is the absolute temperature (K) of the fluid, μ_f is the viscosity of the fluid, and d_p is the diameter of the particle. As a result from Equation C.5, the Brownian motion is relatively large in microscale. This value will increase as the diameter of the particle decreases; as a result, particles with diameters less than *200 nm*, are rarely used in flow studies. The error from Brownian motion is reduced with averaging approaches.

Table C.1: The major error sources associated with PIV studies and the remedies used to reduce their effects [1, 2].

Error value	**Origin**	**Error type**
$\tau_{resp} = \frac{\rho_f d_p^2}{18\mu_f}$	Particle resonance time	Bias
$D = \frac{KT_a}{3\pi\mu_f d_p}$	Brownian motion	Random
-	Pixilation	Bias
$\delta_d = \frac{d_e}{M}\frac{1}{10}$	Accuracy	Bias
-	Background noise	Random
-	Acceleration errors	Bias
-	Refractive index mismatch in two phase flow	Bias
-	Optical distortions	Bias
-	Statistical cross correlation	Random

For the μPIV experiments performed in the current work the major contributor of the uncertainty was the uncertainty from the spatial location of the particles. This error varied between 4% to 8% for all experiments.

C.3 Droplet Resistance Measurement Uncertainty

The uncertainty analysis for the droplet transport project was performed to all measured variables. Each experimental approach that was used for a variable measurement had a bias and a random uncertainty. However, their importance varied according to the measurement approach. The variables that were measured were: flow rate (Q_o), droplet velocity (u_d), spacing between droplets (λ), droplet width (w_d), and droplet length (L_d).

The assessment of the random uncertainty for each variable was based on the measurement approach. For example the random uncertainty of droplet length L_d was simply the standard deviation calculated from all the measured droplets length that were recorded in the video file for the experimental set and substituted in the parameters of Equation C.1 for an α value of 0.025 that gives a 95 % confidence level.

The measured variable that had the largest standard deviation was the measured flow rate (Q_o). The value of S_{Q_o} ranged from 11 % to 14 % in all experiments. Although this standard deviation is high its contribution to the total uncertainty is reduced because of the averaging. An example of the assessment of precision uncertainty of Q_o is discussed next.

The flow sensor was set to acquire measurement points with a frequency of 2.5 *Hz*. The shortest amount of time that flow rate was measured and stabilized was 2 min for all recorded measurements. This time gives a number of measured data points of n = 300. The maximum standard deviation that calculated was 14 %. For a 95 % confidence level $t_{0.025,\infty} = 1.960$ [158]. This will give a Random uncertainty of the measured flow rate to:

$$P_{Q_o} \approx t_{\alpha/2,\gamma}\frac{S_x}{\sqrt{n}}$$
$$P_{Q_o} \approx 1.960\frac{14}{\sqrt{300}}$$
$$P_{Q_o} \approx 1.58\%$$

The uncertainties associated with these parameters are listed in Table C.2.

Table C.2: Bias and random uncertainty parameters for the droplet hydrodynamic transport property project.

Parameter	Unit	Bias uncertainty	Random uncertainty*
Applied pressure P	mbar	0.3 mbar	0.1 %
Measured flow rate Q_o	$\mu l/min$	0.3 %	2 %
L_d with 4X Objective	μm	10 μm	0.3 %
L_d with 10X Objective	μm	4 μm	0.3 %
w_d with 4X Objective	μm	10 μm	0.3 %
w_d with 10X Objective	μm	4 μm	0.3 %
u_d with 4X Objective	$\mu m/s$	10 $\mu m/s$	0.3 %
u_d with 10X Objective	$\mu m/s$	4 $\mu m/s$	0.3 %

* The random uncertainty was provided for the highest value that was recorded during all experiments according to Equation C.1.

Progression of Uncertainty

An example for the prorogation of the uncertainty when measuring a flow property will be given for the reference hydrodynamic resistance $R_{hyd,Ref}$ for the channel without droplet. This property was experimentally measured from the P & Q relation by finding the slope of this relation. In all calibration experiments that were done for the $R_{hyd,Ref}$ the relation of P & Q was linear with at least an R^2 value above 98 %. Hence, it is accepted to take the measured slope as the actual hydrodynamic resistance. The reference hydrodynamic resistance is calculated with:

$$R_{hyd,Ref} = \frac{P}{Q_o} \tag{C.6}$$

The propagation of the uncertainty for the hydrodynamic resistance will be:

$$U_{R_{hyd,Ref}} = \sqrt{\left(\frac{\partial R_{hyd,Ref}}{\partial P} U_P\right)^2 + \left(\frac{\partial R_{hyd,Ref}}{\partial Q_o} U_{Q_o}\right)^2} \tag{C.7}$$

$$U_{R_{hyd,Ref}} = \sqrt{\left(\frac{1}{Q_o} U_P\right)^2 + \left(\frac{-P}{Q_o^2} U_{Q_o}\right)^2}$$

$$U_{R_{hyd,Ref}} = \sqrt{R_{hyd,Ref}^2 \left(\left(\frac{U_P}{P}\right)^2 + \left(\frac{-U_{Q_o}}{Q_o^2}\right)^2\right)}$$

$$\frac{U_{R_{hyd,Ref}}}{R_{hyd,Ref}} = \sqrt{\left(\frac{U_P}{P}\right)^2 + \left(\frac{-U_{Q_o}}{Q_o^2}\right)^2} \tag{C.8}$$

Where U is the uncertainty that could be bias or random random. The total uncertainty will be combined by both the bias uncertainty and the random uncertainty according to Equation C.3. In a typical experiment the uncertainty of measuring $R_{hyd,Ref}$ was around 2%. The component that contributed the major part of the uncertainty was the random error of the flow rate measurement.

Another example for the propagation of the uncertainty will be given for the measured pressure drop of droplets ($\Delta P_{drop,total}$). The total pressure drop due to the existence of droplets in the measurement section due the existence of droplets is calculated from:

$$\Delta P_{drop,total} = P_{applied} - R_{hyd,Ref} * Q_{with\_drop} \tag{C.9}$$

The uncertainties of the variables for presented in Equation C.9 are listed in Table C.2. The propagation of the uncertainty for $\Delta P_{drop,total}$ can be calculated as follows:

$$U_{\Delta P_{drop,total}} = \sqrt{\left(\frac{\partial \Delta P_{drop,total}}{\partial P} U_P\right)^2 + \left(\frac{\partial \Delta P_{drop,total}}{\partial R_{hyd,Ref}} U_{R_{hyd,Ref}}\right)^2 + \left(\frac{\partial \Delta P_{drop,total}}{\partial Q} U_Q\right)^2} \tag{C.10}$$

$$U_{\Delta P_{drop,total}} = \sqrt{(1 \cdot U_P)^2 + \left(-Q_o \cdot U_{R_{hyd,Ref}}\right)^2 + (-R_{hyd,Ref} \cdot U_Q)^2} \tag{C.11}$$

It should be pointed out that all variables in Equation C.11 should be substituted with their real values at each evaluated point. Both parts of the uncertainty, bias and random, were calculated separately with Equation C.11.

References

[1] M. Raffel, C.E. Willert, S.T. Wereley, and J. Kompenhans. *Particle Image Velocimetry a Practical Guide*. Springer Berlin Heidelberg, 2nd edition, 2007.

[2] N. Nguyen and S. Wereley. *Fundamentals and Applications of Microfluidics*. Artech House, 2nd edition, 2006.

[3] E. Brouzes, M. Medkova, N. Savenelli, D. Marran, M. Twardowski, J. B. Hutchison, J. M. Rothberg, D. R. Link, N. Perrimon, and M. L. Samuels. Droplet microfluidic technology for single-cell high-throughput screening. *Proceedings of the National Academy of Sciences*, 106(34):14195–14200, 2009.

[4] F. P. Bretherton. The motion of long bubbles in tubes. *Journal of Fluid Mechanics*, 10(02):166–188, 1961.

[5] D. M. Fries, F. Trachsel, and P. R. von Rohr. Segmented gasliquid flow characterization in rectangular microchannels. *International Journal of Multiphase Flow*, 34(12):1108 – 1118, 2008.

[6] S. Vanapalli, A. Banpurkar, D. Ende, M. Duits, and F. Mugele. Hydrodynamic resistance of single confined moving drops in rectangular microchannels. *Lab on a Chip*, 9(7):982–990, Apr 2009.

[7] R. Dangla, F. Gallaire, and C. N. Baroud. Microchannel deformations due to solvent-induced pdms swelling. *Lab Chip*, 10:2972–2978, 2010.

[8] G. M. Whitesides. The origins and the future of microfluidics. *Nature*, 442(7101):368–373, Jul 2006.

[9] M. U. Kopp, A. J. deMello, and A. Manz. Chemical amplification: Continuous-flow PCR on a chip. *Science*, 280(5366):1046–1048, 1998.

[10] P. Tabeling. *Introduction to Microfluidics*. Oxford University Press., 2005.

[11] P. S. Dittrich and A. Manz. Lab-on-a-chip: Microfluidics in drug discovery. *Nature Reviews Drug Discovery*, 5(3):210–218, 2006.

[12] H. Bruce. *Theoretical Microfluidics*. Oxford University Press, New York, 2007.

[13] J. Whiteley, F. Gordaninejad, and X. Wang. Magnetorheological fluid flow in microchannels. *Journal of Applied Mechanics-Transactions of the ASME*, 77(4), JUL 2010.

[14] X. Ding, P. Li, Sz-C. S. Lin, Z. S. Stratton, N. Nama, F. Guo, D. Slotcavage, X. Mao, J. Shi, F. Costanzo, and T. J. Huang. Surface acoustic wave microfluidics. *Lab Chip*, 13:3626–3649, 2013.

[15] Y. Jin, A. Orth, E. Schonbrun, and K. B. Crozier. Measuring the pressures across microfluidic droplets with an optical tweezer. *Opt. Express*, 20(22):24450–24464, Oct 2012.

[16] A. del Campo and E. Arzt. *Generating Micro-and Nanopatterns on Polymeric Materials*. Wiley-VCH, 2011.

[17] J. M. K. Ng, I. Gitlin, A. D. Stroock, and G. M. Whitesides. Components for integrated poly(dimethylsiloxane) microfluidic systems. *ELECTROPHORESIS*, 23(20):3461–3473, 2002.

[18] D. C. Duffy, J. C. McDonald, J. A. Schueller, and G. M. Whitesides. Rapid prototyping of microfluidic systems in poly(dimethylsiloxane). *Analytical Chemistry*, 70(23):4974–4984, 1998.

[19] I. Chen and E. Lindner. The stability of Radio-Frequency Plasma-Treated polydimethylsiloxane surfaces. *Langmuir*, 23(6):3118–3122, March 2007.

[20] J. L. Pittman, C. S. Henry, and S. D. Gilman. Experimental studies of electroosmotic flow dynamics in microfabricated devices during current monitoring experiments. *Analytical Chemistry*, 75(3):361–370, Feb 2003.

[21] Z. Almutairi, C. L. Ren, and L. Simon. Evaluation of polydimethylsiloxane (PDMS) surface modification approaches for microfluidic applications. *Colloids and Surfaces A: Physicochemical and Engineering Aspects*, 415(0):406 – 412, 2012.

[22] J. Zhou, D. A. Khodakov, A. V. Ellis, and N. H. Voelcker. Surface modification for pdms-based microfluidic devices. *ELECTROPHORESIS*, 33(1):89–104, 2012.

[23] J. N. Lee, C. Park, and G. M. Whitesides. Solvent compatibility of poly(dimethylsiloxane)-based microfluidic devices. *Anal. Chem.*, 75(23):6544–6554, 2003.

[24] T. Glawdel, Z. Almutairi, S. Wang, and C. L. Ren. Photobleaching absorbed rhodamine b to improve temperature measurements in pdms microchannels. *Lab Chip*, 9:171–174, 2009.

[25] P. Cheung, K. Toda-Peters, and A. Q. Shen. In situ pressure measurement within deformable rectangular polydimethylsiloxane microfluidic devices. *Biomicrofluidics*, 6(2):–, 2012.

[26] C-W. Tsao and D. L. DeVoe. Bonding of thermoplastic polymer microfluidics. *Microfluidics and Nanofluidics*, 6(1):1–16, 2009.

[27] P. Jankowski, D. Ogonczyk, A. Kosinski, W. Lisowski, and P. Garstecki. Hydrophobic modification of polycarbonate for reproducible and stable formation of biocompatible microparticles. *Lab Chip*, 11:748–752, 2011.

[28] P. Garstecki, M. Fuerstman, and G. M. Stone, H. A.and Whitesides. Formation of droplets and bubbles in a microfluidic t-junction-scaling and mechanism of break-up. *Lab on a chip*, 6(3):437–46, mar 2006.

[29] V. Van Steijn, M. Kreutzer, and C. Kleijn. μ-PIV study of the formation of segmented flow in microfluidic T-junctions. *Chemical Engineering Science*, 62(24):7505–7514, dec 2007.

[30] A. R. Abate, P. Mary, V. van Steijn, and D. A. Weitz. Experimental validation of plugging during drop formation in a T-junction. *Lab on a Chip*, 12(8):1516–1521, Apr 2012.

[31] K. Wang, Y. C. Lu, J. H. Xu, and G. S. Luo. Determination of dynamic interfacial tension and its effect on droplet formation in the t-shaped microdispersion process. *Langmuir*, 25(4):2153–2158, 2009.

[32] P. Jankowski, D. Ogonczyk, W. Lisowski, and P. Garstecki. Polyethyleneimine coating renders polycarbonate resistant to organic solvents. *Lab Chip*, 12:2580–2584, 2012.

[33] S-Y. Teh, R. Lin, L-H. Hung, and A. P. Lee. Droplet microfluidics. *Lab Chip*, 8:198–220, 2008.

[34] S. Sharma, M. Srisa-Art, S. Scott, A. Asthana, and A. Cass. Droplet-based microfluidics. In Gareth Jenkins and Colin D. Mansfield, editors, *Microfluidic Diagnostics*, volume 949 of *Methods in Molecular Biology*, pages 207–230. Humana Press, 2013.

[35] S. Koster, F. E. Angile, H. Duan, J. J. Agresti, A. Wintner, C. Schmitz, A. C. Rowat, C. A. Merten, D. Pisignano, A. D. Griffiths, and D. A. Weitz. Drop-based microfluidic devices for encapsulation of single cells. *Lab Chip*, 8:1110–1115, 2008.

[36] J. Wan, A. Bick, M. Sullivan, and H. A. Stone. Controllable microfluidic production of microbubbles in water-in-oil emulsions and the formation of porous microparticles. *Advanced Materials*, 20(17):3314–3318, 2008.

[37] Y. Schaerli and F. Hollfelder. The potential of microfluidic water-in-oil droplets in experimental biology. *Mol. BioSyst.*, 5:1392–1404, 2009.

[38] C. N. Baroud, F. Gallaire, and R. Dangla. Dynamics of microfluidic droplets. *Lab on a Chip*, 10(16):2032–2045, Jul 2010.

[39] G. Christopher, N. Noharuddin, J. Taylor, and S. Anna. Experimental observations of the squeezing-to-dripping transition in t-shaped microfluidic junctions. *Physical Review E (Statistical, Nonlinear, and Soft Matter Physics)*, 78(3):036317 (12 pp.) –, Sept. 2008.

[40] E. Rebrov. Two-phase flow regimes in microchannels. *Theoretical Foundations of Chemical Engineering*, 44:355–367, 2010.

[41] A. Kawahara, P.M.-Y. Chung, and M. Kawaji. Investigation of two-phase flow pattern, void fraction and pressure drop in a microchannel. *International Journal of Multiphase Flow*, 28(9):1411 – 1435, 2002.

[42] M. Kreutzer, F. Kapteijn, J. Moulijn, C. Kleijn, and J. Heiszwolf. Inertial and interfacial effects on pressure drop of taylor flow in capillaries. *AIChE Journal*, 51(9):2428–2440, 2005.

[43] T. Cubaud and C. Ho. Transport of bubbles in square microchannels. *Physics of Fluids (1994-present)*, 16(12):4575–4585, 2004.

[44] T. Thorsen, R. W. Roberts, F. H. Arnold, and S. R. Quake. Dynamic pattern formation in a vesicle-generating microfluidic device. *Phys. Rev. Lett.*, 86:4163–4166, Apr 2001.

[45] J. Berthier. *Microdrops and Digital Microfluidics*. William Andrew Inc., 2008.

[46] R. Seemann, M. Brinkmann, T. Thomas Pfohl, and S. Herminghaus. Droplet based microfluidics. *Reports on Progress in Physics*, 75(1):016601, 2012.

[47] G. Christopher and S. Anna. Microfluidic methods for generating continuous droplet streams. *Journal of Physics D: Applied Physics*, 40(19):R319–R336, oct 2007.

[48] J. D. Tice, H. Song, A. D. Lyon, and R. F. Ismagilov. Formation of droplets and mixing in multiphase microfluidics at low values of the reynolds and the capillary numbers. *Langmuir*, 19(22):9127–9133, oct 2003.

[49] K-Y. Tung, C-C. Li, and J-T. Yang. Mixing and hydrodynamic analysis of a droplet in a planar serpentine micromixer. *Microfluidics and Nanofluidics*, 7(4):545–557, feb 2009.

[50] A. Gunther, M. Jhunjhunwala, M. Thalmann, M. A. Schmidt, and K. Jensen. Micromixing of miscible liquids in segmented gas-liquid flow. *Langmuir*, 21(4):1547 – 1555, 2005.

[51] R. F. Probstein. *Physicochemical Hydrodynamics: An Introduction*. Wiley-Interscience, 2 edition, May 2003.

[52] W. L. Olbricht. Pore-scale prototypes of multiphase flow in porous media. *Annual Review of Fluid Mechanics*, 28(1):187–213, 1996.

[53] P. M. Adler and H. Brenner. Multiphase flow in porous media. *Annual Review of Fluid Mechanics*, 20(1):35–59, 1988.

[54] V. va Steijn, C. R. Kleijn, and M. T. Kreutzer. Predictive model for the size of bubbles and droplets created in microfluidic t-junctions. *Lab on a Chip*, 10(19):2513–2518, Sep 2010.

[55] T.C Ransohoff and C.J Radke. Laminar flow of a wetting liquid along the corners of a predominantly gas-occupied noncircular pore. *Journal of Colloid and Interface Science*, 121(2):392 – 401, 1988.

[56] V. S. Ajaev and G. M. Homsy. Modeling shapes and dynamics of confined bubbles. *Annual Review of Fluid Mechanics*, 38(1):277–307, 2006.

[57] M. Dong and I. Chatzis. The imbibition and flow of a wetting liquid along the corners of a square capillary tube. *Journal of Colloid and Interface Science*, 172(2):278 – 288, 1995.

[58] M. T. Sullivan and H. A. Stone. The role of feedback in microfluidic flow-focusing devices. *Philosophical Transactions of the Royal Society A: Mathematical, Physical and Engineering Sciences*, 366(1873):2131–2143, 2008.

[59] T. Glawdel and C. L. Ren. Global network design for robust operation of microfluidic droplet generators with pressure-driven flow. *Microfluidics and Nanofluidics*, 13(3):469–480, 2012.

[60] N. R. Beer, K. A. Rose, and I. M. Kennedy. Observed velocity fluctuations in monodisperse droplet generators. *Lab Chip*, 9:838–840, 2009.

[61] V. Van Steijn, M.T. Kreutzer, and C.R. Kleijn. Velocity fluctuations of segmented flow in microchannels. *Chemical Engineering Journal*, 135, Supplement 1(0):S159 – S165, 2008. Microreaction Technology {IMRET} 9: Proceedings of the Ninth International Conference on Microreaction Technology {IMRET9} Special Issue.

[62] M. Fuerstman, A. Lai, M. Thurlow, S. Shevkoplyas, H.A. Stone, and G. M. Whitesides. The pressure drop along rectangular microchannels containing bubbles. *Lab on a Chip*, 7(11):1479 – 89, 2007/11/.

[63] S. Jakiela, P. Korczyk, S. Makulska, O. Cybulski, and P. Garstecki. Discontinuous transition in a laminar fluid flow: A change of flow topology inside a droplet moving in a micron-size channel. *Phys. Rev. Lett.*, 108:134501, Mar 2012.

[64] T. Glawdel, C. Elbuken, and C. L. Ren. Droplet formation in microfluidic t-junction generators operating in the transitional regime. ii. modeling. *Phys. Rev. E*, 85:016323, Jan 2012.

[65] P. Korczyk, O. Cybulski, S. Makulska, and P. Garstecki. Effects of unsteadiness of the rates of flow on the dynamics of formation of droplets in microfluidic systems. *Lab Chip*, 11:173–175, 2011.

[66] K. Churski, J. Michalski, and P. Garstecki. Droplet on demand system utilizing a computer controlled microvalve integrated into a stiff polymeric microfluidic device. *Lab Chip*, 10:512–518, 2010.

[67] J-C. Galas, D. Bartolo, and V. Studer. Active connectors for microfluidic drops on demand. *New Journal of Physics*, 11(7):075027, 2009.

[68] P. G. de Gennes. Wetting: statics and dynamics, Jul 1985.

[69] P. G. de Gennes, F. Brochard-Wyart, and D. Quere. *Capillary and Wetting Phenomena Drops, Bubbles, Pearls, Waves*. Springer, 2004.

[70] M. J. Rosen. *Surfactants and Interfacial Phenomena*. John Wiley & Sons, Inc., 2004.

[71] T. Glawdel and C. L. Ren. Droplet formation in microfluidic t-junction generators operating in the transitional regime. iii. dynamic surfactant effects. *Phys. Rev. E*, 86:026308, Aug 2012.

[72] B. Adzima and S. Velankar. Pressure drops for droplet flows in microfluidic channels. *Journal of Micromechanics and Microengineering*, 16(8):1504, 2006.

[73] Y. Wang, J. Balowski, C. Phillips, R. Phillips, C. E. Sims, and N. L. Allbritton. Benchtop micromolding of polystyrene by soft lithography. *Lab Chip*, 11:3089–3097, 2011.

[74] L. Derzsi, P. Jankowski, W. Lisowski, and P. Garstecki. Hydrophilic polycarbonate for generation of oil in water emulsions in microfluidic devices. *Lab Chip*, 11:1151–1156, 2011.

[75] J. C. Baret. Surfactants in droplet-based microfluidics. *Lab Chip*, 12:422–433, 2012.

[76] K. A. Erk, J. D. Martin, J. T. Schwalbe, F. Phelan Jr, and S. D. Hudson. Shear and dilational interfacial rheology of surfactant-stabilized droplets. *Journal of Colloid and Interface Science*, 377(1):442 – 449, 2012.

[77] K. Stebe, S. Lin, and C. Maldarelli. Remobilizing surfactant retarded fluid particle interfaces. i. stress-free conditions at the interfaces of micellar solutions of surfactants with fast sorption kinetics. *Physics of Fluids A: Fluid Dynamics (1989-1993)*, 3(1), 1991.

[78] J. Xu, G. Luo, S. Li, and G. Chen. Shear force induced monodisperse droplet formation in a microfluidic device by controlling wetting properties. *Lab on a chip*, 6(1):131–6, jan 2006.

[79] K. Wang, Y. Lu, J. Xu, and G. Luo. Determination of dynamic interfacial tension and its effect on droplet formation in the t-shaped microdispersion process. *Langmuir : the ACS journal of surfaces and colloids*, 25(4):2153–8, feb 2009.

[80] Jing Liu and Nam Trung Nguyen. Numerical simulation of droplet-based microfluidics - a review. *Micro and Nanosystemse*, 2(3):193–201, September 2010.

[81] G. Karniadakis and A. Beskok. *Micro flows: fundamentals and simulation.* Springer, New York, 2002.

[82] H. Yang, Q. Zhou, and L. Fan. Three-dimensional numerical study on droplet formation and cell encapsulation process in a micro t-junction. *Chemical Engineering Science*, 87(0):100 – 110, 2013.

[83] M. De Menech, P. Garstecki, F. Jousse, and H. A. Stone. Transition from squeezing to dripping in a microfluidic t-shaped junction. *Journal of Fluid Mechanics*, 595, January 2008.

[84] M. Mohammadi and K. V. Sharp. Experimental techniques for bubble dynamics analysis in microchannels: A review. *Journal of Fluids Engineering-Transactions of the ASME*, 135(2, SI), FEB 2013.

[85] Caglar Elbuken, Tomasz Glawdel, Danny Chan, and Carolyn L. Ren. Detection of microdroplet size and speed using capacitive sensors. *Sensors and Actuators A: Physical*, 171(2):55–62, Nov 2011.

[86] M. S. Boybay, A. Jiao, T. Glawdel, and C. L. Ren. Microwave sensing and heating of individual droplets in microfluidic devices. *Lab on a Chip*, 13(19):3840–3846, Aug 2013.

[87] A. Huebner, M. Srisa-Art, D. Holt, C. Abell, F. Hollfelder, J. DeMello, and J. B. Edel. Quantitative detection of protein expression in single cells using droplet microfluidics. *Chemical communications (Cambridge, England)*, 2(12):1218–20, mar 2007.

[88] C. Wang, N. Nguyen, and T. Wong. Optical measurement of flow field and concentration field inside a moving nanoliter droplet. *Sensors and Actuators A: Physical*, 133(2):317–322, feb 2007.

[89] J. H. Xu, S.W. Li, J. Tan, and G.S. Luo. Correlations of droplet formation in t-junction microfluidic devices: From squeezing to dripping. *Microfluidics and Nanofluidics*, 5(6):711 – 717, 2008.

[90] T. Fu, Y. Ma, D. Funfschilling, C. Zhu, and H. Z. Li. Squeezing-to-dripping transition for bubble formation in a microfluidic T-junction. *Chemical Engineering Science*, 65(12):3739 – 3748, 2010.

[91] V. Van Steijn, M.T. Kreutzer, and C.R. Kleijn. Velocity fluctuations of segmented flow in microchannels. *Chemical Engineering Journal*, 135, Supplement 1(0):S159 – S165, 2008.

[92] K. Shinohara, Y. Sugii, A. Aota, A. Hibara, M. Tokeshi, T. Kitamori, and K. Okamoto. High-speed micro-piv measurements of transient flow in microfluidic devices. *Measurement Science and Technology*, 15(10):1965 – 1970, 2004.

[93] R. Lindken, M. Rossi, S. GroBe, and J. Westerweel. Micro-particle image velocimetry (piv): recent developments, applications, and guidelines. *Lab on a Chip*, 9(17):2551 – 67, 7 Sept. 2009.

[94] F. Li and K. Hishida. Particle image velocimetry techniques and its applications in multiphase systems. In J. Li, editor, *Characterization of Flow, Particles and*

Interfaces, volume 37 of *Advances in Chemical Engineering*, chapter 3, pages 87 – 147. Academic Press, 2009.

[95] R. Adrian. Twenty years of particle image velocimetry. *Experiments in Fluids*, 39(2):159–169, jul 2005.

[96] J. Westerweel. Fundamentals of digital particle image velocimetry. *Measurement Science and Technology*, 8(12):1379 – 92, 1997/12/.

[97] A. Schroeder and C. E. Willert, editors. *Particle Image Velocimetry New Developments and Recent Application*. Springer Berlin Heidelberg, 2008.

[98] K.T. Christensen and R.J. Adrian. Measurement of instantaneous eulerian acceleration fields by particle image accelerometry: Method and accuracy. *Experiments in Fluids*, 33(6):759–769, 2002.

[99] N. Fujisawa, Y. Nakamura, F. Matsuura, and Y. Sato. Pressure field evaluation in microchannel junction flows through μPIV measurement. *Microfluidics and Nanofluidics*, 2(5):447–453, March 2006.

[100] S. Y. Jaw, J. H. Chen, and P. C. Wu. Measurement of pressure distribution from PIV experiments. *Journal of Visualization*, 12(1):27–35, mar 2009.

[101] C. Willert, G. Stockhausen, M. Voges, J. Klinner, R. Schodl, C. Hassa, B. Schrmans, and F. Gthe. Selected applications of planar imaging velocimetry in combustion test facilities. In *Particle Image Velocimetry*, volume 112 of *Topics in Applied Physics*, pages 283–309. Springer Berlin Heidelberg, 2008.

[102] M. Rossi, R. Lindken, and J. Westerweel. Optimization of multiplane μPIV for wall shear stress and wall topography characterization. *Experiments in Fluids*, 48:211–223, 2010.

[103] A. Melling. Tracer particles and seeding for particle image velocimetry. *Measurement Science and Technology*, 1406, 1997.

[104] M. Mielnik and L. Saetran. Selective seeding for micro-PIV. *Experiments in Fluids*, 41(2):155–159, jan 2006.

[105] M. Reeder, J. Crafton, J. Estevadeordal, J. DeLapp, C. McNiel, D. Peltier, and T. Reynolds. Clean seeding for flow visualization and velocimetry measurements. *Experiments in Fluids*, 48(5):889–900, nov 2009.

[106] C. Bourdon, M. Olsen, and A. Gorby. The depth of correlation in μ-piv for high numerical aperture and immersion objectives. *Transactions of the ASME. Journal of Fluids Engineering*, 128(4):883 – 6, 2006/07/. numerical aperture optics;immersion objectives;correlation depth;measurement depth;microscopic particle image velocimetry;magnification optics;Gaussian particle approximation;refraction index;.

[107] S. Wereley and C. D. Meinhart. Recent advances in micro-particle image velocimetry. *Annual Review of Fluid Mechanics*, 42:557 – 576, 2010.

[108] R. Budwig. Refractive index matching methods for liquid flow investigations. *Experiments in Fluids*, 17(5):350–355, September 1994.

[109] E. Yamaguchi, B. J. Smith, and D. P. Gaver. μ-PIV measurements of the ensemble flow fields surrounding a migrating semi-infinite bubble. *Experiments in Fluids*, 47(2):309–320, apr 2009.

[110] B. Kim, Y. Liu, and H. Sung. Micro PIV measurement of two-fluid flow with different refractive indices. *Measurement Science and Technology*, 15(6):1097–1103, jun 2004.

[111] A. Gunther and K. F. Jensen. Multiphase microfluidics: from flow characteristics to chemical and materials synthesis. *Lab Chip*, 6:1487–1503, 2006.

[112] J. Go and S. Shoji. Digital sorting of flow-through droplet phase microfluid. *Japanese Journal of Applied Physics*, 42(Part 2, No. 5A):L448–L450, may 2003.

[113] C. Wang, Nguyen. N., and T. Wong. Optical measurement of flow field and concentration field inside a moving nanoliter droplet. *Sensors and Actuators A: Physical*, 133(2):317–322, feb 2007.

[114] T. Fu, Y. Ma, D. Funfschilling, and H. Li. Bubble formation and breakup mechanism in a microfluidic flow-focusing device. *Chemical Engineering Science*, 64(10):2392–2400, may 2009.

[115] D. Malsch, M. Kielpinski, R. Merthan, J. Albert, G. Mayer, J. Kohler, H. Suse, M. Stahl, and T. Henkel. $\mu-$ piv-analysis of taylor flow in micro channels. *Chemical Engineering Journal*, 135:S166–S172, jan 2008.

[116] V. Van Steijn, C. Kleijn, and M. Kreutzer. Flows around confined bubbles and their importance in triggering pinch-off. *Physical Review Letters*, 103(21):1–4, nov 2009.

[117] D. Malsch, N. Gleichmann, M. Kielpinski, G. Mayer, T. Henkel, D. Mueller, V. Van Steijn, C. Kleijn, and M. Kreutzer. Dynamics of droplet formation at t-shaped nozzles with elastic feed lines. *Microfluidics and Nanofluidics*, 8(4):497–507, APR 2010.

[118] H. Kinoshita, M. Oshima, S. Kaneda, and T. Fujii. Validation of Confocal Micro-PIV Technique by Poiseuille Flow Measurement. *2006 International Conference on Microtechnologies in Medicine and Biology*, (May):78–80, 2006.

[119] H. Kinoshita, S. Kaneda, T. Fujii, and M. Oshima. Three-dimensional measurement and visualization of internal flow of a moving droplet using confocal micro-piv. *Lab on a chip*, 7(3):338–46, mar 2007.

[120] G. I. Taylor. Deposition of a viscous fluid on the wall of a tube. *Journal of Fluid Mechanics*, 10:161–165, 3 1961.

[121] E. Walsh, Y. Muzychka, P. Walsh, V. Egan, and J. Punch. Pressure drop in two phase slug/bubble flows in mini scale capillaries. *International Journal of Multiphase Flow*, 35(10):879–884, Oct 2009.

[122] H. Foroughi and M. Kawaji. Viscous oilwater flows in a microchannel initially saturated with oil: Flow patterns and pressure drop characteristics. *International Journal of Multiphase Flow*, 37(9):1147 – 1155, 2011.

[123] J. Jovanović, W. Zhou, E. V. Rebrov, T. A. Nijhuis, V. Hessel, and J. C. Schouten. Liquid-liquid slug flow: Hydrodynamics and pressure drop. *Chemical Engineering Science*, 66(1):42 – 54, 2011.

[124] S. R. Hodges, O. E. Jensen, and J. M. Rallison. The motion of a viscous drop through a cylindrical tube. *Journal of Fluid Mechanics*, 501:279–301, 2 2004.

[125] R. Gupta, S. Y. Leung, D. F. Manica, R. andFletcher, and B. S. Haynes. Hydrodynamics of liquid-liquid taylor flow in microchannels. *Chemical Engineering Science*, 92(0):180 – 189, 2013.

[126] P. Woehl and R. L. Cerro. Pressure drop in monolith reactors. *Catalysis Today*, 69(14):171 – 174, 2001. Srtuctured Catalysts and Reactors.

[127] T. C. Thulasidas, M. A. Abraham, and R. L. Cerro. Bubble-train flow in capillaries of circular and square cross section. *Chemical Engineering Science*, 50(2):183–199, Jan 1995.

[128] T. C. Thulasidas, R. L. Cerro, and M. A. Abraham. The monolith froth reactor - residence time modeling and analysis. *Chemical Engineering Research & Design*, 73(A3):314–319, APR 1995. 2nd International Conference on Gas-Liquid-Solid Reactor Engineering, Cambridge, England, MAR 27-29, 1995.

[129] W. B. Kolb and R. L Cerro. Coating the inside of a capillary of square cross section. *Chemical Engineering Science*, 46(9):2181 – 2195, 1991.

[130] M. T. Kreutzer, F. Kapteijn, J. A. Moulijn, and J. J. Heiszwolf. Multiphase monolith reactors: Chemical reaction engineering of segmented flow in microchannels. *Chemical Engineering Science*, 60(22):5895–5916, Nov 2005.

[131] X. Casadevall i Solvas and A. deMello. Droplet microfluidics: recent developments and future applications. *Chem. Commun.*, 47:1936–1942, 2011.

[132] X. Niu, S. Gulati, J. B. Edel, and A. J. deMello. Pillar-induced droplet merging in microfluidic circuits. *Lab Chip*, 8:1837–1841, 2008.

[133] D. Hoang, C. Haringa, L. Portela, M. Kreutzer, C. Kleijn, and V. Van Steijn. Design and characterization of bubble-splitting distributor for scaled-out multiphase microreactors. *Chemical Engineering Journal*, 236(0):545 – 554, 2014.

[134] W. Lee and G. Son. Numerical study of obstacle configuration for droplet splitting in a microchannel. *Computers & Fluids*, 84(0):351 – 358, 2013.

[135] T. Glawdel, C. Elbuken, and C. L. Ren. Passive droplet trafficking at microfluidic junctions under geometric and flow asymmetries. *Lab Chip*, 11:3774–3784, 2011.

[136] D. A. Sessoms, A. Amon, L. Courbin, and P. Panizza. Complex dynamics of droplet traffic in a bifurcating microfluidic channel: Periodicity, multistability, and selection rules. *Phys. Rev. Lett.*, 105:154501, Oct 2010.

[137] V. Labrot, M. Schindler, P. Guillot, A. Colin, and M. Joanicot. Extracting the hydrodynamic resistance of droplets from their behavior in microchannel networks. *Biomicrofluidics*, 3(1):012804, 2009.

[138] T. Gervais, J. El-Ali, A. Gunther, and K. F. Jensen. Flow-induced deformation of shallow microfluidic channels. *Lab Chip*, 6:500–507, 2006.

[139] I. S. Khattab, F. F Bandarkar, M. Khoubnasabjafari, and A. Jouyban. Density, viscosity, surface tension, and molar volume of propylene glycol + water mixtures from 293 to 323 + k and correlations by the jouybanacree model. *Arabian Journal of Chemistry*, (0):–, 2012.

[140] Hamamatsu. *Digital CCD Camera C8484-05C*, 2014.

[141] Z. Almutairi, C. L. Ren, and D. Johnson. μPIV Study of Passive Droplet Generation in a T-junction in the Squeezing, Transition, and Dripping Regimes. volume -. The International Symposia on Applications of Laser Techniques to Fluid Mechanics, July 2014.

[142] D. Malsch, N. Gleichmann, M. Kielpinski, G. Mayer, T. Henkel, D. Mueller, V Van Steijn, C. R. Kleijn, and M. T. Kreutzer. Dynamics of droplet formation

at T-shaped nozzles with elastic feed lines. *Microfluidics and Nanofluidics*, 8(4):497–507, aug 2009.

[143] M. Oishi, H. Kinoshita, T. Fujii, and M. Oshima. Confocal micro-PIV measurement of droplet formation in a T-shaped micro-junction. *Journal of Physics: Conference Series*, 147:012061, feb 2009.

[144] M. Oishi, H. Kinoshita, M. Oshima, and T. Fujii. Investigation of Micro Droplet Formation in a T-Shaped Junction Using Multicolor Confocal Micro PIV. volume PART A of *2008 Proceedings of the ASME Micro/Nanoscale Heat Transfer International Conference, MNHT 2008*, pages 297–301. ASME, 2008.

[145] M. Oishi, H. Kinoshita, T. Fujii, and M. Oshima. Simultaneous measurement of internal and surrounding flows of a moving droplet using multicolour confocal micro-particle image velocimetry (micro-piv). *Measurement Science and Technology*, 22(10):105401, 2011.

[146] R. Hain, C.J. Kahler, and C. Tropea. Comparison of CCD, CMOS and intensified cameras. *Experiments in Fluids*, 42(3):403 – 11, 2007.

[147] F. Guo, M. Lapsley, A. Nawaz, Y. Zhao, S. Lin, Y. Chen, S. Yang, X. Zhao, and T. Huang. A droplet-based, optofluidic device for high-throughput, quantitative bioanalysis. *Analytical Chemistry*, 84(24):10745–10749, 2012.

[148] F.M. White. *Fluid Mechanics*. McGraw-Hill series in mechanical engineering. McGraw-Hill Higher Education, 2011.

[149] Mark A Eddings, Michael A Johnson, and Bruce K Gale. Determining the optimal pdmspdms bonding technique for microfluidic devices. *Journal of Micromechanics and Microengineering*, 18(6):067001, 2008.

[150] Z. Almutairi, C. L. Ren, and D. Johnson. Experimental study of the hydrodynamics transport of liquid droplets in polycarbonate microchannels. Denver, CO, March 3-7 2014. American Physics Society, APS.

[151] C. A. Schneider, W. S. Rasband, and K. W Eliceiri. NIH Image to ImageJ: 25 years of image analysis. *Nat Meth*, 9(7):671–675, jul 2012.

[152] MATLAB. *version 12.0 (R2020b)*. The MathWorks Inc., Natick, Massachusetts, 2020.

[153] T. C. Thulasidas, M. A. Abraham, and R. L. Cerro. Bubble-train flow in capillaries of circular and square cross-section. *Chemical Engineering Science*, 50(2):183–199, JAN 1995.

[154] H. Wong, C. J. Radke, and S. Morris. Motion of long bubbles in polygonal capillaries. part 1. thin films. *Journal of Fluid Mechanics*, 292:71 – 94, 1995.

[155] S. Jakiela, S. Makulska, P. Korczyk, and P. Garstecki. Speed of flow of individual droplets in microfluidic channels as a function of the capillary number, volume of droplets and contrast of viscosities. *Lab Chip*, 11:3603–3608, 2011.

[156] R. Balasubramaniam, E. Ramé, J. Kizito, and M. Kassemi. Two phase flow modeling: Summary of flow regimes and pressure drop correlations in reduced and partial gravity. NASA/CR 214085, National Center for Space Exploration Research, Cleveland, Ohio, 2006.

[157] K. Stebe and C. Maldarelli. Remobilizing surfactant retarded fluid particle interfaces: Ii. controlling the surface mobility at interfaces of solutions containing surface active components. *Journal of Colloid and Interface Science*, 163(1):177 – 189, 1994.

[158] T. G. Beckwith, R. D. Marangon, and V. J. H. Lienhard. *Mechanical Measurements*. Prentice Hall, 5th edition, 1993.